3-30-2021

Optomechanical Quantum Entanglement

Kahlil Y. Dixon
Louisiana State University and Agricultural and Mechanical College

OPTOMECHANICAL QUANTUM ENTANGLEMENT

A Dissertation

Submitted to the Graduate Faculty of the
Louisiana State University and
Agricultural and Mechanical College
in partial fulfillment of the
requirements for the degree of
Doctor of Philosophy

in

The Department of Physics & Astronomy

by
Kahlil Y. Dixon
B.S., Howard University, USA, 2016
May 2021

This Ph.D. dissertation is dedicated to the memories of Jon Dowling, Anand P. Batra, Donnie Marie Pickett-Dixon, Donnie Ray Speer, Anne Cooke, James A. Donaldson, Julius Grant, and Arthur Nathaniel Thorpe.

Acknowledgments

I would first like to thank the love of my life, Smita Speer, for her constant support and encouragement during my academic career. For eight years, she has been my uplifting linchpin as I climbed towards goals that once seemed insurmountable. Thank you for keeping me grounded and sane throughout this arduous process.

I want to thank the professors in my research group: Dr. Thomas Corbitt, Dr. Mark Wilde, Dr. Lior Cohen, Dr. Hwang Lee, and the late Dr. Jonathan P. Dowling. I also want to thank the additional professors who served on my dissertation committee, Dr. Omar Magaña-Loiaza and Dr. Shawn Walker. I want to thank Dr. Dowling and Dr. Wilde in particular. Without their acknowledgment and support, I would not have joined this research group.

I would also like to thank my coursework professors for providing rigorous and supporting learning structures that enabled my doctoral studies and elevated my working knowledge of the physical world. Those professors are Dr. Dan Sheehy, Dr. Ilya Vehkter, Dr. Rongying Jin, Dr. Jorge Pullin, Dr. Omar Magaña-Loiaza, the late Dr. Jon Dowling, Dr. Mark Wilde, Dr. Ravi Rau, William Dr. McElgin, Dr. Scott Marley, and Dr. Dana Browne. Special thanks go to Daniel Sheehy and Dr. Ilya Vehkter for their guidance and support in my early graduate career. I want to thank LSU staff members Paige Whittington and Arnell Nelson for their assistance with the necessary registration and finical management that enabled my studies at LSU. I would also like to thank my friends and colleges at LSU that have offered me their time, support, and presence: Dr. Narayan Bhusal, Michelle Lollie, Graeme Morgan, Dr. Chenglong You, Emily Saffron, Tyler Ellis, Arshag Danageozian, Dr. David Alspaugh, and Vishal Katariya.

I would be remiss if I did not also thank those that helped me get to LSU in the first place, my Howard University mentors and advisors: Dr. Marcus Alfred, Dr. James Lindesay, Dr. Walter Lowe, Dr. Gregory Jenkins, Dr. Thomas Searles, Dr. Kimani A. Stancil, Dr. Belay Demoz, the late great Dr. Arthur Thorpe, the late Anne Cooke, Dr.

Demetrius Venable, and the late Dr. James Donaldson.

I need to thank my academic life's biggest influences, my mother, Dr. Rebecca S. Dixon, my grandfather Dr. Robert M. Dixon, and my (high school) first two physics teachers, Christopher Wright and Dr. Desi. My godfather, Dr. Gregory Carr, and all my family for their support and kindness. I would also like to offer thanks and good fortune to my friends in physics outside LSU: Nathaniel Lashley-Colthirst, Sergio Smith, Janelle Holmes, Ryan Hubbard, Odunayo Ayegbajeje, Stanford Carter, Aara'L Yarber, Nick Sneed, Greg, Ryan O'Donnell, Olivia Dickens, and Kevaughn Johnson. Also, I am thankful for the foundation in mathematics and science provided by my middle school teachers: Ms. McCarthy, Ms. Watkins, Mr. Harding, and Ms. Hawkins.

Special thanks to my undergraduate professors that made a lasting positive impact on me as well: Dr. Wayne Patterson, LSU Alumni Dr. Jabari Lee, Dr. Valethia Watkins, Dr. Mario Beatty, Dr. Chen. I cannot forget the efforts of those who have since left LSU: Nick Lanning, Nick Studer, Sushovit, Sahil, and Sumeet Khatri, as well as the professors at LSU that offered me aid outside the department, Dr. Gloria Thomas and Dr. Tyrslai Williams-Carter. Furthermore, thanks to my undergraduate internship research mentors, Belay Demoz, Demetrius Venable, Mickey Chiu, Victor Galitski, Jim Freericks, and Sonia Najhafi. Finally, I would like to acknowledge the financial support from the Army Research Office and the Bridge to the Doctorate Fellowship.

Table of Contents

Abstract

As classical technology approaches its limits, exploration of quantum technologies is critical. Quantum optics will be the basis of various cutting-edge research and applications in quantum technology. In particular, quantum optics quite efficacious when applied to quantum networks and the quantum internet. Quantum Optomechanics, a subfield of quantum optics, contains some novel methods for entanglement generation. These entanglement production methods exploit the noise re-encoding process, which is most often associated with creating unwanted phase noise in optical circuits. Using the adapted two-photon formalism and experimental results, we simulate (in an experimentally viable parameter space) optomechanical entanglement generation experiments. These simulations consider dual coherent field input, displaced single-mode squeezed input, and displaced two-mode squeezed inputs. Unsqueezed inputs should yield an E_N of about 0.1 at room temperature, although very high measurement certainty is needed to observe this in the laboratory. Squeezing the displaced input fields increases the expected output entanglement significantly (maximum of E_N of about 1). Furthermore, when considering dual two-mode squeezed input (4 fields) in the simulation, the optomechanical cavity demonstrates squeezing angle-dependent entanglement distribution.

Chapter 1
Introduction

The development of applied quantum physics and quantum technologies is at the intersection of many science fields (genetics, material science, condensed matter, optics, computer science, machine learning, etc.) [1, 2, 3, 4, 5, 6]. As knowledge of classical mechanics allowed for the development and application of the classical machinery that sparked the industrial era, quantum mechanics shall usher in a new technological age. More than ever, physical phenomena must be better understood to fully implement technologies such as quantum networks, quantum sensors, universal one-way quantum computers, and the quantum internet. Ultimately, extensive research is required in an array of areas of quantum physics and physical phenomena. One aspect critical to most quantum technologies today and tomorrow is the need for a stable and efficient entanglement source. Correlations are fundamental to communication. In general, the transmission of information from point A to B requires a message sent between the sender and receiver. However, communication channels today are typically over classical communications networks, which are still lacking in security, privacy, and bandwidth relative to their quantum technological counterparts.

Furthermore, Quantum Mechanics can produce advantageous correlation effects. These quantum physics principles make quantum technologies an attractive option for upgrading classical communication networks. Squeezed states and quantum entanglement are physically fundamental corollary phenomena that will be the central limiting resource behind all quantum networks and most quantum technologies. These resources are already in high demand today and will only become more valuable in the future, yet we do not have efficient production methods [7, 8]. Thus, to further develop the technologies involved in entanglement generation and entanglement distributions, this work explores quantum cavity optomechanics. Quantum cavity optomechanics is a sub-field of cavity optics; it considers a mechanical oscillator's motion coupled to the optical cavity fields. Exploiting these phenomena can produce a novel source of quantum light. Ponderomotive entanglement is an entanglement generation technique that has gained recent attention [9]. It exploits op-

tomechanical couplings, which are traditionally noise sources in most optics measurements. To examine the effects of the radiation pressure and quantum back action in our simulations, we consider a dual homodyne quadrature variance measurement of two optical output fields from a single cavity double optical spring. The mechanically oscillating endmirror's mass is small enough to enhance further the quantum back-action effects (see Chapter 4) (micromirror (μmirror)). Two coherent input states yield entangled light. A single input yields displaced squeezed light. Both distinctive outputs, of course, require careful attention and treatment of variables and experimental complications such as cavity linewidth, optical losses, mechanical oscillator temperature, cavity circulating power, optomechanical detunings, etc. These are all considered in the simulations reported in the chapters that follow. Achieving large N entanglement (macroscopic entanglement) will significantly bolster the attention, efficacy, and applications of quantum technologies (quantum key distribution, quantum teleportation, quantum metrology, etc.) [10] [11]. The most popular method for producing entangled photons is Spontaneous Parametric Down Conversion (SPDC). SPDC involves illuminating a birefringent material with laser light. This method yields at most two entangled photon pairs per approximately a million input photons [12]. This method will not be reliable as demands increase due to costs and other factors. Developing a scalable optical entanglement generation method that did not depend on crystal purity is ideal. Optomechanical cavity-based entanglement generation is, so far, not scalable. It is also not yet known to yield competitive entanglement rates. The work and results in the chapters that follow will demonstrate both the typical entanglement output seen in the recent experimental work and some computational studies [9, 13]. We will make a case for how these devices could yield significant entanglement rates while considering laboratory conditions and constraints.

Previous research reaffirms optomechanical methods' applications in entanglement generation—the theoretical study of entanglement of two optical fields from two optical cavities. In 2007 D. Vitali et al. showed that entanglement could theoretically manifest be-

tween an electromagnetic field and a movable mirror [14]. Then, in 2008 Christopher Wipf, Thomas Corbitt, Y. Chen, and Mavalvala adapted Vitali et al.'s approach to generating bipartite entangled optical fields [15]. Later, Y. Wang and A Clerk at Mc Gill University showed that the optomechanical entanglement of two cavity electromagnetic modes and a laser-cooled mirror could actualize optomechanical entanglement when subject to the suitable optomechanical couplings and other favorable experimental constraints. Furthermore, if the couplings can be easily adjusted, the entanglement can be maximized [16]. Interestingly, researchers from Texas A&M University reported that, in theory, a two-cavity two-qubit system could act as a quantum state "beam" splitter of sorts; thus predicted to yielding maximally entangled N00N states from input $|N\rangle \otimes |0\rangle$ [17] [18]. (Chapter 6 reveals more evidence of optomechanical cavities acting as beam splitter-like devices.) They also demonstrated scaling up the system produced multi-N00N states.

Additionally, optomechanical cavities yield squeezed light when the radiation pressure noise is high [19]. More research into maximizing this squeezing is currently underway [20]. Moreover, recent work on optomechanical entanglement includes significant computational and experimental investigation. One experimental paper of note achieves bipartite optical entanglement from an oscillating silicone membrane optomechanical cavity. The computational works showed that optomechanical cavities should still output entangled states without cryogenics [21, 13]. Furthermore, Our study showed that the input quantum noise ratio to the thermal noise determines the entanglement's temperature sensitivity.

Not many experimental reports on the ponderomotive entanglement systems have been published. This lack of experiments is partly due to some disconnect between what is and is not accessible in the laboratory. One goal of this research is to amend this disconnect. Another is to help realize ponderomotive entanglement at LSU and explore possible scaling configurations towards innovative, efficacious entanglement devices through the comprehensive study of ponderomotive entanglement generation. This study will begin with the simulation of this optomechanical entanglement process. This study considers laboratory

constraints and optomechanical cavities' response to quantum noises. Furthermore, it aims to explore upscaling optomechanical systems and the possibility of macroscopic entanglement or other useful entanglement devices.

Creating, aligning, and executing experiments is an arduous task: a task that can end with wasted time, effort, and financial resources. There is a demand for simulations that can closely and accurately simulate possible experiments. A failed computational project is often less expensive than a failed experimental one. Previous work by Corbitt et al. has established a functioning optomechanical circuit simulation. The program has proven accurate in predicting higher-order mechanical effects and their influence over the optomechanical cavities' quantum dynamics [22, 23, 20].

This dissertation will begin with a short review of quantum optics and entanglement measures in this research. The next chapter will provide the reader with a quick introduction to quantum cavity optomechanics and the mathematical frameworks used to study these systems. For a more comprehensive review of quantum cavity optomechanics, see the paper by Aspelmeyer et al. [24]. This dissertation will discuss some of the current quantum cavity optomechanics applications in entanglement and squeezing-based devices. It will also cover the work done to extend the simulation programs to examine possible experiments and provide insight into optomechanical entanglement. Squeezing will also be discussed briefly.

Chapter 2
A Brief Introduction to Quantum Optics

2.1 Field quantization

...photons don't really exist like electrons or protons. They are just an [outdated] explanatory device. That's why you don't see them in physics...I do research in optics and from what I have seen light is purely classical... there is no such thing as quantum optics...
–Dr. Ye Feng Technical Director at LAM Research

People tend to take the optical for granted. The above quote serves as proof. A former physicist assumes to understand optics because he works with optics often, forgetting that in a sense, we all "work with optics". Quantum Optics can serve many purposes, but one of those can be a humbling one. The ability to manipulate something is not evidence of understanding that something.

Field quantization is the most fundamental derivation in Quantum Optics. Field quantization is that critical because it establishes the ever-elusive photon.

To begin, we start from Maxwell's Equations:

$$\nabla \cdot \mathbf{E} = \rho/\epsilon_0 \ , \tag{2.1}$$

$$\nabla \cdot \mathbf{B} = 0 \ , \tag{2.2}$$

$$\nabla \times \mathbf{E} = -\frac{\partial \mathbf{B}}{\partial t} \ , \tag{2.3}$$

$$\nabla \times \mathbf{B} = \mu_0(\mathbf{J} + \epsilon_0 \frac{\partial \mathbf{E}}{\partial t}) \ . \tag{2.4}$$

These equations are known to describe the dynamics of classical light as an electromagnetic wave. Next, we apply these equations to a scenario that will properly yield hints into light's quantum nature. For this, we imagine a one-dimensional box of length L (an optical cavity) that entirely confines the light. As a further simplification, let us assume that the light is

completely polarized in the x-direction, and the light is only free to propagate and reflect off the bounds of the box. Let us say for the time being that the trapped light is or can be equated to a single photon. Maxwell's equations for the system are

$$\nabla \cdot \mathbf{E} = \nabla \cdot \mathbf{B} = 0, \tag{2.5}$$

$$\nabla \times \mathbf{E} = -\frac{\partial \mathbf{B}}{\partial t}, \tag{2.6}$$

$$\nabla \times \mathbf{B} = \mu_0 \epsilon_0 \frac{\partial \mathbf{E}}{\partial t}, \tag{2.7}$$

These develop into a wave equation:

$$\nabla \times \mathbf{E} = -\frac{\partial \mathbf{B}}{\partial t}, \tag{2.8}$$

$$\nabla \times \mathbf{B} = \mu_0 \epsilon_0 \frac{\partial \mathbf{E}}{\partial t}, \tag{2.9}$$

$$\nabla \times -\frac{\partial \mathbf{B}}{\partial t} = -\mu_0 \epsilon_0 \frac{\partial^2 \mathbf{E}}{\partial t^2}, \tag{2.10}$$

$$\nabla \times (\nabla \times \mathbf{E}) = -1/c_0^2 \frac{\partial^2 \mathbf{E}}{\partial t^2}, \tag{2.11}$$

then, apply

$$\nabla \times (\nabla \times \mathbf{A}) = \nabla(\nabla \cdot \mathbf{A}) - \nabla^2 \mathbf{A}, \tag{2.12}$$

$$(\text{where } \nabla^2 \mathbf{A} = (\nabla \cdot \nabla)\mathbf{A}), \tag{2.13}$$

$$\text{and since } \nabla \cdot \mathbf{E} = 0 \quad \nabla \times (\nabla \times \mathbf{E}) = -\nabla^2 \mathbf{E}, \tag{2.14}$$

which leaves us the wave equation (in $\mathbf{E}$ and $\mathbf{B}$),

$$\nabla^2 \mathbf{E} - \frac{1}{c^2} \frac{\partial^2 \mathbf{E}}{\partial t^2} = 0 = \nabla^2 \mathbf{B} - \frac{1}{c^2} \frac{\partial^2 \mathbf{B}}{\partial t^2}. \tag{2.15}$$

Since the light is polarized in the x-direction the electric field is considered of the

form $\mathbf{E} = \hat{\mathbf{x}}\ E_x(z,t)$. This allows us to *easily* solve the differential equations above and see, after boundary conditions are considered, that $E_x(z,t) = \sqrt{\frac{2\omega^2}{L\epsilon_0}} q(t)\sin(kz)$. Like the particle in a box example from vanilla quantum mechanics, ω is the frequency, $q(t)$ is a function that acts as the position of a particle later, so here we call it $q(t)$. Furthermore, we note that from Maxwell's equations, the magnetic field must obey the relation: $\mathbf{B} = \hat{\mathbf{y}}\frac{\mu_0\omega}{k}\sqrt{\frac{2\epsilon_0}{L}} \cdot q(t)\cos(kz)$. With forms for the electric and magnetic fields, we can write the Hamiltonian as $H = 1/2\int(\epsilon_0\mathbf{E}^2 + 1/\mu_0\mathbf{B}^2)dV$; after integrating, we find

$$H = 1/2(p^2 + \omega^2 q^2)\ ; \tag{2.16}$$

since their Hamiltonians are the same, the single optical mode acts like a harmonic oscillator. Since these are the canonical position and momentum variables, we can replace them with the operators. Moreover, since the single-mode follows the same Hamiltonian as the harmonic oscillator, the ladder operators satisfy the commutation relation $[\hat{a}, \hat{a}^\dagger] = 1$. Thus the position and momentum operators $\hat{q}$ and $\hat{p}$ follow the canonical commutation relation. For the remainder of this work, we will refer to these operators as the quadrature operators $\hat{\mathbf{X}}$ and $\hat{\mathbf{Y}}$ respectively.

2.2 Quadrature operators

The analogous phase space operators for quantum optics are the quadrature operators, here written in terms of the ladder operators $\hat{\mathbf{X}}$ and $\hat{\mathbf{Y}}$ follow the equations below:

$$\hat{\mathbf{X}} = \frac{\hat{\mathbf{a}}^\dagger + \hat{\mathbf{a}}}{2} \qquad \hat{\mathbf{Y}} = i\frac{(\hat{\mathbf{a}}^\dagger - \hat{\mathbf{a}})}{2}. \tag{2.17}$$

They are the position ($\hat{\mathbf{X}}$) and momentum ($\hat{\mathbf{Y}}$) analogues for electromagnetic oscillations. They follow the quantum canonical commutation relation directly: $[\hat{\mathbf{X}}, \hat{\mathbf{Y}}] = i\hbar$. Consequently, they are useful for creating optical phase space diagrams (see figure 2.1).

Such diagrams give a compelling visual representation of the statistics of optical states

and operations on optical states. Here these operators allow for the characterization of Gaussian state statistics for the quantification of bipartite optical entanglement. They are great for visualizing squeezing.

It is also useful to establish a generic quadrature operator that varies with a quadrature angle ζ:

$$\hat{\mathbf{Q}}(\zeta) = \frac{1}{2}(\hat{\mathbf{a}}^\dagger \, e^{i\zeta} + \hat{\mathbf{a}} e^{-i\zeta}) \; . \tag{2.18}$$

This form is beneficial when creating the optical phase space plots. This form allows for the X quadrature as $\zeta = 0$ and Y quadrature as $\zeta = \pi/2$.

2.3 Coherent states

Here coherent states refer to optical Gaussian states with a second-order coherence function equal to unity. These states are noiseless laser light. They are also the Eigenstates of the annihilation operators:

$$\hat{\mathbf{a}} \, |\alpha\rangle \;\; = \;\; \alpha \, |\alpha\rangle \, . \tag{2.19}$$

2.4 The Wigner quasiprobability distribution function

Another necessary tool in exploring quantum optics is the Wigner quasiprobability distribution (or only Wigner function). A quasiprobability distribution (QPDF) could be hastily described as a distribution function that almost could be called a probability distribution function (PDF). To fully classify as a PDF, distribution functions must satisfy the three Kolmogorov axioms at the foundation of probability theory. The Wigner function violations the first and third of these axioms. Specifically, the non-negativity and σ-additivity axioms.

A wavefunction's Wigner function is also the generator for the wavefunction's spatial autocorrelations. This feature of the Wigner function directly relates the wavefunction to

the noise power spectral density. For a pure state, the Wigner function is:

$$W(X,Y) = \frac{1}{\pi\hbar}\int_{-\infty}^{\infty} \psi^*(X+X')\psi(X-X')\exp\left[\frac{-2iYX'}{\hbar}\right] dX' \ . \tag{2.20}$$

Moreover, in general, and in this dissertation, we primarily deal with mixed states. The Wigner function for an arbitrary mixed state with density matrix operator $\hat{\rho}$ is:

$$W(X,Y) = \frac{1}{\pi\hbar}\int_{-\infty}^{\infty} \langle X+X'|\,\hat{\rho}\,|X-X'\rangle \exp\left[\frac{-2iYX'}{\hbar}\right] dX' \ . \tag{2.21}$$

2.5 Squeezed light

Squeezed light is a form of quantum light with minimal uncertainty and whose statistics are modified to yield higher noise in one measurable mode than another canonically conjugate mode. The result is light with phase uncertainty under the Heisenberg $\hbar/2$ limitation while amplitude noise is increased.

To demonstrate the topics from sections 2.2-2.4, we shall plot the Wigner distribution for a squeezed coherent state. Our squeezed coherent state has a wavefunction $\langle x|\psi\rangle = \psi(x)$ where $\hbar = 1$ let

$$\psi(x) = \exp\left(-\frac{(x-1)^2}{2w_0^2} + 2ix\right) \quad \text{(ignoring the normalization constant for now).} \tag{2.22}$$

In this form the parameter, w_0, represents the squeezing; $w_0 > 1$ represents amplitude squeezing and $0 < w_0 < 1$ represents phase squeezing. Using the equation 2.20 Wigner function can be written as

$$W(X,Y) = \sqrt{\pi}|w_0|e^{\left(4{w_0}^4(4+Y(iX+Y-4))+{w_0}^2X(3X-4iY)+(X-8)X-4\right)} \ ; \tag{2.23}$$

the "squeezing" of the coherent function is more apparent in the Wigner function plots as

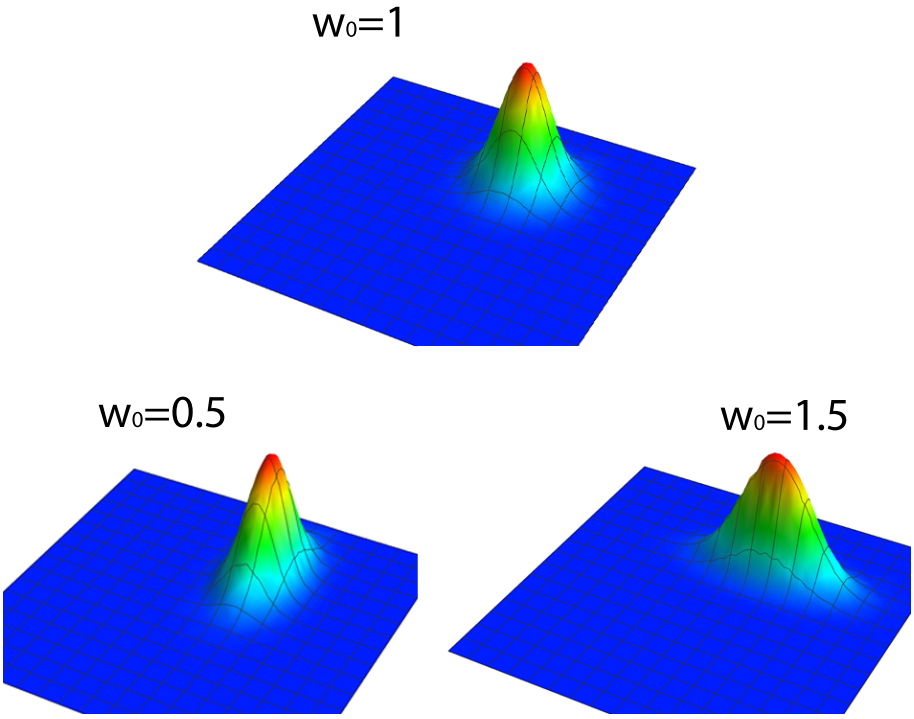

Figure 2.1: The above images are 3D plots of the Wigner quasiprobability distribution of three nearly identical coherent states. The only difference between the coherent states above is the squeezing amount quantified by the parameter, w_0, and its deviation from unity (note that $w_0 > 0$). The Wigner function plotted is mathematically described by equation 2.23.

displayed in figure 2.1.

Then, we can fully characterize quantum states with the Wigner quasiprobability distribution within the optical phase space. Future work (discussed in Chapter 7) will heavily involve solving and propagating the intracavity Wigner functions to produce the full process tomography [25]. Here, the function solely serves to provide a fundamental method for visualizing the optical quantum states and showing a coherent field's squeezing.

2.6 Operator propagation

One of the go-to methods for solving quantum optical systems applies a matrix transformation to the incident optical fields yielding the output fields or vice versa. Essentially, taking incident field operator from $\hat{\mathbf{a}}$ to $\hat{\mathbf{a}}'$ via a set of equations specific to the type of optic the field is acting on/ passing through. The following section reviews an example applica-

tion of this method for single photons ($N = 1$ Fock states). However, these methods can (and will) be applied to continuous-variable quantum optics as well (see sections 2.5.1 and Chapter 4 and 5).

Beamsplitter Example

As a quick example of operator propagation through an optical apparatus we examine a single photon state incident on a (50:50) beam splitter (figure 2.2). Here the initial state, $|\psi_{\text{input}}\rangle$, is just a single photon, $|1\rangle_1$. Then the solving following the matrix equation for the outgoing field operators we find expressions for modes $\hat{\mathbf{a}}_2$ and $\hat{\mathbf{a}}_3$:

$$\begin{pmatrix} \hat{\mathbf{a}}_2 \\ \hat{\mathbf{a}}_3 \end{pmatrix} = \begin{pmatrix} t_2 & r_1 \\ r_2 & t_1 \end{pmatrix} \times \begin{pmatrix} \hat{\mathbf{a}}_0 \\ \hat{\mathbf{a}}_1 \end{pmatrix} \tag{2.24}$$

for a 50:50 beam splitter the transmission and reflection coefficients all equal to $\sqrt{0.5}$. Our initial state is then rewritten as $|1\rangle_1 = \hat{\mathbf{a}}_1 |0\rangle$. This in combination with the matrix equation about reveal the outgoing fields as (see figure 2.2) :

$$|\psi\rangle_{out} = \frac{1}{\sqrt{2}}(|0\rangle_2 |1\rangle_3 + |1\rangle_2 |0\rangle_3) \; ; \tag{2.25}$$

here the matrix equation determines how the initial field ladder operators are transformed by the beam splitter, how the operators propagate around the beam splitter.

2.7 Homodyne measurement

Homodyne measurement or homodyne detection is the measurement technique most critical to the research that follows. They allow the measurement of quadrature means and variances, making them highly useful when working with Gaussian states.

Typically, this is considered an electrical engineering technique that excels at extracting information from frequency modulations. This scheme uses a local oscillator considered to have zero frequency modulation relative to the signal beam detected. In optics, the local

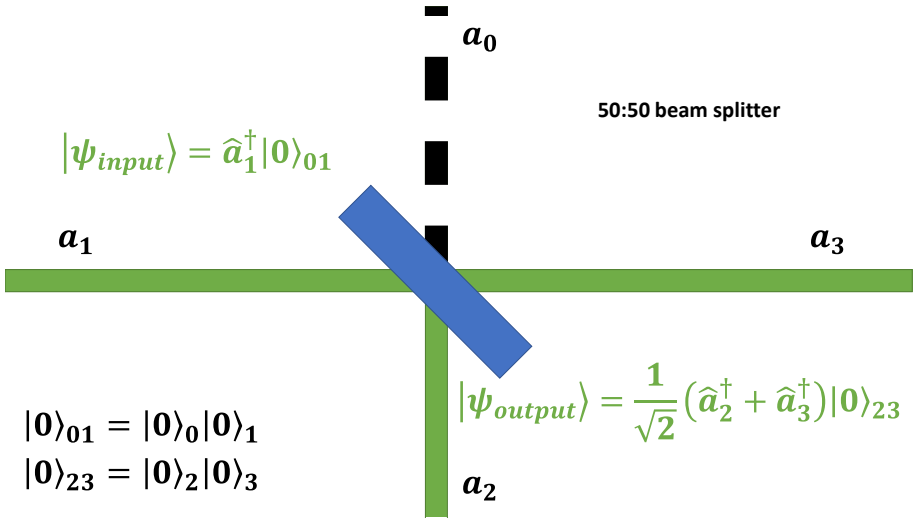

Figure 2.2: A single photon incident on a beam splitter yields an $N = 1$ N00N state [26].

oscillator is the unsqueezed optical source. Alternatively, using the signal (squeezed light) as a reference oscillator is called self-homodyne detection [27, 28]. Ultimately, the path length of one arm of the optical circuit is varied intentionally to create a difference in phase between the two paths. This phase difference corresponds to the quadrature angle ζ in equation 2.18. The measured deviation from the local oscillator at some phase is the quadrature measurement at the corresponding angle.

2.7.1 Dual homodyne measurement in the two-photon formalism

When trying to characterize entangled Gaussian states, more quadrature spaces are necessary. In order to correctly measure the statistics of such systems, multiple homodyne detection schemes are necessary. The parallel homodyne detectors are necessary because the quadrature modes' entanglement and correlations will appear as noise in the single-angle quadrature measurement.

Our programs simulate the noises and losses associated with the measurement. Later in this work, the simulated experiments require several (three or more) parallel homodyne

detection circuits. Fortunately, using the adapted two-photon formalism, we can write the homodyne measurement step in each experiment as a function. A function that is readily modified to adapt to detector modes necessary to characterize the bipartite entanglement (see appendix-B). The adapted two-photon formalism is a method of operator propagation regarding the twin sideband modes as a single term [29, 22].

2.8 Beam splitter entanglement

Here we review a standard method for generating optical entanglement. Here beam splitter entanglement refers to methods that involve sending single-mode squeezed light to a beam splitter [30]. Such methods of using squeezed light to create entanglement present a problem in our analysis of squeezed light enhancement of optomechanical cavity entanglement generation (see Chapter 6).

We begin with one single-mode squeezed vacuum state incident on a 50:50 beam splitter. The input state$|\psi_N\rangle$ is $|\psi\rangle_1 = |\xi\rangle_1 = \hat{\mathbf{S}}\,|0\rangle_1$. The application of equation 2.24 we find (considering as well the phase difference factor of i):

$$\hat{\mathbf{a}}_2 = \sqrt{1/2}(i\hat{\mathbf{a}}_0 + \hat{\mathbf{a}}_1) \quad \hat{\mathbf{a}}_3 = \sqrt{1/2}(\hat{\mathbf{a}}_0 + i\hat{\mathbf{a}}_1)\ . \tag{2.26}$$

This reduces to the following:

$$\hat{\mathbf{a}}_1 = \frac{\sqrt{2}}{2}(\hat{\mathbf{a}}_3 - i\hat{\mathbf{a}}_2) \quad \text{and} \quad \hat{\mathbf{a}}_1^\dagger = \frac{\sqrt{2}}{2}(\hat{\mathbf{a}}_3^\dagger + i\hat{\mathbf{a}}_2^\dagger)\ . \tag{2.27}$$

The input state is the squeezing operator acting on vacuum so the operator to transform is the single-mode squeezing operator $\hat{\mathbf{S}}$, where $\hat{\mathbf{S}} = \exp\Big[1/2(\xi^*\hat{\mathbf{a}}_1^2 - \xi\hat{\mathbf{a}}_1^{\dagger 2})\Big]$. The transformed operator becomes:

$$\begin{aligned}\hat{\mathbf{S}}_1' = \exp\left[\frac{1}{2}(\frac{\xi^*}{2}\,\hat{\mathbf{a}}_2^2 - \frac{\xi}{2}\hat{\mathbf{a}}_2^{\dagger 2}) - \frac{1}{2}(\frac{\xi^*}{2}\,\hat{\mathbf{a}}_3^2 - \frac{\xi}{2}\hat{\mathbf{a}}_3^{\dagger 2}) + \frac{1}{2}((i\xi)^*\hat{\mathbf{a}}_2\hat{\mathbf{a}}_3 - (i\xi)\hat{\mathbf{a}}_2^\dagger\hat{\mathbf{a}}_3^\dagger)\right] \\ = \hat{\mathbf{S}}_2(\xi/2)\hat{\mathbf{S}}_3^\dagger(\xi/2)\hat{\mathbf{S}}_{23}^{(2)}(i\xi)\ ;\end{aligned} \tag{2.28}$$

where $\hat{\mathbf{S}}_{23}^{(2)}$ represents the two-mode squeezing operator, which yields an entangled state when acting on vacuum (two-mode squeezed vacuum).

Chapter 3
A Brief Overview of Entanglement Measures of Interest

To determine whether or not the output fields are entangled, we need to choose a convenient measure. The primary measure we will use for this paper and others on this project will be the logarithmic negativity entanglement measure [31]. Later on, in our work, we will utilize at least one more measure. That measure we will call the Duan measure. The variance matrix assembled from the quadrature operators will be the main output to measure entanglement on, thus the variance matrix can be written as follows:

$$\mathbf{V} = \begin{pmatrix} \langle {X_1}^* X_1 \rangle_+ & \langle {X_1}^* Y_1 \rangle_+ & \langle {X_1}^* X_2 \rangle_+ & \langle {X_1}^* Y_2 \rangle_+ \\ \langle {Y_1}^* X_1 \rangle_+ & \langle {Y_1}^* Y_1 \rangle_+ & \langle {Y_1}^* X_2 \rangle_+ & \langle {Y_1}^* Y_2 \rangle_+ \\ \langle {X_2}^* X_1 \rangle_+ & \langle {X_2}^* Y_1 \rangle_+ & \langle {X_2}^* X_2 \rangle_+ & \langle {X_2}^* Y_2 \rangle_+ \\ \langle {Y_2}^* X_1 \rangle_+ & \langle {Y_2}^* Y_1 \rangle_+ & \langle {Y_2}^* X_2 \rangle_+ & \langle {Y_2}^* Y_2 \rangle_+ \end{pmatrix} \tag{3.1}$$

or in block form:

$$V = \begin{pmatrix} V_{11} & V_{12} \\ V_{21} & V_{22} \end{pmatrix}. \tag{3.2}$$

In the above formula, the symmetrized average follows the form:

$$\langle \hat{\mathbf{X}}_j \hat{\mathbf{Y}}_k \rangle_+ = \frac{1}{2} \langle \hat{\mathbf{X}}_j \hat{\mathbf{Y}}_k + \hat{\mathbf{Y}}_k \hat{\mathbf{X}}_j \rangle \ . \tag{3.3}$$

3.1 Logarithmic negativity

Negativity is an "easy-to-compute" measure of entanglement defined as follows:

$$N(\rho) = \frac{||\rho^{\Gamma_A}|| - 1}{2} \ , \tag{3.4}$$

where ρ is the density matrix, A is the dimension of the subsystem, and ρ^{Γ_A} is the partial transpose of ρ with respect to subsystem A [32, 33]. Written with the same dependence

the logarithmic negativity is the following:

$$E_N = log_2||\rho^{\Gamma_A}||_1. \tag{3.5}$$

One of the most beneficial features of this measure is that it is additive for tensor products; meaning, $E_N(\rho_A \otimes \rho_B) = E_N(\rho_A) + E_N(\rho_B)$. It can also be defined as a function of the quadrature covariance matrix (see chapter 5).

3.2 Duan' measure of inseparability

Since the logarithmic negativity is strongly dependent on the normalization, we compute a second entanglement measure, Duan's measure, as a sanity check. Figure 3.1 contrasts the two measures with the results from the calculations discussed in Chapter 5. We chose this measure because it does not deviate from the choice of variance matrix normalization. This entanglement monotone is an alternative to the negativity-based measure for CV entangled beams [34]. The calculation determining the a parameter is dependent on calculations done on the variance matrix V; however, the only variance matrices of certain forms can be used [34]. Fortunately, Duan's work explains how to quantify entanglement from an arbitrary covariance matrix (with arbitrary normalization, for example). Duan's approach involves transforming the given non-standard covariance matrix into their standard forms for robust entanglement quantification. The variance matrix of the standard form (the goal) is written as follows:

$$V'' = \begin{pmatrix} n_1 & & c_1 & \\ & n_2 & & c_2 \\ c_1 & & m_1 & \\ & c_2 & & m_2 \end{pmatrix}. \tag{3.6}$$

These matrix elements are computed from the elements of what we shall call the "substandard form of the variance matrix"; this form shall be written as follows:

$$V' = \begin{pmatrix} n & & c & \\ & n & & c' \\ c & & m & \\ & c' & & m \end{pmatrix}. \tag{3.7}$$

The standard form is calculated from the substandard form by solving the following system of equations for the parameters r_1 and r_2:

$$\sqrt{r_1 r_2}|c| - \frac{|c'|}{\sqrt{r_1 r_2}} = \sqrt{\alpha_n \alpha_m} - \sqrt{(\beta_n \beta_m)} \tag{3.8}$$

$$\frac{\beta_n}{\alpha_n} = \frac{\beta_m}{\alpha_m} \tag{3.9}$$

where $\alpha_n = nr_1 - 1$, $\beta_n = \frac{n}{r_1} - 1$, $\alpha_m = mr_2 - 1$, and $\beta_m = \frac{m}{r_2} - 1$. Then, to apply r_1 and r_2: $n_1 = nr_1,\ n_2 = n/r_2,\ m_1 = mr_1,\ m_2 = mr_2,\ c_1 = c\sqrt{r_1 r_2},\ c_2 = \frac{c'}{\sqrt{r_1 r_2}}$.

Finally, our original variance matrix, V, will be referenced in block form as follows:

$$V = \begin{pmatrix} V_{11} & V_{12} \\ V_{12}^T & V_{22} \end{pmatrix} = \begin{pmatrix} A & B \\ B^T & C \end{pmatrix}. \tag{3.10}$$

Calculating $\mathbf{V}'$ from $\mathbf{V}$ was done using the following equations.

$$\det A = n^2, \quad \det C = m^2, \det B = cc', \tag{3.11}$$

$$\det \mathbf{V} = (nm - c^2)(nm - c'^2) \tag{3.12}$$

After attaining the proper form, the following inequalities need to be broken for there

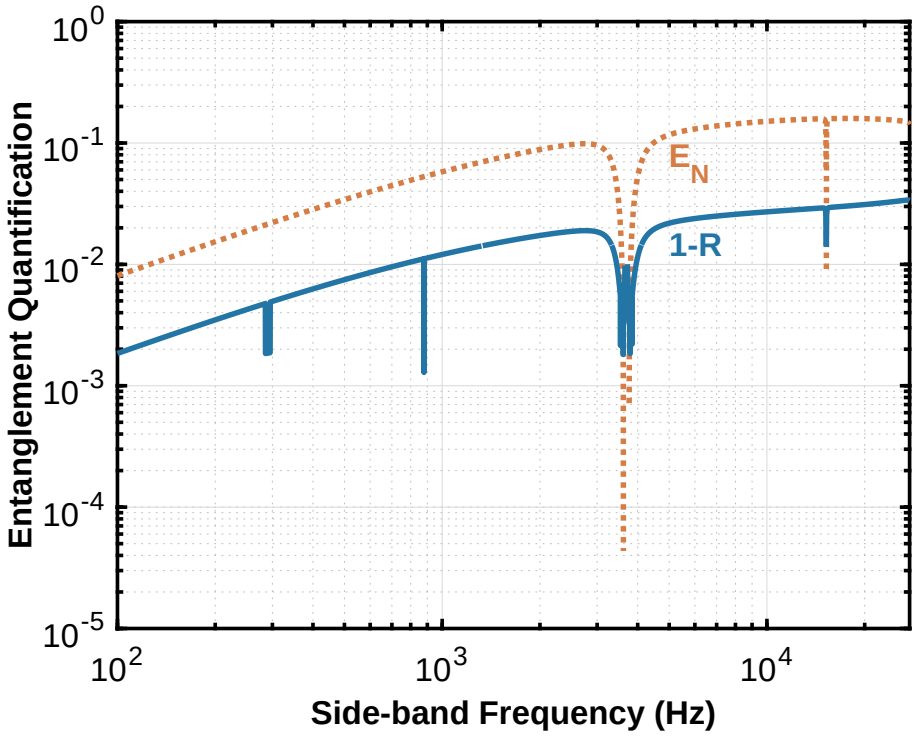

Figure 3.1: Duan measure $1-R$ and logarithmic negativity E_N versus side-band frequency. For this measure, higher values correspond to stronger entanglement. Both at T = 295 K. The dips in the Duan measure are due entirely to numeric instabilities from our parameter space.

to be entanglement in the system:

$$|c_1| \leq \sqrt{(n_1 - 1)(m_1 - 1)} \tag{3.13}$$

$$|c_2| \leq \sqrt{(n_2 - 1)(m_2 - 1)} \tag{3.14}$$

To compare Duan's measure with logarithmic negativity, we use the following form of the metric inequality representing Duan's measure:

$$R = \frac{\frac{a^2(n_1+n_2)}{2} + \frac{(m_1+m_2)}{2a^2} - |c_1| - |c_2|}{a^2 + a^{-2}} \geq 1$$

where $a^2 = \sqrt{\frac{m_1-1}{n_1-1}}$. The system is separable only when this inequality is satisfied. The plot of the two entanglement measures versus the side-band frequency is depicted in figure 3.1.

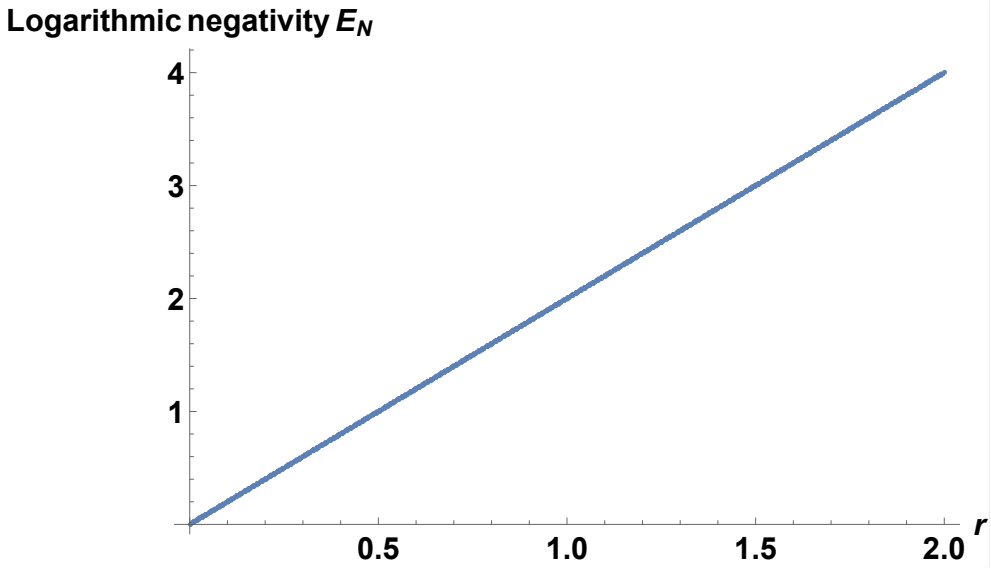

Figure 3.2: This is a plot of the output entanglement (E_N) versus the input squeezing strength ($r/2$) of one single-mode squeezed coherent state incident on a 50:50 beam splitter. A notable feature for comparison to OMC entanglement methods is the low squeezing region, see chapter 6.

3.3 Optical entanglement generation example

When one single-mode squeezed coherent beam is incident on a 50:50 beam splitter, the result is the tensor product state. That state consists of a two-mode squeezed state and two single-mode squeezed states (see equation 2.29). Thus, the logarithmic negativity between the two beam splitter outputs (due to the logarithmic negativity's additivity) is equivalent to the logarithmic negativity of a two-mode squeezed state. Later in this work, this two-mode squeezed state generation method is used to compare the efficacy of new entangling techniques. Figure 3.2 plots the output Logarithmic negativity versus the strength of the input squeezing.

Chapter 4
Introduction to Quantum Cavity Optomechanics

Optomechanical cavities are optical cavities with at least one mechanical mode coupled to at least one intracavity optical mode. The inclusion of these coupled mechanical modes elicits rich dynamics in the optical cavities. The following is a quick introduction to the field of optomechanics. We discuss the basics necessary to understand the experiments that follow this chapter.

4.1 Optical cavities

An optical cavity (also referred to as an optical resonator or a resonating cavity) is an optical device that temporarily traps incoming light. This temporary confinement causes an amplification in the cavity fields. The most common form of the optical cavity is the Fabry-Perot cavity. These devices utilize two flat mirrors to trap and amplify input light. While the amplification only occurs inside the cavity, this temporary boost in intensity is still useful for many applications. The optical resonator's ability to host longitudinal optical states closely ties quantum optics and optical resonators (see chapter 2).

The physics of the stationary optical cavity (here meaning, without a mechanical resonator) is highly relevant to the quantum optomechanical descriptions that are seen in the Quantum Langevin approach to quantum cavity optomechanics. In particular, the input output theory provides a quantum mechanical framework for understanding optical cavity reflection and/or transmission. Traditionally, input output theory is written in Heisenberg's picture of quantum mechanics. It establishes direct relationships between the intracavity and extracavity (exocavity) optical field operators:

$$\dot{\hat{\mathbf{a}}}_c = -\kappa/2\hat{\mathbf{a}}_c + i(\omega_\alpha - \omega_c)\hat{\mathbf{a}}_c + \sqrt{\kappa_x}\hat{\mathbf{a}}_n + \sqrt{\kappa_0}\hat{\mathbf{a}}_\ell \ ; \tag{4.1}$$

where: $\hat{\mathbf{a}}_c$ is the intracavity field operator, $\hat{\mathbf{a}}_N$ is the input field operator, κ_x is the loss rate due to the input mirror of the cavity, and κ_0 is the optical loss rate in the rest of the cavity;

thus the total cavity loss rate is their sum: $\kappa = \kappa_0 + \kappa_x$. Moreover, the theory describes the relationship of the intracavity light to the out going light as $\hat{\mathbf{a}}_{\text{out}} = \hat{\mathbf{a}}_{\text{n}} - \sqrt{\kappa_x}\hat{\mathbf{a}}$, and it also establishes the input power photon number as $P \propto \langle \hat{\mathbf{a}}_N^\dagger \hat{\mathbf{a}}_N \rangle$. The terms $\hat{\mathbf{a}}_N, \hat{\mathbf{a}},$ and $\hat{\mathbf{a}}_{\text{out}}$ are the ladder operators that correspond to the input field, the intracavity field, the output field respectively.

4.2 Optomechanical cavities

An optomechanical cavity (OMC) is an optical cavity that includes a mechanical oscillator that is coupled to the intracavity electromagnetic field. For our discussions we are primarily concerned with the physics of Fabry-Perot cavities with movable endmirrors as the mechanical oscillator. These types of OMC's couple the optical to mechanical fields via the momentum transfer that comes from the intracavity radiation pressure. Since this is the only mode of interaction between the mechanical and optical fields we can , from this, write the radiation pressure force and its relation to the interaction Hamiltonian:

$$\langle \hat{\mathbf{F}} \rangle = \frac{\hbar\omega}{L} \langle \hat{\mathbf{a}}_c^\dagger \hat{\mathbf{a}}_c \rangle \;=\; -\langle \frac{d\mathbf{H}_{int}}{d\hat{\mathbf{x}}_\mu} \rangle \tag{4.2}$$

$$\mathbf{H}_{int} \approx C_0 - \frac{\hbar\omega \hat{\mathbf{a}}_c^\dagger \hat{\mathbf{a}}_c}{L\hat{\mathbf{x}}_\mu} \; . \tag{4.3}$$

This type of optomechanical interaction creates a dynamical back action on the intracavity fields. The dynamical back action causes the mechanical oscillator's resonance frequency to change with the optical field frequency, optical losses, and the mechanical oscillator frequency. Moreover, these effects lend to the physics of the optical spring. More information on the physics of ideal OMC and the optical spring effect can be found the references [19, 24, 15, 35, 36]. One area of study involves the inclusion or consideration of the cavity end mirror's response to the amplified radiation pressure. This phenomenon boasts a rich physics that deeply extends into cutting-edge quantum technology research.

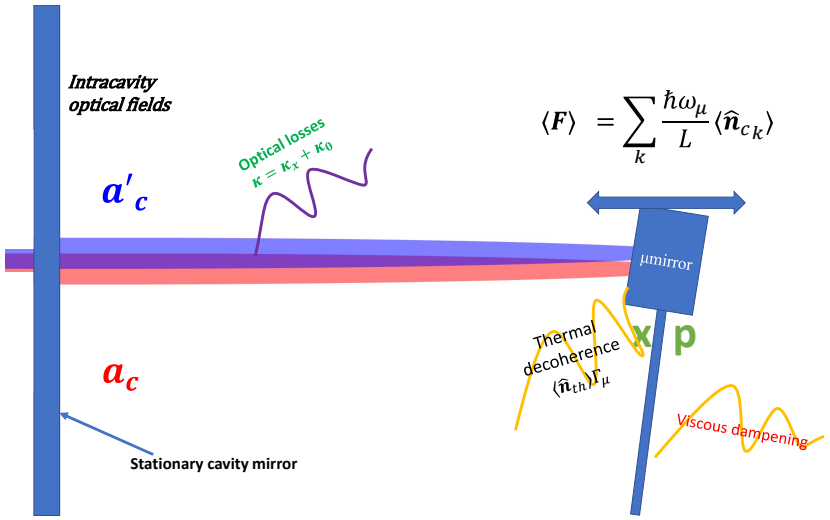

Figure 4.1: This figure depicts a cartoon of an optomechanical cavity with two intracavity fields (red and blue not indications of detuning here) cantilever shaped movable end mirror here marked μmirror. The OMC that we simulate exhibits viscous dampening due to its size. A thin rod (acts as a heat pipe) maintains the endmirror's (mechanical oscillator's) temperature. It connects the head of the cantilever mirror and a coolable heatsink. The decoherence rate depends on temperature, which we can control in our simulations (Chapters 5-7).

4.2.1 Optical springs

For a movable endmirror optical cavity, the restoring force for the endmirror with no optical fields considered to follow Hooke's law for small vibrations in position from the rest position. For equilibrium mirror position $x = 0$ the potential energy of the mechanical oscillator is $V_0(x) = m\Omega^2 x^2/2$. Considering the intracavity optical fields complicates the physics. The mechanical oscillator responds to the applied radiation pressure from the intracavity circulating fields. Thus, changing the oscillator potential function to:

$$V(x) = V_0(x) + V_R(x); \tag{4.4}$$

where $V_R(x) = \frac{\partial F_R}{\partial x}$ is the potential that comes from the radiation pressure force. Thus, changing the equilibrium position to x_0, where $x_0 = x$ when $\frac{\partial V_0}{\partial x}(x) = -\frac{\partial V_R}{\partial x}(x)$. This phenomenon can be understood as changing the effective spring constant of the endmirror. In other words, after considering the change to the rest position of the endmirror, two springs are acting in series; the original restoring action from the mechanical oscillators restoring force (with potential V_0) and the new restoring action from the optical field's force on the endmirror. This is called the Optical spring effect. The new effective spring constant k_e follows:

$$k_e = m\Omega^2 + \frac{\partial^2 V_R}{\partial x^2}(x)|_{x=x_0} \ . \tag{4.5}$$

This effect gives rise to other phenomena such as bistable oscillation and optical cooling (of the mechanical oscillator) in the red-detuned regime ($\omega_\alpha - \omega_c < 0$), unstable oscillation, and optical heating in the blue-detuned regime (see reference [24, 19]), and (when considering the dynamic back-action as well) frequency dependency shifts to the effecting mechanical dampening and oscillating frequency (see references).

4.3 The optomechanical Hamiltonian

A salutary approach for understanding the quantum dynamics of a generic OMC begins with the optomechanical Hamiltonian. Guessing the form from the preceding radiation force equation and considering the free-photon and free-phonon Hamiltonians. The following is a Hamiltonian of a 1-dimensional optical cavity with a moving end mirror (cavity length depends on the position, x, of end mirror):

$$H = \hbar\omega_c(\mathbf{x})\hat{\mathbf{a}}^\dagger\hat{\mathbf{a}} + \hbar\omega_{mech}\hat{\mathbf{b}}^\dagger\hat{\mathbf{b}} + i\hbar\mathbf{E}(e^{i\omega_\alpha t}\hat{\mathbf{a}} - e^{-i\omega_\alpha t}\hat{\mathbf{a}}^\dagger); \tag{4.6}$$

where $\hat{\mathbf{a}}$ and $\hat{\mathbf{b}}$ are the annihilation operators for the intracavity photon field and the movable endmirror's phonon modes respectively; $\mathbf{E}$ is the carrier electric field, ω_α is the frequency of the carrier, and t is time. This Hamiltonian considers the endmirror's behavior as quantum, the perhaps more adaptable version of this Hamiltonian is $H = \hbar\omega_c(\mathbf{x})\hat{\mathbf{a}}^\dagger\hat{\mathbf{a}} + \hat{\mathbf{p}}^2/(2m_\mu) + i\hbar\mathbf{E}(e^{i\omega_\alpha t}\hat{\mathbf{a}} - e^{-i\omega_\alpha t}\hat{\mathbf{a}}^\dagger)$. Furthermore, in our work or endmirror has a restoring force that follows Hookee's law, this adds $1/2m_\mu\omega_\mu\hat{\mathbf{x}}_\mu^2$ to the Hamiltonian.

Since the cavity frequency, ω_c, is dependent on cavity length it depends on the cavity endmirror's position operator $\hat{\mathbf{x}}$:

$$\omega_c(\hat{\mathbf{x}}) = \frac{2\pi c}{L + \hat{\mathbf{x}}} = 2\pi c\sum_{n=0}^{\infty}(-1)^n L^{-n-1}\hat{\mathbf{x}}^n \ , \tag{4.7}$$

where L is the cavity length with the endmirror at the "rest" position ($x = 0$) and c is the intracavity speed of light. Though there are some interesting and important effects that call attention to the higher order terms in the series, typically, quadratic and higher order terms are ignored [37].

So far, the Hamiltonian describes the cavity's physics, but we are concerned with noise effects specifically. In systems with sufficient input power versus the mechanical oscillator's inertia, the systems can act as a classical steady-state with fluctuations, in that steady-

state, due to quantum and thermal noises. The quantum noise in the input light drives the quantum behavior of the cavity. To begin, we assume that the quantum noise in the optical and mechanical fields can be represented by the quadrature mode operator $\delta\hat{\mathbf{a}}$ such that the total mode operator $\hat{\mathbf{a}}$ is then rewritten [24]:

$$\hat{\mathbf{a}} -> \hat{\mathbf{a}}_0 \; + \; \delta\hat{\mathbf{a}} \tag{4.8}$$

Furthermore, we can exclude the time dependence terms by switching to a rotating frame of reference (at frequency ω_α); since the $\hat{\mathbf{a}}^\dagger\hat{\mathbf{a}}$ terms ultimately yield a constant factor of α^2, we omit that factor by reestablishing the μmirror rest position to account for this radiation pressure constant. The Hamiltonian becomes

$$H = \hbar(\omega_\alpha - \omega_0)\delta\hat{\mathbf{a}}^\dagger\delta\hat{\mathbf{a}} + \hbar\omega_m\hat{\mathbf{b}}^\dagger\hat{\mathbf{b}} - \frac{2\pi\omega_0\gamma_c\alpha\hbar}{L\mathscr{F}(\omega_m)}(\delta\hat{\mathbf{a}}^\dagger + \delta\hat{\mathbf{a}})(\hat{\mathbf{b}}^\dagger + \hat{\mathbf{b}}), \tag{4.9}$$

where $\mathscr{F}(\omega_m)$ is a function that accounts for the higher order modes in the mechanical oscillator (when the sideband frequency, ω_m, equals a higher mode frequency the function goes to zero).

4.4 Correlations in optomechanics

Cavity optomechanics allows for the generation of quantum correlations between the oscillator and the intracavity optical field [24]. The amplitude variations from each input field in the OMC induces variations in the end mirror position. The quantum dynamical back action then imprints those variations onto the intracavity optical field's phases. Since both fields receive fluctuations from each other, the output fields are correlated. This phenomenon can present as phase noise in most interferometers. The phase noise is caused by the fluctuations in input power fluctuating the overall cavity length, which encodes this noise (or fluctuations) in the outgoing light phase. However, via the application of quantum cavity optomechanics, the phenomena can be exploited as a source for quantum light,

such as squeezed light [23]. The optomechanical phase noise limited the Laser Interferometer Gravitational-wave Observatory 's (LIGO's) measurements. Recently, LIGO upgraded their facility to include squeezed light to reduce the quantum back-action effects on the phase measurements (these measurements are critical in an interferometer). This implementation of quantum technologies significantly increased the overall sensitivity of their gravity wave detector [38, 39]. These methods involve injected squeezed light to reduce the effects of the optomechanical interaction but injecting squeezed light can also boost the quantum behavior of the OMC (see Chapter 6). We should capitalize on a weakness anytime can be turned into a strength. We have this opportunity with quantum cavity optomechanics. One of the most interesting of the quantum effects that spawn from the three-wave mixing in quantum noise-dominated OMCs is the emission of entangled optical fields from the OMC.

4.5 Research in optomechanical entanglement

Entanglement is the most common resource for quantum technologies, from quantum metrology [40], to quantum communication [41] and quantum computing [42, 43]. Quantum light sources, in particular entangled sources, require nonlinear interaction [44]. To date, most of these sources are based on all-optical nonlinear processes in crystals [45], which are good enough for most applications, but insufficient for applications with very short wavelengths [46]. Exploring different avenues to generate quantum entanglement is a consistent topic of interest in the quantum technology research community [47, 11, 10, 48]. One approach is to use strong light-matter interaction with single atoms [47] or single quantum dots [11]. While this method is very efficient, it is limited to a single entangled pair at a time. A reliable source of entanglement which does not require a high-intensity field and provides multi-photon entanglement is still in need.

Radiation pressure — the force electromagnetic radiation exerts on a material surface — is a significant source of noise in optical metrology [49]. The light's momentum causes fluctuations in the mirror's position, yielding phase noise in the electromagnetic

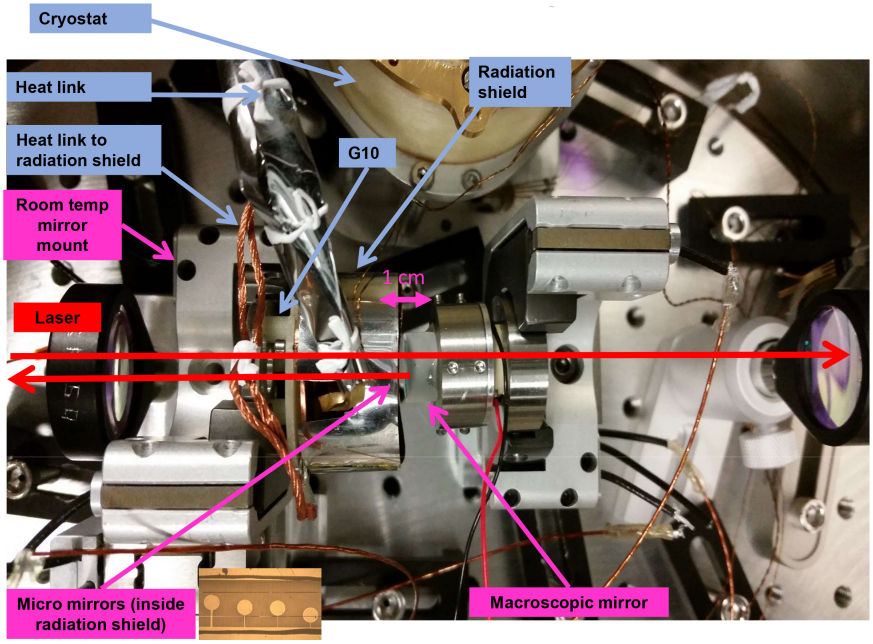

Figure 4.2: Labeled image of the OMC in LSU optics laboratory. This setup was used to obtain thermal and quantum noise measurements used in the simulations [19].

wave. However, exploiting this interaction could produce light with squeezed or entangled light. When an electromagnetic wave is incident on a movable micromirror, it experiences an optical nonlinearity which can yield squeezed light[50]. The same process can generate entanglement between the light and the micromirror [14]. However, if two light sources are used, the entanglement can be swapped such that the two light sources are entangled [35, 16]. This work numerically evaluates the amount of entanglement produced by simulating two coherent light fields on one micromirror under realistic experimental conditions. Furthermore, we aim to investigate the entanglement's dependence on various experimental parameters like temperature, sideband frequency, cavity length, and loss. Ponderomotive entanglement is an entanglement generation technique that exploits optomechanical coupling. This coupling is traditionally a noise source in most optical measurements; the radiation pressure noise. To enhance the effect of the radiation pressure and quantum back action, we consider a homodyne quadrature variance measurement of two optical output fields from a single cavity double optical spring; quantum back action is further enhanced

by utilizing a very small mirror in the cavity (μmirror). Here, we report the prediction of an experimentally feasible parameter configuration that allows for observable entanglement at room temperature and lower. Furthermore, based on programs and foundations that have been previously tested and reported [20, 19], we can predict continuous-variable entanglement between two Gaussian beams using only one optical cavity and micro-mirror with realistic losses. These relationships between output entanglement and laboratory parameters will be discussed further in the subsequent chapter. Let us next present the theory behind optomechanical entanglement through the use of the Quantum Langevin equations.

4.5.1 Before the Quantum Langevin Equations

To begin and find the correct form of the Quantum Langevin Equations, we start with the system's Hamiltonian.

Commence with the OMC Hamiltonian with the restoring force term and only the linear term in the expansion for the mechanical oscillator's Brownian motion $\omega_c(\hat{\mathbf{x}}_\mu)$, and in the rotating reference frame:

$$H = \hbar(\omega_\alpha - \omega_0)\hat{\mathbf{a}}^\dagger\hat{\mathbf{a}} + \hbar\omega_\mu\hat{\mathbf{b}}^\dagger\hat{\mathbf{b}} + \frac{1}{2}\hbar\omega_\mu^2 - \hbar g\hat{\mathbf{a}}^\dagger\hat{\mathbf{a}}\hat{\mathbf{x}}_\mu \ , \tag{4.10}$$

where: $\hat{\mathbf{a}}^\dagger\hat{\mathbf{a}} = \hat{\mathbf{n}}$. These will be used interchangeably for the photon fields only unless otherwise specified, the optomechanical interaction term is $H_{\text{int}} = -\hbar g\hat{\mathbf{n}}\hat{\mathbf{x}}_\mu$, the free photon component is $H_0 = \hbar\omega_0\hat{\mathbf{n}}$, the mechanical oscillator in the simple harmonic potential is $H_\mu = \hbar\omega_\mu\hat{\mathbf{b}}^\dagger\hat{\mathbf{b}} + \frac{1}{2}m_\mu\omega_\mu\hat{\mathbf{x}}_\mu^2$. The Quantum Langevin method describes the how the intracavity operators evolve in time. Therefore, we are interested in the time derivatives of the operators: $\hat{\mathbf{x}}_\mu, \hat{\mathbf{X}}, \hat{\mathbf{Y}}, \hat{\mathbf{p}}$; where $\hat{\mathbf{X}}$ and $\hat{\mathbf{Y}}$ are the optical quadrature operators described in eqn 2.17. Applying Heisenberg's equations (for arbitrary operator $\hat{\mathbf{A}}$ $\dot{\hat{\mathbf{A}}} = \frac{i}{\hbar}[\mathbf{H}, \hat{\mathbf{A}}(t)] + (\frac{\partial\hat{\mathbf{A}}}{\partial t})_H$)

yields (let $\hat{\mathbf{x}}_\mu = \hat{\mathbf{x}}$):

$$\dot{\hat{\mathbf{x}}} = \frac{i}{\hbar}[\mathbf{H}, \hat{\mathbf{x}}] = \frac{\hat{\mathbf{p}}}{m}, \tag{4.11}$$

$$\dot{\hat{\mathbf{p}}} = -m\omega_\mu^2 \hat{\mathbf{x}} + \hbar g \hat{\mathbf{n}}, \tag{4.12}$$

$$\dot{\hat{\mathbf{a}}} = ig_1(1 - \hat{\mathbf{x}}) + ... \tag{4.13}$$

Using these equations to form the optical quadrature operators and arranging them into the covariance matrix form will lead to the Quantum Langevin equations and a coupling matrix $\mathbf{K}$.

4.5.2 Quantum Langevin Approach

The mathematics describing the entangling process that occurs in the cavity are, so far, best explained by the quantum Langevin equations. Most of the parameters specific to the optical cavity are contained in the coupling matrix, $\mathbf{K}$. The intracavity fields are considered within the Heisenberg picture, thus to describe the field's evolution we must identify the relevant operators. The coordinate operators of the intracavity field are contained in the vector $\mathbf{u}_c$. To cleanly model the noises in our system we assume the injection of noise in to our cavity as the addition of a set of noise operators confined to the vector $\mathbf{u}_N$, the input noise coordinate vector. This means:

$$\mathbf{u}_c = [q, p, X_{c1}, Y_{c1}, X_{c2}, Y_{c2}]^T \ , \tag{4.14}$$

$$\mathbf{u}_N = [0, F_{th}, X_{N1}, Y_{N1}, X_{N2}, Y_{N2}]^T \ , \tag{4.15}$$

$$\text{and } \mathbf{K} = \begin{pmatrix} 0 & 1/m & 0 & 0 & 0 & 0 \\ -m\omega_m^2 & -\gamma_m & \hbar G_1 & 0 & \hbar G_2 & 0 \\ 0 & 0 & -\frac{\gamma_c}{2} & -\Delta_1 & 0 & 0 \\ G_1 & 0 & \Delta_1 & -\frac{\gamma_c}{2} & 0 & 0 \\ 0 & 0 & 0 & 0 & -\frac{\gamma_c}{2} & -\Delta_2 \\ G_2 & 0 & 0 & 0 & \Delta_2 & -\frac{\gamma_c}{2} \end{pmatrix} \ . \tag{4.16}$$

The mirror resonance frequency is ω_m, m is the mass of the movable mirror, γ_c is the cavity linewidth, and G_1, G_2 are the optomechanical couplings; while Γ_m is the movable mirror dampening rate. Also, the detunings are $\Delta_n = -\omega_n + \omega_c(1 - \frac{\langle q \rangle}{L})$. When ω_c is the cavity resonance frequency, the optomechanical couplings can be written as follows: $G_n = 2\sqrt{\frac{I_n \gamma_c \omega_c}{\hbar L^2(\gamma_c^2 + \Delta_n^2)}}$. With these elements, one can describe in the Heisenberg picture of quantum mechanics the dynamics that entangle the two Gaussian fields. The quantum Langevin equations that do so are as follows:

$$\dot{\mathbf{u}}_c = \mathbf{K}\mathbf{u}_c + \mathbf{u}_N. \tag{4.17}$$

To solve this differential matrix equation we can conveniently transform to the side-band frequency-space:

$$-i\Omega\widetilde{\mathbf{u}}_c = \mathbf{K}\widetilde{\mathbf{u}}_c + \widetilde{\mathbf{u}}_N \ , \tag{4.18}$$

$$-[\mathbf{K} + i\Omega\mathbf{I}]\mathbf{u}_c = \mathbf{u}_N \ . \tag{4.19}$$

Here, we have taken $\widetilde{\mathbf{u}}_c - > \mathbf{u}_c$, etc..Since our goal is to calculate the variance matrix for our measurements we can shape the solution for the equation into a form most appropriate for the calculations by considering the outer product of the intracavity coordinate vector and the input-output relation for the system. The input output relation is

$$\hat{\mathbf{a}}_{out} = \sqrt{2\gamma_c}\hat{\mathbf{a}}_c - \hat{\mathbf{a}}_N \ , \tag{4.20}$$

where the quadratures are defined as $\hat{\mathbf{X}} = \frac{\hat{\mathbf{a}} + \hat{\mathbf{a}}^\dagger}{2}$ and $\hat{\mathbf{Y}} = \frac{\hat{\mathbf{a}} - \hat{\mathbf{a}}^\dagger}{2i}$. After considering these equations, the expectation of the outer product of the output field should yield the variance matrix of the output field; to illustrate we write the outer product of the output field as

follows:

$$\mathbf{v} \otimes \mathbf{v}^\dagger = \begin{pmatrix} \hat{\mathbf{X}}_1^* \hat{\mathbf{X}}_1 & \hat{\mathbf{X}}_1^* \hat{\mathbf{Y}}_1 & \hat{\mathbf{X}}_1^* \hat{\mathbf{X}}_2 & \hat{\mathbf{X}}_1^* . \hat{\mathbf{Y}}_2 \\ \hat{\mathbf{Y}}_1^* \hat{\mathbf{X}}_1 & \hat{\mathbf{Y}}_1^* \hat{\mathbf{Y}}_1 & \hat{\mathbf{Y}}_1^* \hat{\mathbf{X}}_2 & \hat{\mathbf{Y}}_1^* \hat{\mathbf{Y}}_2 \\ \hat{\mathbf{X}}_2^* \hat{\mathbf{X}}_1 & \hat{\mathbf{X}}_2^* \hat{\mathbf{Y}}_1 & \hat{\mathbf{X}}_2^* \hat{\mathbf{X}}_2 & \hat{\mathbf{X}}_2^* \hat{\mathbf{Y}}_2 \\ \hat{\mathbf{Y}}_2^* \hat{\mathbf{X}}_1 & \hat{\mathbf{Y}}_2^* \hat{\mathbf{Y}}_1 & \hat{\mathbf{Y}}_2^* \hat{\mathbf{X}}_2 & \hat{\mathbf{Y}}_2^* \hat{\mathbf{Y}}_2 \end{pmatrix}. \tag{4.21}$$

The Quantum Langevin equation and the input-output relation allow us to (somewhat) directly write the variance matrix in terms of the coupling matrix, the sideband frequency (Ω), and the outer product of the input noise vector. Conveniently, the input noise vector's outer product with its Hermitian conjugate is also the input noise's correlation spectra.

Mathematically, from equation 4.19, write,

$$\mathbf{u}_c = -[\mathbf{K} + i\Omega\mathbf{I}]^{-1}\mathbf{u}_N. \tag{4.22}$$

Then, let $\mathbf{M} = [\mathbf{K} + i\Omega\mathbf{I}]^{-1}$, and write the outer product of the intracavity space with its Hermitian conjugate:

$$\mathbf{u}_c \otimes \mathbf{u}_c^\dagger = \mathbf{M}\ \mathbf{u}_N \otimes \mathbf{u}_N^\dagger\ \mathbf{M}^\dagger \tag{4.23}$$

$$= \mathbf{M}\ \mathbf{G}\ \mathbf{M}^\dagger, \tag{4.24}$$

where $\mathbf{G} = \mathbf{u}_N \otimes \mathbf{u}_N^\dagger$. Next, apply the transformation of $\mathbf{u}_c$ to $\mathbf{v}$ (the output field coordinate vector). Next, we consider the input-output relation and how it transforms $\mathbf{u}_c -> \mathbf{v}$:

$$\mathbf{v} = \sqrt{2\gamma_c}\mathbf{u}_c - \mathbf{u}_N \tag{4.25}$$

$$\mathbf{v} \otimes \mathbf{v}^\dagger = 2\gamma_c \mathbf{u}_c \otimes \mathbf{u}_c^\dagger + \mathbf{u}_N \otimes \mathbf{u}_N^\dagger \tag{4.26}$$

$$-\sqrt{2\gamma_c}(\mathbf{u}_c \otimes \mathbf{u}_N^\dagger + \mathbf{u}_N \otimes \mathbf{u}_c^\dagger) \tag{4.27}$$

The first half of $\mathbf{v} \otimes \mathbf{v}^\dagger$ is a simple substitution to $\mathbf{v} \otimes \mathbf{v}^\dagger = \mathbf{M}\ \mathbf{G}\ \mathbf{M}^\dagger + \mathbf{G} - ...$; however, the next two terms require an additional step to simplify.

$$\mathbf{u}_c \otimes \mathbf{u}_N^\dagger = -\mathbf{M}\ \mathbf{u}_N \otimes \mathbf{u}_N^\dagger \tag{4.28}$$

$$= -\mathbf{M}\ \mathbf{G}; \tag{4.29}$$

and likewise for its complex conjugate, $\mathbf{u}_N \otimes \mathbf{u}_c^\dagger = -\mathbf{G}\ \mathbf{M}^\dagger$. Finally, we may write the variance matrix as a function of the input noise spectra and the sideband frequency as follows:

$$\langle \mathbf{v} \otimes \mathbf{v}^\dagger \rangle = \langle 2\gamma_c \mathbf{M}\ \mathbf{G}\ \mathbf{M}^\dagger + \mathbf{G} + \sqrt{2\gamma_c}(\mathbf{M}\ \mathbf{G} + \mathbf{G}\ \mathbf{M}^\dagger) \rangle\ , \tag{4.30}$$

while recalling $\mathbf{V} = \frac{1}{2}(\langle \mathbf{v} \otimes \mathbf{v}^\dagger \rangle\ +\ \langle \mathbf{v}^\dagger \otimes \mathbf{v} \rangle)$.

Also, the correlation spectra is:

$$\langle \mathbf{G} \rangle = \begin{pmatrix} 0 & 0 & 0 & 0 & 0 & 0 \\ 0 & \frac{\gamma_m \Omega \left(\coth\left(\frac{\hbar\Omega}{2k_B T}\right) - 1 \right)}{\omega_m} & 0 & 0 & 0 & 0 \\ 0 & 0 & \frac{1}{2} & \frac{i}{2} & 0 & 0 \\ 0 & 0 & -\frac{i}{2} & \frac{1}{2} & 0 & 0 \\ 0 & 0 & 0 & 0 & \frac{1}{2} & \frac{i}{2} \\ 0 & 0 & 0 & 0 & -\frac{i}{2} & \frac{1}{2} \end{pmatrix}\ . \tag{4.31}$$

Then recalling that $\mathbf{M}$ is not a matrix of operators we can simplify to the following:

$$\mathbf{V} = 1/2(2\gamma_c \mathbf{M}\langle \mathbf{G} \rangle \mathbf{M}^\dagger + \langle \mathbf{G} \rangle + \sqrt{2\gamma_c}(\mathbf{M}\langle \mathbf{G} \rangle + \langle \mathbf{G} \rangle \mathbf{M}^\dagger) + ...\ ; \tag{4.32}$$

which can be further simplified to the following:

$$\mathbf{V} = \frac{1}{2}(\mathbf{Q}\langle\mathbf{G}\rangle\mathbf{Q}^\dagger \ + \ \mathbf{Q}^\dagger\langle\mathbf{G}\rangle\mathbf{Q}), \tag{4.33}$$

$$\text{or } \mathbf{V} = Re(\mathbf{Q}\langle\mathbf{G}\rangle\mathbf{Q}^\dagger) \tag{4.34}$$

$$\text{where } \ \mathbf{Q} = \sqrt{2\gamma_c}\mathbf{M} + \mathbf{I}. \tag{4.35}$$

This form can be directly used to calculated entanglement (see Chapter 3).

4.6 Computational methods in optomechanics

When simulating tabletop experiments of effects like temperature-sensitive ponderomotive squeezing, optomechanical entanglement, quantum back-action, etc., the choice of theoretical and computational framework is critical. For fast order of magnitude simulations of ideal systems, the Quantum Langevin approach is more than ideal. However, in long-term experimental projects that require performing several (similar) experiments to finish the project, then the two-photon formalism adaptation (2PF) by Thomas Corbitt et al. is the most promising. Both have their strengths and weaknesses, yet preparing complicated simulations of quantum optomechanics is not straightforward. In both computational/theoretical frameworks, matrices need to be inverted to solve the system. These matrices are mostly expensive to invert computationally. These computational expenses imply that higher precision (and in many cases different commands) is (are) necessary to calculate the inverse accurately. Moreover, the Quantum Langevin (QL) methods are most advantageous when working with lossless ideal circumstances. In this methodology, the inversion problems can be mostly avoided by switching to natural units.

However, in the 2PF methods, a different (likely not entirely stable/achievable) parameter space must be used to avoid significant numerical instabilities (at losses within two orders of magnitude see chapter 6 and the appendix were dropping the losses to 1% of lab losses eliminated the numerical noise that obscured our results).

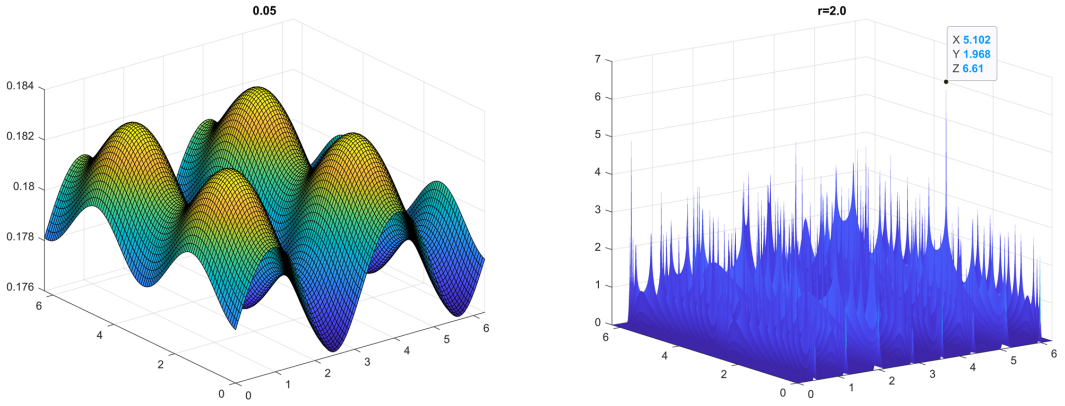

Figure 4.3: Qualitative comparison of two parameter sets that differ only in the squeezing parameter set for the light injected into the OMC. When considering more realistic conditions the simulation fails at strong squeezing strengths $r > 1$.

4.6.1 Quantum Langevin

Although it can be well adapted to simulate loss and other laboratory conditions, the QL approach shines when such complications are not considered. Losses and noises are tricky to work into these methods because of the QL's close reliance on the Hamiltonian and Quantum master equations; in other words, it is more challenging to use such methods in open systems.

4.6.2 Adapted Two-Photon Formalism

The adapted two-photon formalism is an approach that more easily allows for high modularity in the simulation programs. Here high modularity means that a program written in this framework can be modified more promptly to address major or minor changes to the simulated experiment. In other words, when the experiment is changed or the apparatus is altered, the code can be readily edited to compensate (this modularity is loosely captured in figure 4.4). Moreover, this approach relies on operator transformations, the go-to method in photonics. It may be more intuitive to most (especially those without a strong background in quantum mechanics but with some knowledge of advanced electromagnetism).

Furthermore, this method allows for the inclusion of losses and noise easier than the Hamiltonian methods. The simulation of an OMC with two intracavity fields that both interact with a single mechanical mode. This is depicted in figure 4.4. These fields only affect each other through the mechanical mode; thus, the OM coupling is critical to producing bipartite quantum effects.

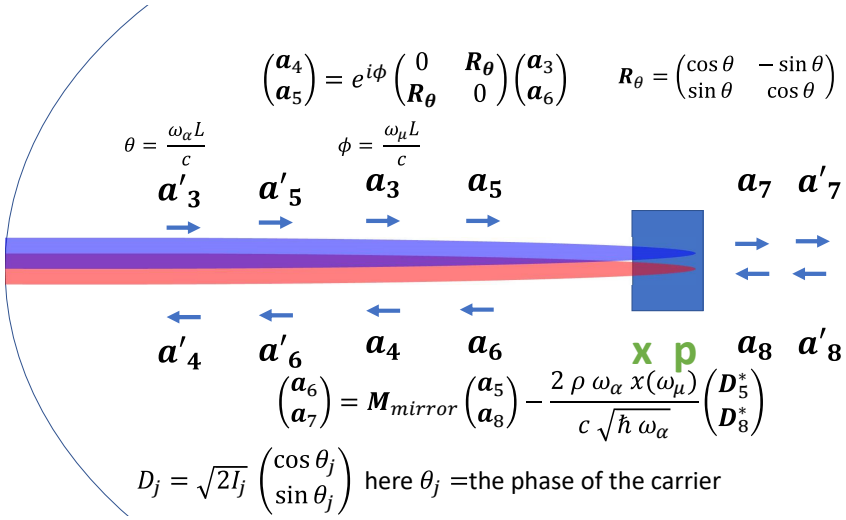

Figure 4.4: Above the prime operators correspond to a second intracavity field. This figure is a diagram of an optomechanical cavity with (blue) a movable end mirror with fluctuating position and momentum (x and p). The equations that transform the intracavity fields in the two-photon formalism are included in the diagram. Here $x(\omega_\alpha)$ are the sideband frequency-dependent position measurements that our group has obtained. These measurements help incorporate effects like thermal noise and higher-order vibration modes when simulating the optomechanical cavity. Note that even for two intracavity fields, there is only a single mechanical mode. Thus, each optical mode couples to the mechanical mode, which determines the overall interaction between the optical modes.

Chapter 5
Room Temperature Optomechanical Entanglement

To observe the effect of the quantum back action between the two light fields, we consider a homodyne quadrature variance measurement of two output optical fields from a single cavity double optical spring with a μmirror. We examine the experimental feasibility of observable ponderomotive entanglement in a cantilever μmirror type optomechanical cavity at room temperature and lower temperature. This work identifies experimental configurations that will yield observable entanglement using programs, designs, and measurements that have been previously reported [51, 52, 19]. We numerically evaluate the amount of entanglement and investigate the dependence of entanglement on various experimental parameters such as temperature, side-band frequency, cavity length, and loss. This is the first work to consider such realistic experimental conditions in a computational framework; thus, we predict the efficacy of such an entanglement generation as techniques develop minimizing losses and noises.

5.1 Methods

5.1.1 Experimental considerations

The experimental setup considered is shown in figure 5.1. This configuration allows for a stable optomechanical system with no external feedback, which could disrupt the entanglement. It utilizes a single optomechanical cavity, that (when two optical fields are input) acts as a double optical spring. This setup will convert the squeezing effects of the optical spring cavity into entanglement. Measuring this form of entanglement requires dual homodyne detection to properly measure the squeezing correlations (see Appendix). The two lasers are frequency locked in order to maintain their relative detunings with respect to the cavity resonance. The laser fields are arranged with orthogonal relative polarizations.

In order to accurately predict entanglement generation from the μmirror cavity we take into account: temperature, cavity loss, laser power, and optical spring detunings. Concurrently, we restrict the optical detuning to maintain a stable optical spring; while including

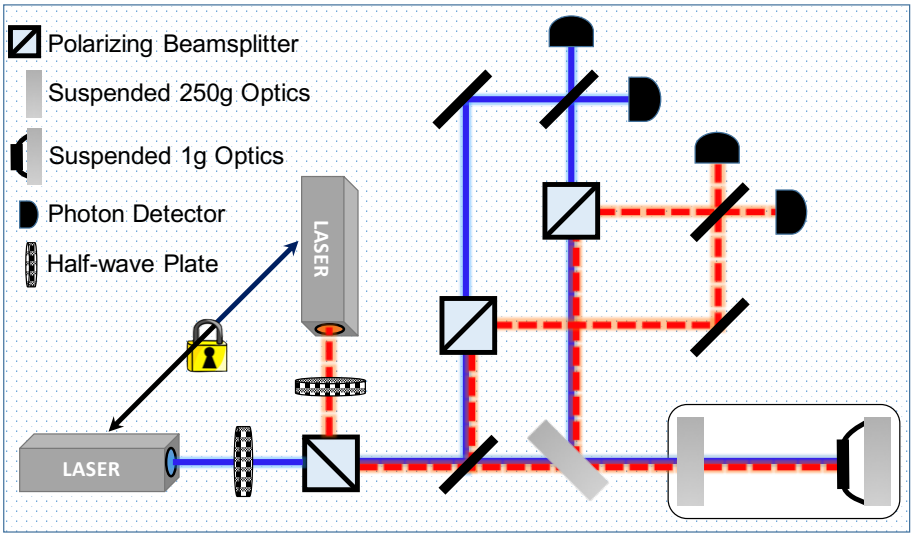

Figure 5.1: Schematic diagram of the proposed experiment. The scheme uses two frequency locked laser fields that are prepared in two orthogonal polarizations before entering the cavity. A balanced homodyne measurement is employed to construct the full quadrature covariance matrix. The scheme utilizes polarizing beam splitters to isolate orthogonal polarizations.

more realistic models for input noises. Other variables pertaining to the optomechanical cavity, such as the thermal noise from the μmirror motion (at room temperature), was taken from experimental data of the same setup [52].

5.1.2 Measuring entanglement

To determine whether or not the output fields are entangled we need to choose a convenient measure. The main measure we will use here is the logarithmic negativity entanglement measure [53, 31]. The variance matrix assembled from the quadrature operators will be the main output to measure.

Logarithmic negativity

The logarithmic negativity is useful for measuring continuous-variable (CV) entanglement and is monotone for Gaussian beams (see appendix for an alternate entanglement measure and results). The information-theoretic meaning of logarithmic negativity in terms of exact entanglement cost of quantum Gaussian states was established in [54, 55]. Conveniently, the logarithmic negativity can be calculated from the variance matrix (see

equation 3.2 [56]:

$$E_N = \max[\ 0,\ \ -\ln\sqrt{2\eta - 2\sqrt{\eta^2 - 4\det\mathbf{V}}}\ ]\ ,$$
$$\text{where}\quad \eta = \det V_{11} + \det V_{22} - 2\det V_{12}.$$

5.1.3 Computational resources

While the quantum Langevin approach is more convenient for an analytical approach, to experimentally and computationally develop a simulation, sideband operator propagation is preferred; due to its more intuitive treatment of the optics and higher modularity [22, 29]. The simulation assumes an input field and cavity configuration specified by some parameter configuration ξ and outputs the homodyne measurement of the quadratures. It solves for the output quadratures via successive transformation of the input sideband quadratures. To calculate the effect of the micromirror on the input sidebands, measurement data from previous work with the optomechanical cavity is used to simulate the cantilever's effects. These data allow our simulation to consider the cantilever's higher harmonic modes' effect on the entanglement.

These programs are written to calculate the entanglement measures over different parameter spaces. There are nine adjustable parameters; highlighted in the table 5.1. Past experiments identified configurations that would yield observable single mode squeezing for a single incident beam. These results narrowed our search for optimal parameters (more on these methods in later in the chapter).

5.2 Results

The last column in table 5.1 represents a parameter set that generates the highest logarithmic negativity and stable optical spring. After the simulations are preformed the output is used to calculate the variance matrices and entanglement measures. All subsequent figures will use the parameters in the table above unless otherwise specified. For example at room temperature and frequency of about 20 kHz, the program predicts an

output variance matrix,$\mathbf{V}$ where $E_N(\mathbf{V}) = 0.104$ and where:

$$\mathbf{V} = \begin{pmatrix} 17.32 & -51.38 & -21.06 & -14.80 \\ -51.38 & 156.2 & 63.76 & 45.07 \\ -21.06 & 63.76 & 26.61 & 18.47 \\ -14.80 & 45.07 & 18.47 & 13.54 \end{pmatrix} \tag{5.1}$$

(note that unsqueezed shot noise would have a variance matrix of $\frac{1}{2}\mathbf{I}$ where $\mathbf{I}$ is the identity matrix).

Table 5.1: Set of variable simulation parameters, and a stable configuration that yield non-zero entanglement.

Stable laboratory parameters $\mathscr{P}_1$

Parameter	Notation	Stable and $E_N \neq 0$
Temperature	T	295K
Circulating carrier power	P_1	0.2816W
Circulating subcarrier power	P_2	0.2238W
Loss	L_s	$250ppm$
Carrier detuning	d_1	0.3
Subcarrier detuning	d_2	-1.5
Quality factor	Q	17000
Cavity Length	L_n	0.01m

Further analyzing the entanglement yields, we found that the E_N was maximum at 20kHz for the above parameters. This maximum appears to decrease slightly in frequency as temperature decreases as shown in figure 5.2. In the figure, the sharp drops to zero E_N are at the resonance frequencies of higher order mechanical modes of the cantilever.

Not only is the double optical spring cavity capable of entangling the two fields, it is able to do so at room temperature. Cooling the micromirror increases both the degree of entanglement and the frequencies over which it is produced. However, there is no significant advantage to cooling the micromirror below 4K, for frequencies of 1kHz and above. This is a result of the thermal noise being pushed well below the quantum back action level, as shown in figure 4. At about 4K, the logarithmic negativity maximizes at approximately $E_N = 0.2$ at frequencies above the yaw resonance at 4.3 kHz. Furthermore, the figure shows

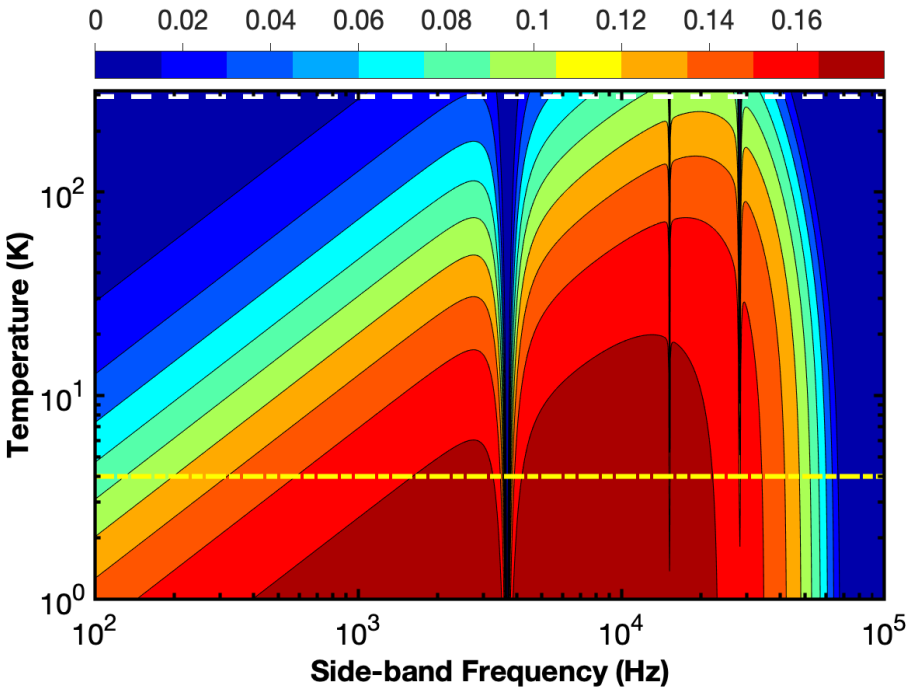

Figure 5.2: Logarithmic negativity measure (E_N) of the two output optical fields as a function of temperature and frequency. Conveniently, these parameters yield entanglement at room temperature for a range of frequencies. The sharp drops in E_N are due to the higher order optical spring resonances of the cantilever micromirror (yaw resonance at 4.3 kHz and translation and yaw 54 kHz are the most visible). Top and bottom most dotted lines indicate 295K and 4K respectively.

that the predicted entanglement closely follows the results of the ponderomotive squeezing experiment, which also maximized at a frequency of about 20 kHz at room temperature [23].

More promise for this method is inspired by the results displayed in figure 5.3. Even when realistic noise and losses are considered the entanglement persists. Lower losses also aid the entangler; figure 5.3 shows the entanglement increases as loss decreases. The behavior of the classical to quantum noise ratio well follows that of the entanglement at all temperatures.

To maximize entanglement we consider changing the optomechanical cavity length. Figure 5.4 shows the dependence between cavity length and E_N. Together figures 5.4 and 5.5 pertain to the fundamental concepts behind optomechanical entanglement generation. The cavity length changes due to the input laser power. This has quantum fluctuations due to the Heisenberg uncertainty principle. This creates a fundamental uncertainty in

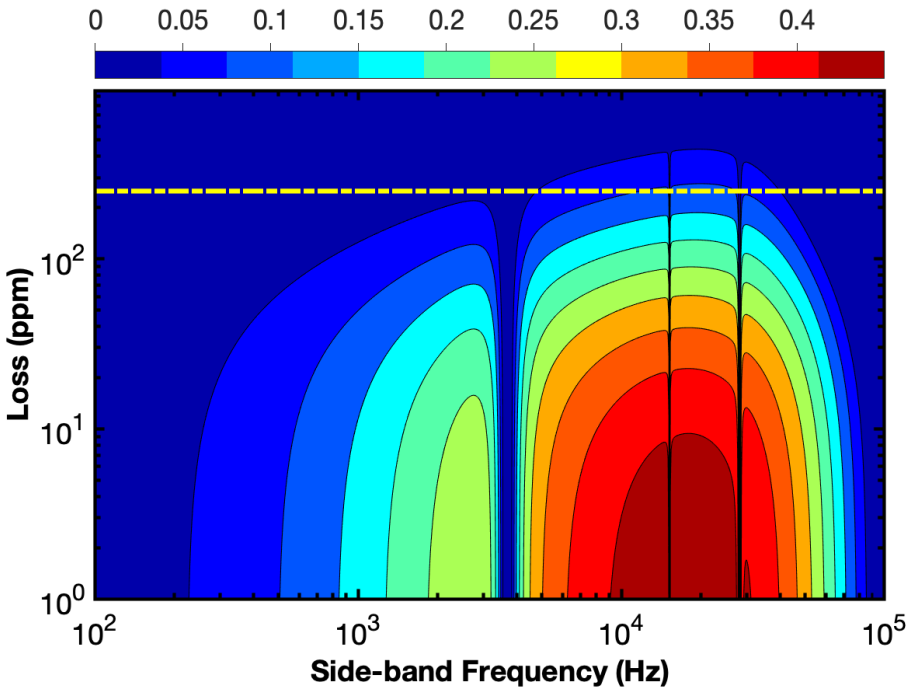

Figure 5.3: E_N vs Loss and frequency at room temperature. Encircled black region denotes absolute zero logarithmic negativity. For small changes in loss the maximum E_N is relatively constant. The three higher order harmonics are all visible here: yaw,ya-transverse, roll-transverse. The yellow line indicates current experimental losses.

the overall cavity length, which in turn strongly effects the properties of the output light. This technique manipulates quantum radiation pressure noise into an entanglement source. When this noise is greater than the classical noise, in this case thermal noise, the entanglement should thrive; figure 5.5 confirms this. Furthermore, entanglement will be limited if the cavity length fluctuations are too small relative to the overall cavity length. Moreover, the dampening effects become more dominant as the cavity length increases thus widening the resonances that destroy entanglement as shown in figure 5.4.

We would like to quantify how difficult it is to experimentally verify the existence of the simulated entanglement. We simulate a noisy variance matrix measurement by creating a set of variance matrices normally distributed about the initial output variance matrix at each frequency. (While we shall only show the experiments noise sensitivity as a function of Gaussian spread and frequency, it is possible to vary any of the parameters in the table for the noise analysis) The resulting entanglement uncertainties are plotted in figure 5.6.

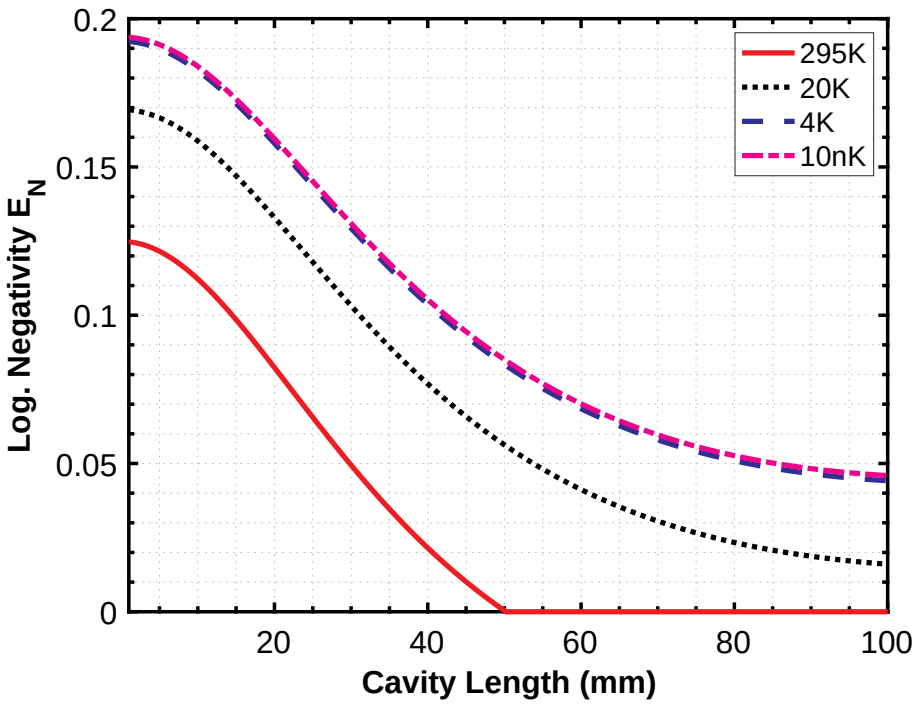

Figure 5.4: Logarithmic negativity versus the cavity length for different ambient temperatures at 20kHz. No benefit to entanglement generation will be seen when cooling below 4K (unless operating at the cantilever's higher harmonic frequencies). Furthermore, cooling below 1K avoids losses to entanglement due to harmonic effects the cavity length effects on the entanglement (the drop at 10cm) are present at all temperatures. Entanglement does not improve at cavity lengths shorter than 1mm.

With measurement certainty on the order of 1% the output noise in the measurement is several times that of the expected maximum entanglement. When measuring at or near the peak E_N frequency, the double homodyne precision must be on the order of 0.1%.

5.3 Simulating the optomechanics

This project's simulations required a mathematical framework (we refer to as the adapted two-photon framework) that developed from the two-photon formalism by Caves and Schumaker. This approach solves for the propagating fields in an interferometer via the input-output equations that pertain to each constituent optic in the interferometer. These methods are described in detail in the reference [22]. Here we give a more abstract overview of the process.

Let $\hat{\mathbf{a}}$ equal a column vector of sideband annihilation operators in the adapted two-

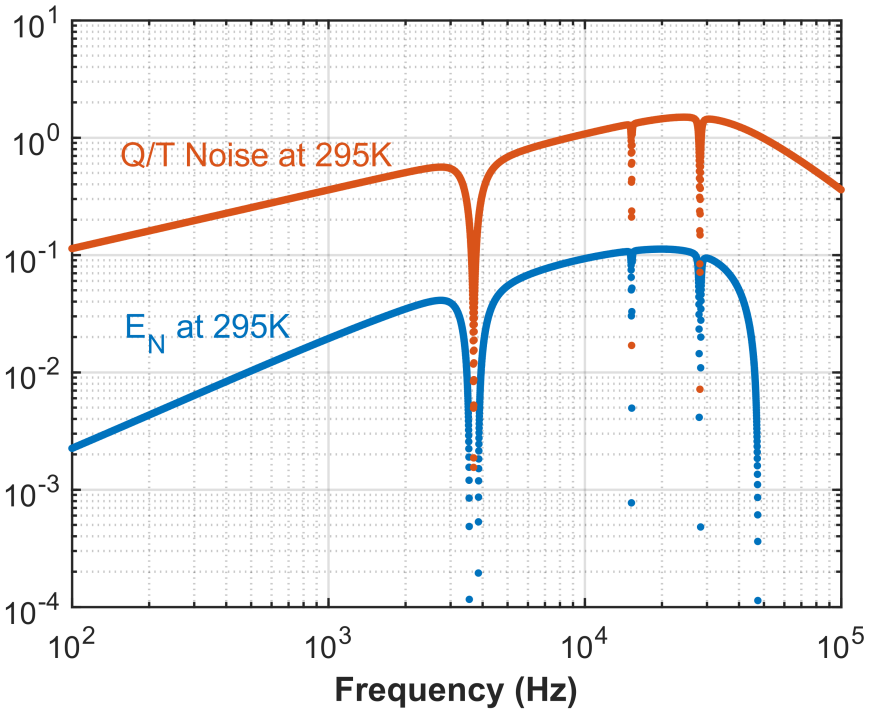

Figure 5.5: The ratio of quantum to thermal noises in the system (see appendix for calculation). The Logarithmic negativity result at room temperature (295K) has been included to show agreement.The early decrease of the E_N with respect to the noise ratio is due to losses. While this confirms our hypothesis about the quantum radiation pressure noise working in opposition to the thermal noises to yield entanglement, in conjunction with our other results it also shows that such an entanglement generation technique heavily relies on the other experimental parameters as well.

photon formalism specific to our considered experimental setup in fig. 5.1 [22]. For our specific experimental setup there is a corresponding matrix $\mathbf{M}$ such that the following is true for each particular parameter configuration ξ:

$$\mathbf{M}\,\hat{\mathbf{a}} = \begin{pmatrix} M(1,1) & & M(1,62) \\ & \cdot\ \ \cdot & \\ & \cdot\ \ \cdot & \\ M(62,1) & & M(62,62) \end{pmatrix} \begin{pmatrix} \hat{\mathbf{a}}_1 \\ \cdot \\ \cdot \\ \hat{\mathbf{a}}_{62} \end{pmatrix} = \hat{\mathbf{u}}\ , \tag{5.2}$$

$$\text{such that } \hat{\mathbf{u}} = \hat{\mathbf{v}}_\mathbf{0} + \hat{\mathbf{l}}_\mathbf{0}\ ; \tag{5.3}$$

where $\hat{\mathbf{v}}_\mathbf{0}$ and $\hat{\mathbf{l}}_\mathbf{0}$ are column vectors corresponding to vacuum and input laser sidebands.

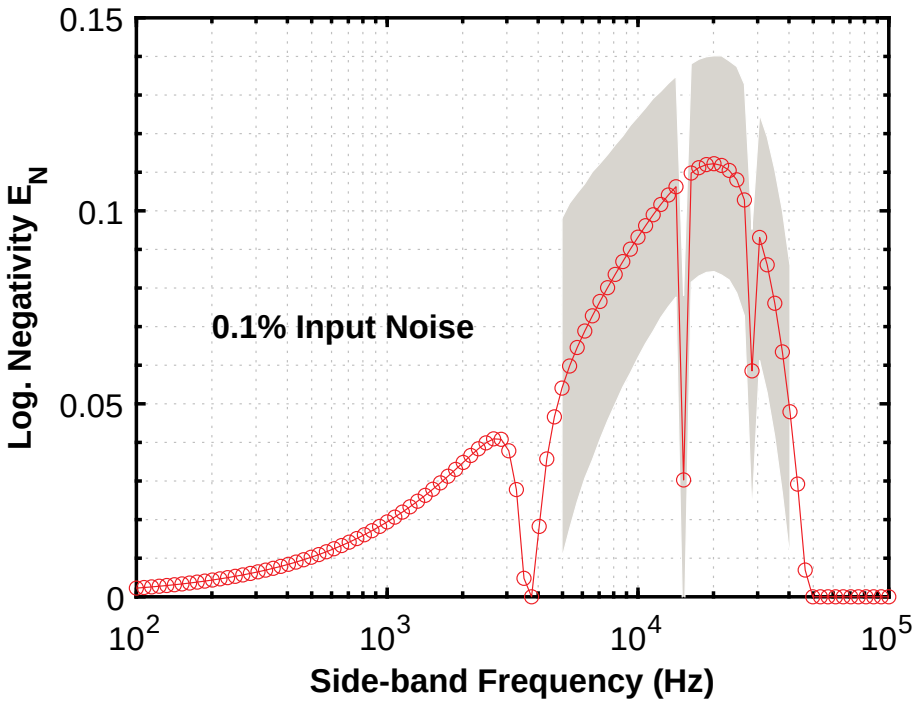

Figure 5.6: The effects of Gaussian noise in the double homodyne measurement in the resulting negativity. This was done by creating a normal distribution of variance matrices and calculating the standard deviation. Due to the numeric instabilities in the entanglement measure, entanglement verification requires high precision measurement of the output quadratures (about 0.1%) (67% confidence interval); the logarithmic negativity is highly sensitive to Gaussian noise. The grey shaded region denotes the uncertainty in the output entanglement. All parameters for this calculation match those in the table previous.

Furthermore, elements of the vector $\hat{\mathbf{a}}$ are the annihilation operators for the sidebands with out vacuum noises and laser input. In figure 5.7, the noiseless sidebands are named the critical sidebands. As is explained in the figure, calculating the fields and the homodyne measurement simulation requires the inversion of a 62×62 matrix. This is one of the differences between the traditional Quantum Langevin approach and the two-photon reformalism approach. The two-photon methods allows for the development of more robust programs. These programs are more intuitive when including losses, noises, and changes to the experimental apparatus in the computations.

5.3.1 Noise ratio calculation

This technique solves for all fields in the optical apparatus, so it is convenient for our calculation for the quantum to thermal noise ratio as well. To begin we assume that the only

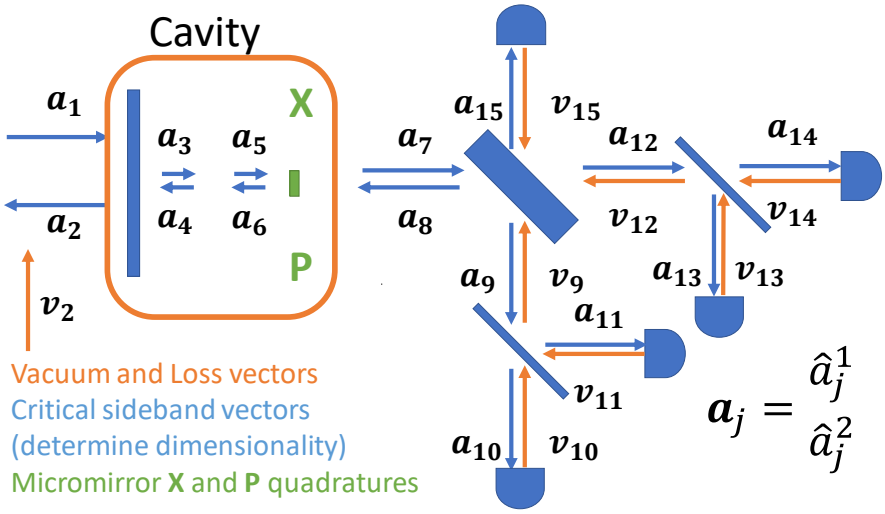

Figure 5.7: The program calculates the transformation matrix for the sideband operators ($\hat{\mathbf{a}}_j$).Since there are 15 fields with each having an upper and lower annihilation operator for a single field input the program calculates (considering losses and input noises) and inverts a 30 +2 by 30 +2 transformation matrix. For the two input fields case the matrix is 60 + 2 by 60 + 2

significant thermal noise source is in the variance of the μmirror's expected position. Next, we sum the total quadrature noise directly from the homodyne detection; then, divide by the thermal noise's contribution to the double homodyne noise detection. Mathematically,

$$Q_N = \frac{total\ input\ quantum\ noise\ measured}{total\ thermal\ noise\ measured}; \tag{5.4}$$

for a single coherent input this can be written in the same terms used in figure 5.7. To begin let there be two vectors $\mathbf{u}$ and $\mathbf{v}$ such that the elements of $\mathbf{u}$ are the matrix elements $M^{-1}(19,1)$, $M^{-1}(19,6)$, and all other elements in between in the same row (in MATLAB $\mathbf{v} = M^{-1}(19, 1:6)$); and where $\mathbf{v}$ are likewise but in between the elements $M^{-1}(X,1)$, $M^{-1}(X,6)$. Then,

$$Q_N = \sqrt{\frac{|\mathbb{L}(\mathbf{u})|^2 + |\mathbb{L}(\mathbf{v})|^2 + |M^{-1}(19,13)|^2 + |M^{-1}(19,14)|^2}{\lambda |M^{-1}(X,X)|^2}}, \tag{5.5}$$

where $\mathbb{L}$ takes the vector and assigns a function to the proper elements that correctly accounts for losses (in other words it multiplies elements that correspond to the fields $\mathbf{a}_2$

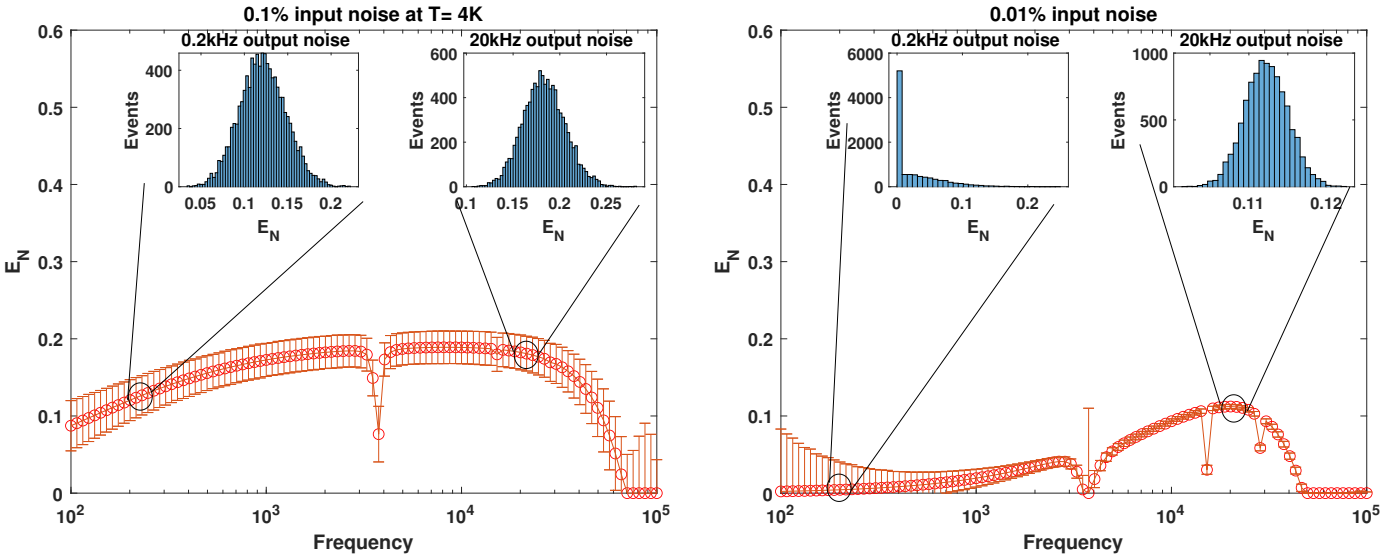

Figure 5.8: All other parameters match the table. Due to the entanglement measure we see non-Gaussian noise output in certain frequency and temperature combinations.

and $\mathbf{a}_3$ by $\frac{l}{1-l}$ where l is the *Loss* parameter in table 5.1). The result of this calculation for each sideband frequency graphed in figure 5.5

5.3.2 Gaussian noise and the logarithmic negativity

Logarithmic negativity cannot be less than zero. So ensembles with high separability have the same E_N as those with lower separability as long as their η_- values are less than zero (see Chapter 3). Figure 5.8 shows how this effects Gaussian noise analysis. Injecting Gaussian noise into our simulated dual homodyne apparatus we often found non-Gaussian statistics in the measurements of E_N.

5.4 Project conclusions

All optical circuits and devices are subject to quantum radiation pressure effects. These effects correlate incident light; which implies potential for new entanglement devices. The effects are strong enough to be manipulated into generating bipartite optical entanglement. Moreover, this entanglement persists at room temperature with realistic losses, stable optical spring detunings, and accessible circulating powers. With experimentally stable parameters, we predict a maximum logarithmic negativity of $E_N = 0.2$; while considering

parameters close to reported experiments yields average logarithmic negativity of $E_N = 0.3$ (with about 1% measurement certainty) which agrees with the results reported there [9]. Furthermore, we found that entanglement is highly temperature dependent. While lowering losses could enhance entanglement, we have shown that the current loss levels still allow for entanglement. Although, predicted entanglement persists despite realistic noise and higher mode considerations, the sensitivity of the system to Gaussian noises presents a significant challenge to experimental realizations. Further optimization may be required to achieve accessible entanglement output.

Chapter 6
Boosting Optomechanical Entanglement with the Injection of Squeezed Light

Upon further application of the adapted two-photon formalism, we extend our knowledge of optomechanical cavities as a quantum optical entanglement device [13]. Previous work computationally demonstrated middling entanglement output when two laser fields are input. Moreover, the computational and experimental squeezing results are further evidence of a lack of "quantumness" in the OMC. We desire a method to enhance these quantum effects. Amplifying the squeezing effects should enhance its quantum effects. It is unlikely that the overall increase in usable quantum output, for even a large increase in the quantum to classical noise ratio, would be marginal; as it was in Chapter 5, where cooling below $T = 4$ the increase in the output E_N was marginal. OMC could be more useful if we could enhance these effects; it would also be convenient if these devices could generate much more entanglement. Investigating all options is necessary to grasp the utility of optomechanical cavities in quantum technologies fully. In a first attempt to amplify these quantum effects, we consider the room temperature simulations' results. The project in Chapter 5 found that the quantum to thermal noise ratio was a good indicator of the OMC's "quantumness". When the ratio was high, entanglement (for dual input) and (for single input field) squeezing were output. Thus, to increase the quantum effects in the OMC, we must first need to somehow increase the quantum noise in the cavity. One possibility is to inject states with higher quantum noise, for example, squeezed states.

6.1 Squeezing

Adding squeezed light in OMC optical circuits has been demonstrated, both theoretically and experimentally, to dissipate the negative OM effects that obscure measurements of phase in interferometers, that impede optical cooling of the mechanical oscillator, etc. [57, 58, 59, 60, 61]. Here, we attempt to use squeezed light to enhance the OM effects. Specifically, we look to increase the output bipartite optical entanglement produced in the OMC. First, we recall from our previous work that two coherent states input into

the cavity may yield bipartite entangled optical quantum states. This entanglement is due to the optomechanical interaction. The quantum fluctuations of the two input beams are imprinted onto each other since both fields interact with a single mechanical mode. The interaction Hamiltonian, with the higher-order terms in the mirror's x quadrature dropped, is recalled from Chapter 4 as the following:

$$H_{int} = -g(\hat{\mathbf{n}}_1 + \hat{\mathbf{n}}_2)\hat{\mathbf{X}}_\mu \ . \tag{6.1}$$

This term also plays a significant role in enhancing the output squeezing when squeezed light is injected into the OMC.

This enhancement of quantum noise is also what enables these devices to produce entangled light from coherent inputs. Furthermore, as the squeezed light injection enhances output squeezing, squeezed inputs also enhance output optomechanical entanglement.

6.1.1 Squeezed coherent input

We predicted enhanced response and increased optomechanical cavity effectiveness when the input states are squeezed coherent light.

Let us assume we have included in out table top system a black box single-mode squeezer. Our input state is then written as follows:

$$|\xi_A, \alpha_A\rangle_1 = \hat{\mathbf{S}}_1(\xi_A)\hat{\mathbf{D}}_1(\alpha_A)\,|0\rangle_1 \ . \tag{6.2}$$

Considering the interaction Hamiltonian above, we can calculate the time propagation of the squeezing in the intracavity quantum state via Heisenberg's quantum equation of motion [62].

In the single-mode simulations, we find that the optomechanical cavity can enhance the single-mode squeezing strength. This effect is seen mathematically from the following commutator (for the common first order approximation in phonon position quadrature

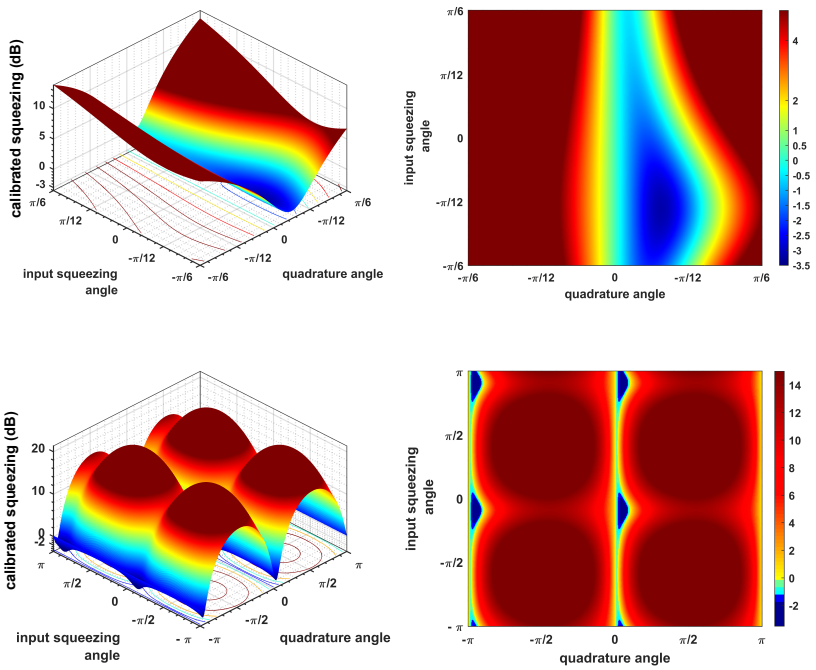

Figure 6.1: Above are the simulation results from the single single-mode coherent state input ($r = 1.1$). Squeezing is present where the output is below 0.

operator $\hat{\mathbf{X}}_\mu$):

$$[\mathbf{H}_{int}, \hat{\mathbf{S}}_j(\xi)] = -g\hat{\mathbf{S}}_j(2\xi)\hat{\mathbf{X}}_\mu \ , \tag{6.3}$$

where $\xi = re^{i\theta}$.

6.2 Enhancing output entanglement

The high quantum to thermal noise ratio is a feature of OM cavities with novel output. A cavity whose intracavity noise is quantum dominate can yield squeezed light or entangled light with one or two coherent states at inputs. Injecting squeezed light into such a device will further increase the quantum to thermal noise ratio. Since the quantum to thermal noise ratio should increase, the squeezed light injection should yield larger output squeezing for the single input field and higher logarithmic negativity for the two field cases.

Our input state

$$|\xi_A, \alpha_A\rangle_1 |\xi_B, \alpha_B\rangle_2 = \mathbf{S}_1(\xi_A)\mathbf{D}_1(\alpha_A)\mathbf{S}_2(\xi_B)\mathbf{D}_2(\alpha_B) |0\rangle_1 |0\rangle_2 \ . \tag{6.4}$$

Considering the interaction Hamiltonian of the form,

$$H_{int} = g(\hat{\mathbf{n}}_1 + \hat{\mathbf{n}}_2)\hat{\mathbf{X}}_\mu \ : \tag{6.5}$$

we calculate the expected intracavity quantum state via Heisenberg's quantum equation of motion.

For $\xi_A = \xi_B = \xi$ the following form is found within:

$$m_1 |2\xi\rangle_1 |\xi\rangle_2 + m_2 |\xi\rangle_1 |2\xi\rangle_2 \tag{6.6}$$

where m_1, and m_2 are functions of temperature, squeezing, and miscellaneous experimental parameters and conditions. More specifically, part of the intracavity field is entangled only due to the non-zero input squeezing parameter, ξ. Mathematically, writing the time derivative of the squeezing operators with respect to the full optomechanical coupling;

$$\begin{aligned} \dot{\hat{\Xi}} &= \dot{\hat{\mathbf{S}}}_1(\xi_A)\hat{\mathbf{S}}_2(\xi_B) + \hat{\mathbf{S}}_1(\xi_A)\dot{\hat{\mathbf{S}}}_2(\xi_B) \ , \\ \dot{\hat{\Xi}} = \ & (\hat{\mathbf{S}}_1(2\xi_A)\hat{\mathbf{S}}_2(\xi_B) + \hat{\mathbf{S}}_1(\xi_A)\hat{\mathbf{S}}_2(2\xi_B) - \hat{\mathbf{S}}_1(\xi_A) - \hat{\mathbf{S}}_2(\xi_B)) \ . \end{aligned} \tag{6.7}$$

6.2.1 Calculating changes in the output entanglement

Since our final output state will host a pure state of the form written in equation 6.7, the squeezing parameters that yield optimal entanglement are calculable. Next, assume a pure state $|\psi\rangle$, such that

$$|\psi\rangle = |\Xi\rangle = m_1 |2\xi_A\rangle_1 |\xi_B\rangle_2 + m_2 |\xi_A\rangle_1 |2\xi_B\rangle_2 \ . \tag{6.8}$$

The above state is a Gaussian state when $\xi_A = \xi_B$; it is a Gaussian state for most combinations of ξ_A and ξ_B; its (positive) Wigner function is written, using the wavefunction from equation 2.22, in the appendix. Then, the density operator becomes the following;

$$\begin{aligned} \hat{\rho} = |\psi\rangle \langle\psi| = \\ |m_1|^2 |2\xi_A\rangle_1 |\xi_B\rangle_2 \langle\xi_B|_2 \langle 2\xi_A|_1 + \\ |m_2|^2 |\xi_A\rangle_1 |2\xi_B\rangle_2 \langle 2\xi_B|_2 \langle\xi_A|_1 + \\ m_1 m_2^* |2\xi_A\rangle_1 |\xi_B\rangle_2 \langle 2\xi_B|_2 \langle\xi_A|_1 + \\ m_1^* m_2 |\xi_A\rangle_1 |2\xi_B\rangle_2 \langle\xi_B|_2 \langle 2\xi_A|_1 \ . \end{aligned} \tag{6.9}$$

Which inspires the following form of the logarithmic negativity:

$$E_N(\rho) = ln||\rho^{\Gamma_B}||_1. \tag{6.10}$$

For a complete basis, we use the photon number basis; so we must recall

$$\begin{aligned} |\alpha, \xi\rangle = (\cosh r)^{-1/2} \ \exp\left[-\frac{1}{2}|\alpha|^2 - \frac{1}{2}\alpha^{*2} e^{i\ \theta} \tanh r\right] \times \\ \sum_{n=0}^{\infty} \frac{(\frac{1}{2} e^{i\ \theta} \tanh r)^{n/2}}{\sqrt{n!}} \ H_n[\gamma (e^{i\ \theta} \sinh 2r)^{-1/2}] \, |n\rangle \ . \end{aligned}$$

The method above is an alternative to finding the quadrature covariance matrix; this may be easier to solve for the entanglement dynamics. First, we note G & K and start solving for the elements in the covariance matrix for a state (see Chapters 2 and 3). Note

that the quadrature covariance matrix is of the traditional form

$$\mathbf{V} = \begin{pmatrix} \langle {X_1}^* X_1 \rangle_+ & \langle {X_1}^* Y_1 \rangle_+ & \langle {X_1}^* X_2 \rangle_+ & \langle {X_1}^* Y_2 \rangle_+ \\ \langle {Y_1}^* X_1 \rangle_+ & \langle {Y_1}^* Y_1 \rangle_+ & \langle {Y_1}^* X_2 \rangle_+ & \langle {Y_1}^* Y_2 \rangle_+ \\ \langle {X_2}^* X_1 \rangle_+ & \langle {X_2}^* Y_1 \rangle_+ & \langle {X_2}^* X_2 \rangle_+ & \langle {X_2}^* Y_2 \rangle_+ \\ \langle {Y_2}^* X_1 \rangle_+ & \langle {Y_2}^* Y_1 \rangle_+ & \langle {Y_2}^* X_2 \rangle_+ & \langle {Y_2}^* Y_2 \rangle_+ \end{pmatrix} \tag{6.11}$$

were $\langle u^* v \rangle_+ = \frac{\langle u^* v + v^* u \rangle}{2}$, or in block form:

$$\mathbf{V} = \begin{pmatrix} V_{11} & V_{12} \\ V_{21} & V_{22} \end{pmatrix}. \tag{6.12}$$

Using what we know already we can attempt to write the variance matrix by using the density operator: $Tr(\hat{\rho}\hat{\mathbf{X}}_j\hat{\mathbf{Y}}_k) = \langle \hat{\mathbf{X}}_j\hat{\mathbf{Y}}_k \rangle$.

For the state above, these quadrature operators transform with respect to a squeezing operator $\hat{\mathbf{S}}$; to transform these operators calculate $\hat{\mathbb{X}}_j = \hat{\mathbf{S}}^\dagger \hat{\mathbf{X}}_j \hat{\mathbf{S}}$. Of the 16 terms in the covariance matrix, the four diagonal terms are (somewhat) trivial, and six others can be calculated directly from the remaining six. Therefore, we only need to calculate six terms to construct the matrix

$$\begin{aligned} \hat{\mathbb{X}}_j \hat{\mathbb{X}}_k &= \cosh r_j \cosh r_k \hat{\mathbf{X}}_j \hat{\mathbf{X}}_k \\ &+ \frac{1}{4} \sinh r_j \sinh r_k \hat{\tilde{\mathbf{f}}}_j(e^{i\theta_j}, 1) \hat{\tilde{\mathbf{f}}}_k(e^{i\theta_k}, 1) \\ &+ \frac{1}{2} \cosh r_j \sinh r_k \hat{\mathbf{X}}_j \hat{\tilde{\mathbf{f}}}_k(e^{i\theta_k}, 1) \\ &+ \frac{1}{2} \sinh r_j \cosh r_k \hat{\tilde{\mathbf{f}}}_j(e^{i\theta_j}, 1) \hat{\mathbf{X}}_k \ ; \end{aligned} \tag{6.13}$$

and

$$\begin{aligned}\hat{\mathbb{X}}_j\hat{\mathbb{Y}}_k &= \cosh r_j \cosh r_k \hat{\mathbf{X}}_j\hat{\mathbf{Y}}_k \\ -\frac{i}{4}\sinh r_j \sinh r_k \hat{\tilde{\mathbf{f}}}_j(e^{i\theta_j},1)\hat{\mathbf{f}}_k(e^{i\theta_k},1) \\ +\frac{i}{2}\cosh r_j \sinh r_k \hat{\mathbf{X}}_j\hat{\mathbf{f}}_k(e^{i\theta_k},1) \\ -\frac{i}{2}\sinh r_j \cosh r_k \hat{\tilde{\mathbf{f}}}_j(e^{i\theta_j},1)\hat{\mathbf{Y}}_k\ ;\end{aligned} \tag{6.14}$$

these are 5 of the 6 required calculations the final one is the following:

$$\begin{aligned}\hat{\mathbb{Y}}_j\hat{\mathbb{Y}}_k &= \sinh r_j \sinh r_k \hat{\mathbf{Y}}_j\hat{\mathbf{Y}}_k \\ -\frac{1}{4}\sinh r_j \sinh r_k \hat{\mathbf{f}}_j(e^{i\theta_j},1)\hat{\mathbf{f}}_k(e^{i\theta_k},1) \\ +\frac{i}{2}\sinh r_j \sinh r_k \hat{\mathbf{Y}}_j\hat{\mathbf{f}}_k(e^{i\theta_k},1) \\ -\frac{i}{2}\sinh r_j \sinh r_k \hat{\mathbf{f}}_j(e^{i\theta_j},1)\hat{\mathbf{Y}}_k\ ,\end{aligned} \tag{6.15}$$

for $j = 1$ and $k = 2$.

Next, we consider these transformed operators acting on a pair of squeezed states with squeezing parameters ξ_1 and ξ_2. After the transformation, the leftover quadratures are the quadrature operators for a vacuum state (should produce the same overall variance matrix as the coherent states). Let us begin by writing V_{11} for the super-ξ state. This is similar to calculating $\mathbf{G}$ for this case in the QL approach (see next section) but with different (or more specific) squeezing parameters. Thus, V_{11} is the following (before symmetrization):

$$\langle\hat{\mathbf{g}}_{11}\rangle = \begin{pmatrix} \frac{1}{2}e^{4r_1^2} + 2\sinh 4r_1\cos\theta_1 & \frac{i}{2} - \sinh 4r_1 \sin\theta_1 \\ \frac{i}{2} - \sinh 4r_1\sin\theta_1 & \frac{1}{2}\sinh^2 2r_1(1 + i\sin\theta_1) \end{pmatrix} \tag{6.16}$$

furthermore,

$$\langle \hat{\mathbf{g}}_{22} \rangle = \begin{pmatrix} \frac{1}{2}e^{r_2^2} + 2\sinh 2r_2 \cos\theta_2 & \frac{i}{2} - \sinh 2r_2 \sin\theta_2 \\ \frac{i}{2} - \sinh 2r_2 \sin\theta_2 & \frac{1}{2}\sinh^2 r_2(1 + i\sin\theta_2) \end{pmatrix}; \tag{6.17}$$

where $\langle \hat{\mathbf{g}}_{12} \rangle = 0$ and $\langle \hat{\mathbf{G}} \rangle = \langle \hat{\mathbf{g}} \rangle + \langle \hat{\eth} \rangle$; additionally,

$$\hat{\mathbf{g}} = \begin{pmatrix} \hat{\mathbf{g}}_{11} & \hat{\mathbf{g}}_{12} \\ \hat{\mathbf{g}}_{21} & \hat{\mathbf{g}}_{22} \end{pmatrix} \qquad \hat{\eth} = \begin{pmatrix} \hat{\eth}_{11} & \hat{\eth}_{12} \\ \hat{\eth}_{21} & \hat{\eth}_{22} \end{pmatrix} \tag{6.18}$$

next,

$$\langle \hat{\eth}_{11} \rangle = \begin{pmatrix} \frac{1}{2}e^{r_1^2} + 2\sinh 2r_1 \cos\theta_1 & \frac{i}{2} - \sinh 2r_1 \sin\theta_1 \\ \frac{i}{2} - \sinh 2r_1 \sin\theta_1 & \frac{1}{2}\sinh^2 r_1(1 + i\sin\theta_1) \end{pmatrix} \tag{6.19}$$

furthermore,

$$\langle \hat{\eth}_{22} \rangle = \begin{pmatrix} \frac{1}{2}e^{4r_2^2} + 2\sinh 4r_2 \cos\theta_2 & \frac{i}{2} - \sinh 4r_2 \sin\theta_2 \\ \frac{i}{2} - \sinh 4r_2 \sin\theta_2 & \frac{1}{2}\sinh^2 2r_2(1 + i\sin\theta_2) \end{pmatrix}. \tag{6.20}$$

The process written above follows $\hat{\mathbb{X}}_j = \hat{\mathbf{S}}^\dagger \hat{\mathbf{X}}_j \hat{\mathbf{S}}$ which, in Heisenberg picture, is essentially rewritten using commutator relations as $\hat{\mathbb{X}}_j => \hat{\mathbf{S}}^\dagger \hat{\mathbf{S}} \hat{\mathbf{O}}_j$; where $\hat{\mathbf{O}}_j$ is some arbitrary operator that is yielded from the commutation of $\hat{\mathbf{X}}_j$ with $\hat{\mathbf{S}}_j$ [44]. However, when trying to measure the entanglement of the super ξ state one must calculate terms such as $\hat{\mathbb{X}}_j \hat{\mathbb{X}}_k$ to write the super-ξ covariance matrix.These terms are equal to $\hat{\mathbf{S}}_m^\dagger \hat{\mathbf{X}}_j \hat{\mathbf{X}}_k \hat{\mathbf{S}}_n$, where m and n indicate the two squeezing parameters, are dependent on two different squeezing parameters when $m \neq n$. Details of this calculation are in appendix. Those calculations show for $\zeta = 2\xi$ that $\hat{\mathbf{S}}^\dagger(\zeta)\hat{\mathbf{S}}(\xi) = \hat{\mathbf{S}}(2\xi)^\dagger$, effectively multiplying affected variance matrices by $\frac{1}{\cosh 2r}$.

Ultimately, we end up with a sum of 4 matrices as our unsymmetrized variance matrix.(

for the $\xi_A = 2\xi_B = 2\xi$ case); $\hat{\mathbb{M}}_{11}\ \hat{\mathbf{1}} + \hat{\mathbb{M}}_{22}\ \hat{\mathbf{1}} + \hat{\mathbb{M}}_{12}\ \frac{1}{\cosh 2r} + \hat{\mathbb{M}}_{21}\ \frac{1}{\cosh 2r}$. The following alternative approach provides more insight into the four terms here.

an alternate approach

The approach above is precarious in notation and handling of the complications due to the squeezing amplifications. Below is a more formal yet hopefully equivalent methodology. The goal in this section is to calculate the terms in the quadrature variance matrix. To begin, let $\hat{\mathscr{O}}_j(\theta_1)$ represent some arbitrary quadrature operator of the j^{th} mode with quadrature angle θ_1; then, any arbitrary covariance matrix element is the following:

$$\tilde{\mathbf{V}}_{jk} = \hat{\mathbf{S}}_1^\dagger(s_1^1\xi_1)\hat{\mathbf{S}}_2^\dagger(s_2^1\xi_2)\hat{\mathscr{O}}_j(\theta_j)\hat{\mathscr{O}}_k(\theta_k)\hat{\mathbf{S}}_1(s_1^2\xi_1)\hat{\mathbf{S}}_2(s_2^2\xi_2)\ , \tag{6.21}$$

where $\tilde{\mathbf{V}}_{jk}^{(i)}$ is an element of one of the unsymmetrized variance matrix that sum to the unsymmetrized variance matrix $\mathbf{V}$ ($\mathbf{V} = \sum_{i=1}^{4}\mathbf{V}^{(i)}$) before taking the expectation values; the superscript i is ignored for now. Due to the lack of commutators between different modes, this element can be written as

$$\tilde{\mathbf{V}}_{jk} = \prod_\ell \hat{\mathbf{S}}_\ell^\dagger(s_1^\ell\xi_\ell)\hat{\mathscr{O}}_\ell(\theta_\ell)\hat{\mathbf{S}}_\ell(s_2^\ell\xi_\ell)\ . \tag{6.22}$$

Next, depending on θ_ℓ the quadrature operator $\hat{\mathscr{O}}$ can be either $\hat{\mathbf{X}}$ or $\hat{\mathbf{Y}}$, so to solve our covariance matrix we need to calculate $\hat{\mathbf{S}}_\ell^\dagger(s_1^\ell\xi_\ell)\hat{\mathbf{X}}_\ell\hat{\mathbf{S}}_\ell(s_2^\ell\xi_\ell)$ and $\hat{\mathbf{S}}_\ell^\dagger(s_1^\ell\xi_\ell)\hat{\mathbf{Y}}_\ell\hat{\mathbf{S}}_\ell(s_2^\ell\xi_\ell)$.

$$\hat{\mathbf{S}}_\ell^\dagger(s_1^\ell\xi_\ell)\hat{\mathbf{S}}_\ell(s_2^\ell\xi_\ell)\hat{\mathbf{S}}_\ell^\dagger(s_2^\ell\xi_\ell)\hat{\mathbf{X}}_\ell\hat{\mathbf{S}}_\ell(s_2^\ell\xi_\ell)\ =\ \hat{\mathbf{S}}_\ell^\dagger(s_1^\ell\xi_\ell)\hat{\mathbf{S}}_\ell(s_2^\ell\xi_\ell)\hat{\gamma}_x(s_2^\ell\xi_\ell)\ , \tag{6.23}$$

where $\hat{\gamma}_x(s_2^\ell\xi_\ell) = \frac{1}{2}[(\cosh s_2^\ell r_\ell - e^{i\theta_\ell}\sinh s_2^\ell r_\ell)\hat{\mathbf{a}}^\dagger + (\cosh s_2^\ell r_\ell - e^{-i\theta_\ell}\sinh s_2^\ell r_\ell)\hat{\mathbf{a}}]$. In this work the terms s_ℓ^m are ether 1 or 2. Following the calculation in Appendix A.1 , eqn 6.23 becomes

$$\hat{\mathbf{S}}_\ell^\dagger((s_1^\ell - s_2^\ell)\xi_\ell)\hat{\gamma}_x(s_2^\ell\xi_\ell) \tag{6.24}$$

(when we restrict s_ℓ^m to 1 or 2); likewise for $\hat{\mathbf{S}}_\ell^\dagger(s_1^\ell\xi_\ell)\hat{\mathbf{Y}}_\ell\hat{\mathbf{S}}_\ell(s_2^\ell\xi_\ell)$ we have

$$\hat{\mathbf{S}}_\ell^\dagger(s_1^\ell\xi_\ell)\hat{\mathbf{Y}}_\ell\hat{\mathbf{S}}_\ell(s_2^\ell\xi_\ell) = \hat{\mathbf{S}}_\ell^\dagger((s_1^\ell - s_2^\ell)\xi_\ell)\hat{\gamma}_y(s_2^\ell\xi_\ell) \tag{6.25}$$

and $\hat{\gamma}_y(s_2^\ell\xi_\ell) = \frac{i}{2}[(\cosh s_2^\ell r_\ell + e^{i\theta_\ell}\sinh s_2^\ell r_\ell)\hat{\mathbf{a}}^\dagger - (\cosh s_2^\ell r_\ell + e^{-i\theta_\ell}\sinh s_2^\ell r_\ell)\hat{\mathbf{a}}]$. A more general form would be $\hat{\mathbf{S}}_\ell^\dagger(\xi_{1\ell})\hat{\mathbf{Y}}_\ell\hat{\mathbf{S}}_\ell(\xi_{2\ell}) = \hat{\mathbf{S}}_\ell^\dagger(\xi_{1\ell} - \xi_{2\ell})\hat{\gamma}_y(s_2^\ell\xi_\ell)$. Ether way the difference between the two squeezing parameters ,$\xi_{1\ell} - \xi_{2\ell}$, should be known to expedite the calculation in the appendix Appendix A.1.

6.2.2 Squeezed input with the QL method

The Quantum Langevin method allows for the same setup as the initial unsqueezed OM entanglement cases. All that changes are the input noises. Since the coupling matrix does not change for lossless squeezing, we only need to consider alterations to the input noise spectra $\langle\mathbf{G}\rangle$. For this calculation, we lean heavily on the results of the transformed quadrature operators above. Mathematically, each element of the noise matrix is a term of similar form to $\langle\hat{\mathbb{X}}_j\hat{\mathbb{Y}}_k\rangle_{\alpha_1\alpha_2}$; so we write them here

$$\begin{aligned}\langle\hat{\mathbb{X}}_j\hat{\mathbb{Y}}_k\rangle_{\alpha_j\alpha_k} &= \langle\cosh r_j\cosh r_k\hat{\mathbf{X}}_j\hat{\mathbf{X}}_k \\ &+ \frac{1}{4}\sinh r_j\sinh r_k\hat{\tilde{\mathbf{f}}}_j(e^{i\theta_j},1)\hat{\tilde{\mathbf{f}}}_k(e^{i\theta_k},1) \\ &+ \frac{1}{2}\cosh r_j\sinh r_k\hat{\mathbf{X}}_j\hat{\tilde{\mathbf{f}}}_k(e^{i\theta_k},1) \\ &+ \frac{1}{2}\sinh r_j\cosh r_k\hat{\tilde{\mathbf{f}}}_j(e^{i\theta_j},1)\hat{\mathbf{X}}_k\rangle_{\alpha_j\alpha_k}\end{aligned} \tag{6.26}$$

assuming we can average with respect to $0_1 0_2$ instead of $\alpha_1\alpha_2$ we note: $\hat{\mathbf{X}}\,|0\rangle = 1/2\,|1\rangle$, $\hat{\tilde{\mathbf{f}}}(u,1)\,|0\rangle = u\,|1\rangle = \hat{\mathbf{f}}(u,1)\,|0\rangle$.

For single-mode correlations, the intra-mode quadratures are non-zero, yet the inter-

modes are zero; thus,

$$\langle\hat{\mathbb{X}}_j\hat{\mathbb{X}}_k\rangle_{00} = \langle\delta_{jk}(\cosh r_j\cosh r_k\hat{\mathbf{X}}_j\hat{\mathbf{X}}_k \;+\; \frac{1}{4}\sinh r_j\sinh r_k\hat{\tilde{\mathbf{f}}}_j(e^{i\theta_j},1)\hat{\tilde{\mathbf{f}}}_k(e^{i\theta_k},1) \tag{6.27}$$

$$+\;\frac{1}{2}\cosh r_j\sinh r_k\hat{\mathbf{X}}_j\hat{\tilde{\mathbf{f}}}_k(e^{i\theta_k},1) \;+\; \frac{1}{2}\sinh r_j\cosh r_k\hat{\tilde{\mathbf{f}}}_j(e^{i\theta_j},1)\hat{\mathbf{X}}_k)\rangle_{00}$$

$$= \;\langle(\cosh^2 r_j\hat{\mathbf{X}}_j^2\rangle_{00} \;+\; \langle\frac{1}{4}\sinh^2 r_j\hat{\tilde{\mathbf{f}}}_j^\dagger(e^{i\theta_j},1)\hat{\tilde{\mathbf{f}}}_k(e^{i\theta_k},1)\rangle_{00} \tag{6.28}$$

$$+\;\langle\frac{1}{2}\cosh r_j\sinh r_j\hat{\mathbf{X}}_j\hat{\tilde{\mathbf{f}}}_j(e^{i\theta_j},1)\rangle_{00} \;+\; \langle\frac{1}{2}\sinh r_j\cosh r_j\hat{\tilde{\mathbf{f}}}_j(e^{i\theta_j},1)\hat{\mathbf{X}}_j)\rangle_{00}$$

$$= \;1/4\cosh^2 r_j \;+\; \frac{1}{4}\sinh^2 r_j \;+\; \frac{1}{2}\cosh r_j\sinh r_j e^{i\theta_j} \;+\; \frac{1}{2}\sinh r_j\cosh r_j e^{-i\theta_j} \tag{6.29}$$

$$= \;\frac{1}{4}(\cosh^2 r_j \;+\; \sinh^2 r_j) \;+\; \sinh 2r_j(\cos\theta_j) \tag{6.30}$$

$$= \;\frac{1}{4}e^{r^2} \;+\; \sinh 2r_j(\cos\theta_j)\;. \tag{6.31}$$

Next,

$$\langle\hat{\mathbb{X}}_j\hat{\mathbb{Y}}_k\rangle_{00} = \langle\cosh r_j\cosh r_k\hat{\mathbf{X}}_j\hat{\mathbf{Y}}_k \;-\; \frac{i}{4}\sinh r_j\sinh r_k\hat{\tilde{\mathbf{f}}}_j(e^{i\theta_j},1)\hat{\mathbf{f}}_k(e^{i\theta_k},1) \tag{6.32}$$

$$+\;\frac{i}{2}\cosh r_j\sinh r_k\hat{\mathbf{X}}_j\hat{\mathbf{f}}_k(e^{i\theta_k},1) \;-\; \frac{i}{2}\sinh r_j\cosh r_k\hat{\tilde{\mathbf{f}}}_j(e^{i\theta_j},1)\hat{\mathbf{Y}}_k\rangle_{00}$$

$$= \;\cosh^2 r_j i/4 \;-\; \frac{i}{4}\sinh^2 r_j \;+\; \frac{i}{4}\cosh r_j\sinh r_j e^{i\theta_j} \;-\; \frac{i}{4}\sinh r_j\cosh r_j e^{-i\theta_j} \tag{6.33}$$

$$= \;\frac{i}{4} \;-\; \frac{1}{2}\sinh 2r_j\sin\theta_j\;; \tag{6.34}$$

and lastly,

$$\langle\hat{\mathbb{Y}}_j\hat{\mathbb{Y}}_k\rangle_{00} = \langle\sinh r_j\sinh r_j\hat{\mathbf{Y}}_j\hat{\mathbf{Y}}_j \;-\; \frac{1}{4}\sinh r_j\sinh r_j\hat{\mathbf{f}}_j(e^{i\theta_j},1)\hat{\mathbf{f}}_j(e^{i\theta_j},1) \tag{6.35}$$

$$+\;\frac{i}{2}\sinh r_j\sinh r_j\hat{\mathbf{Y}}_j\hat{\mathbf{f}}_j(e^{i\theta_j},1) \;-\; \frac{i}{2}\sinh r_j\sinh r_j\hat{\mathbf{f}}_j(e^{i\theta_j},1)\hat{\mathbf{Y}}_j\rangle_{00}$$

$$= \;\sinh r_j\sinh r_j 1/4 \;-\; \frac{1}{4}\sinh r_j\sinh r_j(-1) \tag{6.36}$$

$$+\;\frac{i}{2}\sinh r_j\sinh r_j(-\frac{i}{2}e^{i\theta_j}) \;-\; \frac{i}{2}\sinh r_j\sinh r_j(-\frac{i}{2}e^{-i\theta_j})$$

$$= \;\frac{1}{2}\sinh^2 r_j + (\frac{1}{4})(\sinh^2 r_j)(2i\sin\theta_j) \tag{6.37}$$

$$= \;\frac{1}{2}\sinh^2 r_j(1 + i\sin\theta_j) \tag{6.38}$$

The first optical sub-matrix for the correlation spectra for squeezed coherent state input is the following:

$$\langle \hat{\mathbf{G}} \rangle = \begin{pmatrix} \frac{1}{2}e^{r_1^2} + 2\sinh 2r_1 \cos\theta_1 & \frac{i}{2} - \sinh 2r_1 \sin\theta_1 \\ \frac{i}{2} - \sinh 2r_1 \sin\theta_1 & \frac{1}{2}\sinh^2 r_j(1 + i\sin\theta_j) \end{pmatrix} \tag{6.39}$$

Since the coupling matrix does not change when adding the lossless squeezing, we only need to consider alterations to the input noise spectra $\langle \mathbf{G} \rangle$. The optical only elements for the correlation spectra for squeezed coherent state input are the following

$$\langle \mathbf{G} \rangle = \tag{6.40}$$

$$\begin{pmatrix} \frac{A_1^2\alpha + B_1^2\alpha^{*2} + A_1B_1(2|\alpha|^2+1)}{2} & \frac{i(B_1^2\alpha^{*2} - A_1^2\alpha^2 + A_1B_1) - 1}{2} & 0 & 0 \\ -\frac{i(B_1^2\alpha^{*2} - A_1^2\alpha^2 + A_1B_1) - 1}{2} & \frac{-A_1^2\alpha - B_1^2\alpha^{*2} + A_1B_1(2|\alpha|^2+1) - 1}{2} & 0 & 0 \\ 0 & 0 & \frac{A_2^2\alpha + B_2^2\alpha^{*2} + A_2B_2(2|\alpha|^2+1)}{2} & \frac{i(B_2^2\alpha^{*2} - A_2^2\alpha^2 + A_2B_2) - 1}{2} \\ 0 & 0 & -\frac{i(B_2^2\alpha^{*2} - A_2^2\alpha^2 + A_2B_2) - 1}{2} & \frac{-A_2^2\alpha - B_2^2\alpha^{*2} + A_2B_2(2|\alpha|^2+1)}{2} \end{pmatrix}$$

where $A_j = \cosh r_j - e^{-i\theta_j}\sinh r_j$ and $B_j = \cosh r_j - e^{i\theta_j}\sinh r_j$.

The simulations correspond to the theoretical calculations. The figure (6.3) shows that the super-ξ state creates entanglement that is periodic in the squeezing angles (with the two angles sharing the same periodicity in E_N). Since the simulation results more so consider the realistic output from an experimental apparatus, the results plotted in figure 6.2 more so correspond to the expected behavior of the output entanglement.

6.2.3 Single 2-mode squeezed input

We expect that the cavity would have a similar effect on two-mode squeezed displaced states. Figure 6.4 confirms this hypothesis. The cavity, with a particular combination of input squeezing parameters, outputs completely disentangled light. It appears to act as a

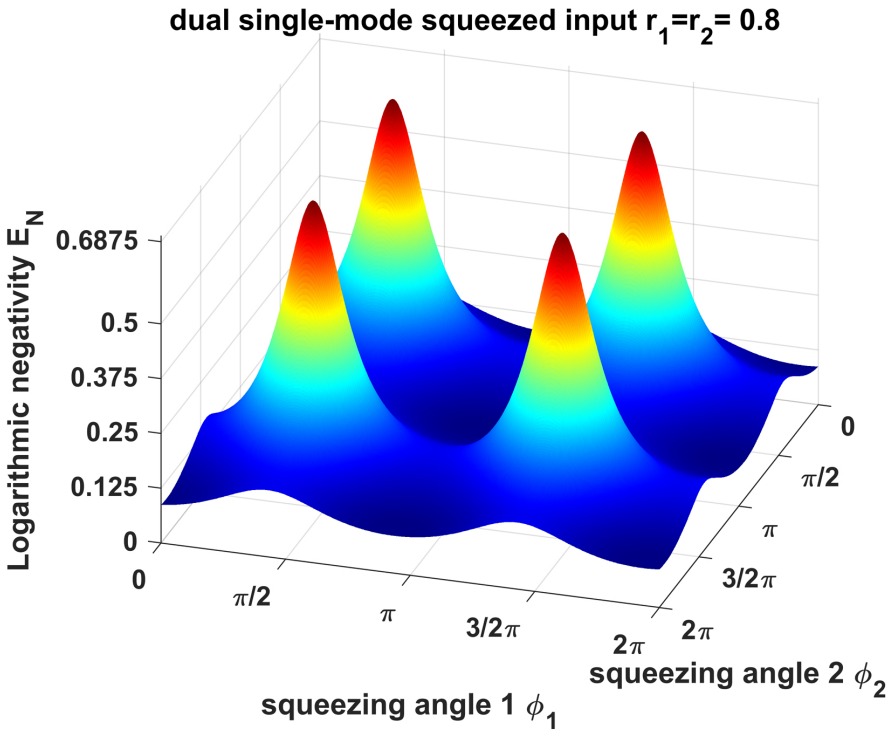

Figure 6.2: The simulation shows the same two-mode periodicity due to the dependence on two squeezing angles. This dependence is consistent with our presented theoretical results of the super-ξ state. The maximum output E_N is about unity and is the same for 2 one-mode squeezed and 1 two-mode squeezed input cases. For this simulation the squeezing strengths are $r_1 = r_2 = 0.8$, and the temperature is set to $4K$, see table 6.1 for other parameters used. The maxima occur when input squeezing angles are odd integer multiples of $\pi/2$ and minima at even integer multiples of $\pi/2$.Interestingly, the maximum E_N for $r_1 = r_2 = 0.5$ is $E_N \approx 6.5$, only slightly lower than the $r_1 = r_2 = 0.8$ case

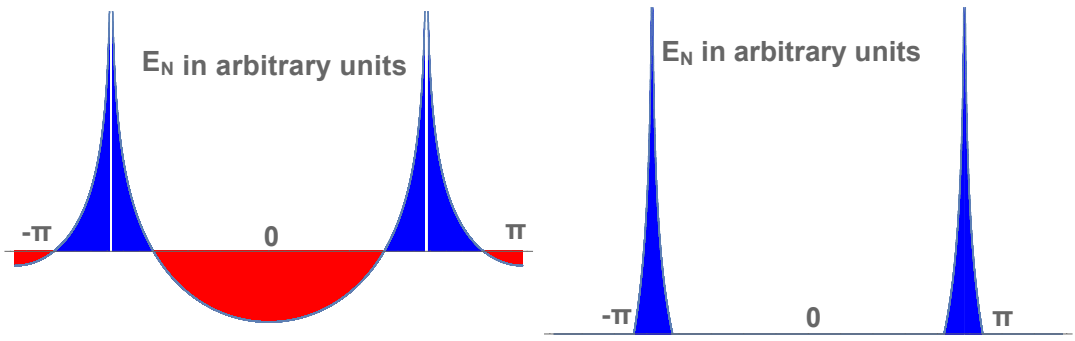

Figure 6.3: Above is a qualitative plot of logarithmic negativity of a super-ξ state as a function of the common squeezing angle, $\theta_1 = \theta_2$ on the left and the logarithmic negativity of the state calculated from the quantum Langevin equations. This result shows that these states boost the entanglement in the same regions as those in the computational results. The double-angle dependence has been removed to better compare to the simulation results. The discrepancies in the theoretical calculations and the simulations are likely from the entanglement measure. The logarithmic negativity is not necessarily monotonic for non-Gaussian continuous variable states, and the super-ξ state is non-Gaussian for some cases where the input squeezing angles are not equal(see Appendix-A.5). The entanglement boosts in the figure affirms the production of the super-ξ states within the optomechanical cavity. Despite a drastic difference in parameters, the maxima in E_N boosting are still at the same relative input squeezing angle and periodicity (integer multiples of π).

detangler for displaced two-mode squeezed states. The entanglement enhancement effects are also limited to about $E_N = 1$.

6.3 OMC device efficacy

Optomechanical cavity-based entanglement generating devices with unsqueezed coherent state input yields output entanglement. However, it is not efficient enough to rival two-mode squeezed vacuum entanglement generation methods. The next step is considering light that has some squeezing before inputting into the OMC. The sections above show much higher output entanglement, yet these yields are not competitive for strong squeezing. The disparaging entanglement yields are clear from comparing figure 6.7 to figure 3.2. However, in the squeezing strength range of $r = 0$ to $r = 0.2$, there is some advantage in the OMC methods over the traditional methods of optical entanglement generation (see figure 6.7). The OMC method always outputs at least some entanglement, unlike the two-mode squeezing methods, which see an output E_N of zero for $r > 0.4$.

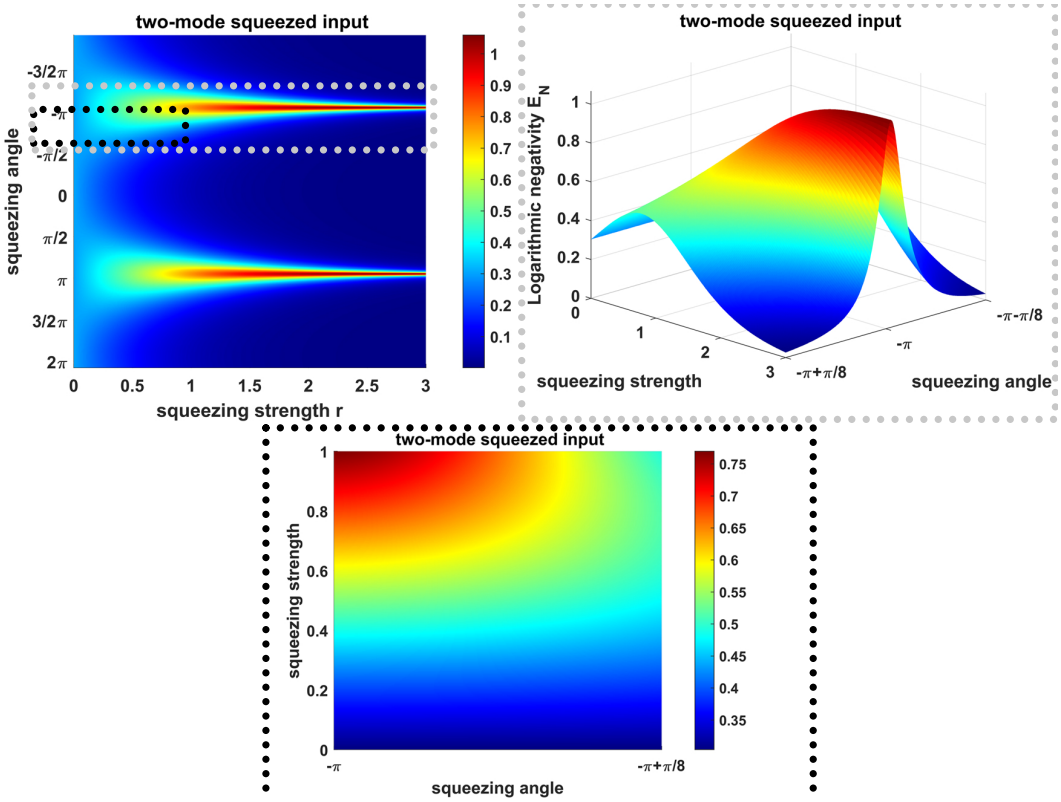

Figure 6.4: Above are the results of the two-mode squeezed coherent input. Each plot is of the same results over different input squeezing parameters. The output E_N is strongly dependent on the input squeezing angle. Output entanglement peaks ($E_N = 1$) at integer multiples of π with a squeezing strength of about 2. Temperature is set to 4K, and the rest of the parameters follow table 6.1. The color scale is rest for the plot encircled in black. The grey boxed plot shows that the peak in output E_N is asymptotic in input squeezing strength r.

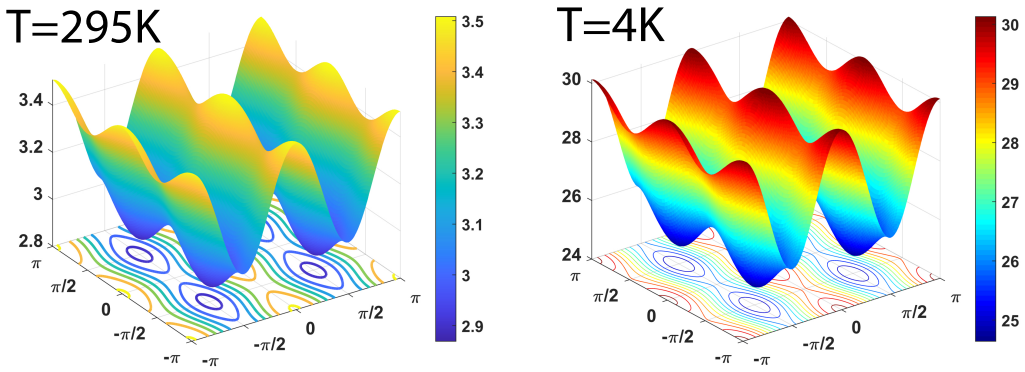

Figure 6.5: Above plots correspond to the dual single-mode squeezed input case with $r_1 = r_2 = 0.8$. In the previous chapter, the quantum to thermal noise ratio greatly determined the cavity's entanglement output. Here this still holds, but the overall increase in entanglement is much less than when unsqueezed coherent light is input (see figure 5.5). In the two plots, the quantum to thermal noise ratio is maximum at the squeeze angles where output entanglement is maximum (at about $(n\pi/2, n\pi/2)$ where n an arbitrary integer); seemingly, in direct contradiction to the results from our last project. However, note the boosted quantum noise in the injected field. Then, the quantum to thermal noise ratio is always above unity. Thus the output bipartite entanglement could occur at any squeezing angle. What this plot likely hints at is the tripartite optomechanical entanglement (between the two propagation optical modes and the mechanical oscillator) at the maximum ratio squeezing angles combination.

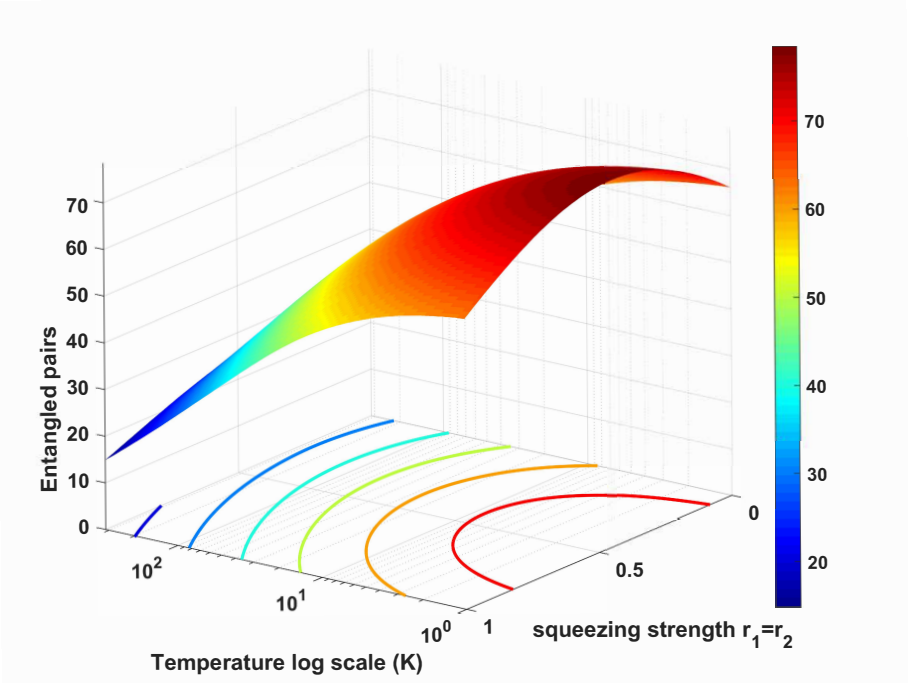

Figure 6.6: This is a plot of the entangled pairs per mode versus the input squeezing strength and temperature for two single-mode squeezed inputs. The squeezing angles are set to yield a maximum E_N (see appendix for two single-mode squeezed squeezing angles plot for lab parameter space), and the other parameters are represented in table 5.1. A notable feature is the maximum entanglement here is at T=1K (which is trivial) and when $r \approx 0.5$. These results hint that OMC may have even more possible applications versus conventional methods at low input squeezing strength.

However, while these advantages will vary with system parameters, the overall benefit to entanglement is slight. This benefit to entanglement is seemingly in contrast to the large increase in the quantum noise (see figure 6.5). The expectation is that the quantum noise drives (or is an indicator of) the optomechanical entanglement. Figure 6.5 shows large quantum variances that are at most two orders of magnitude higher than the unsqueezed input variances (figure 5.5), yet the output entanglement is only weakly boosted.

Entanglement production efficiency output by these devices is low. Even with cryogenics, squeezed light input, and ultra-low losses (here, this means losses two order of magnitude below current laboratory operations), the maximum output E_N is about unity. There should be some applications that can take advantage of this specific system's broadband capabilities (table 5.1) . In the paper by Deng et al., the number of entangled pairs

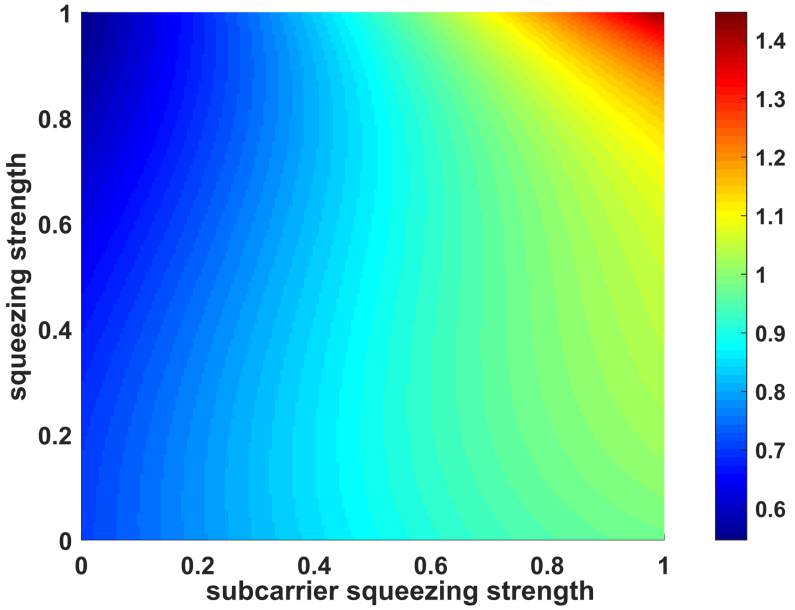

Figure 6.7: In this figure, entanglement at peak squeezing angles odd integer multiples of $\pi/2$ and $\pi/2$ versus squeezing strength. This calculation is done using the LSU parameter set, except temperature is set to 4 K (see table 5.1). These results can be compared to figure 3.2 to see efficacy arguments at small squeezing where the methods described for figure 3.2 yield $E_N = 0$.

per second that these systems overall output per second is E_{NT} where [63],

$$E_{NT} = \frac{1}{2\pi} \int_0^\infty E_N(\Omega) d\Omega \ . \tag{6.41}$$

We can consider all output sideband frequencies for some applications when comparing the entanglement output (see appendix for frequency-dependent plots with squeezed light injection into the OMC). Another factor that directly affects the output entanglement is the mechanical oscillator temperature. This variable is difficult (and expensive) to control and is not an issue with non-optomechanical entanglement methods. With this in mind consider figure 6.6. Which plots the integral's result versus input squeezing strength and mechanical oscillator temperature. Surprisingly, the actual output bipartite optical entanglement rate peaks at $r_1 = r_2 = 0.5$.

The squeezing enhancement results show slight promise for future utility. In section

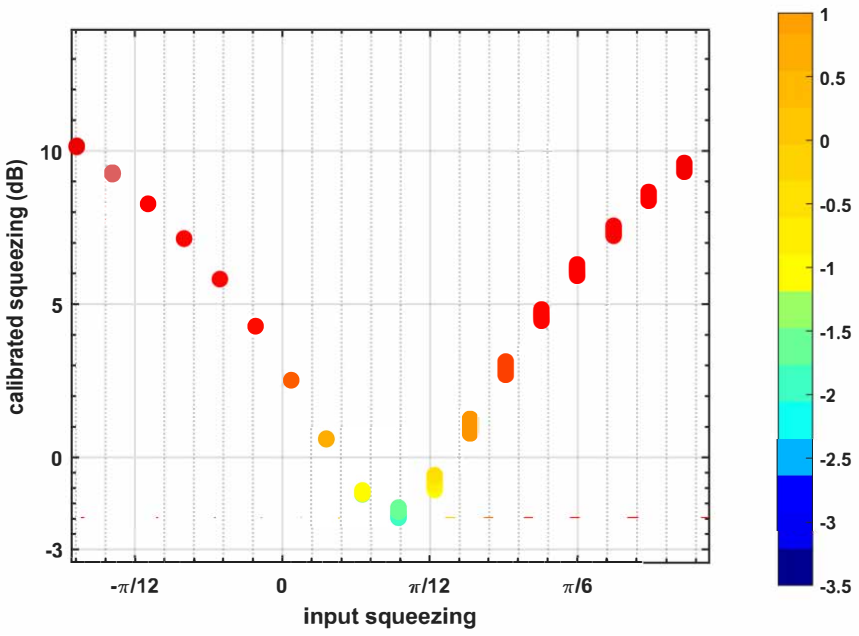

Figure 6.8: Another look at the squeezing results from the single-mode input simulations (similar to figure 6.1). Here input squeezing strength is $r = 0.5$. The overall squeezing is much greater for squeezed input than for an unsqueezed coherent state. This would be an interesting mode of application for these devices if the output squeezing limitations can be overcome. For increasing input squeezing strength, preliminary results show that the marginal output is squeezing decreases.

6.1.1, it appears OMC-based device could be designed to output squeezing on the order of $2^N r$ where N is the number of OM cavities (in series) (see equation 6.3) and r is the input squeezing strength. This application is most likely limited to small input squeezing only $r < 0.4$. Our current results show limited output squeezing for increasing input squeezing strength. More study is necessary to determine feasibility even for the small squeezing applications.

OMC devices could have useful applications in entanglement swapping [24]. The most exciting platform for examining the entanglement swapping applications is that of non-Gaussian inputs here; we can more easily study Gaussian inputs, so we include entanglement output results from two two-mode squeezed coherent inputs though these results are preliminary, they are included in the subsequent chapter.

Future application investigations should include quantum network/internet-related ap-

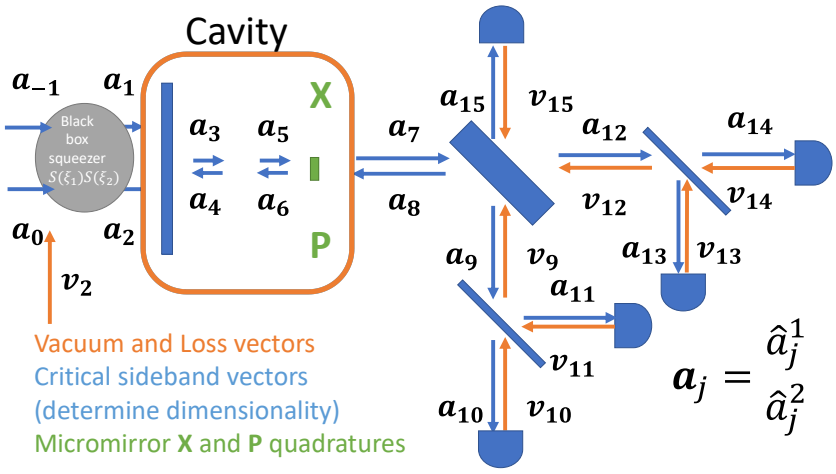

Figure 6.9: This diagram depicts the main calculation in the simulation. The functionality is the same as figure 5.7 but with a lossless black box squeezer that adds two additional fields to the calculation. This diagram best describes the two single-mode squeezed coherent state input scenario, yet the two-mode squeezing case is the same but without the field $\mathbf{a}_{-1}$ and only one squeezing parameter ξ.

plications (like entanglement swapping), non-Gaussian input applications, and quantum noise-based metrology devices.

6.4 Computational methods

Most of the computational framework from our previous project was preserved for this work. Ultimately, the edits where just the addition of the matrix $\mathscr{S}$ and the addition of 1-2 quadrature fields (in figure 6.9 these fields are $\mathbf{a}_0$ and $\mathbf{a}_{-1}$). Here the matrix $\mathscr{S}$ describes how the sideband operators transform due to single-mode squeezing

$$\mathscr{S}(r,\theta) = \begin{pmatrix} \cos 2\theta \sinh r + \cosh r & \sin 2\theta \sinh r \\ \sin 2\theta \sinh r & \cosh r - \cos 2\theta \sinh(r) \end{pmatrix}. \tag{6.42}$$

Changing the parameter space has a strong effect on the results. For our two-photon formalism-based calculations, two-parameter spaces were considered. The first we shall call $\mathscr{P}_1$ is a parameter space loosely based on the laboratory parameter listed in a recent

experimental work where observed OM entanglement from an oscillating silicon membrane-based OMC (see table 6.1) [9]. These parameters gave very stable calculations and led to quick, sensible results. The other parameter space we consider is stable in the optics laboratory at LSU, and that is the same parameter space as listed in the previous chapter (see table 5.1). This space more accurately depicts experimental results, yet they do not stray far from the results from the $\mathscr{P}_1$ parameter space. Simulating with this parameter space presented significant challenges due to numerical instabilities and the non-Gaussian nature of the entanglement measure E_N (see figure 5.8).

Table 6.1: This table is a set of variable simulation parameters and a stable configuration that yield non-zero entanglement. Since losses were not quantified directly in the reference, the Loss value was set equal to our other parameter space yet relative to the new cavity parameters(reflection and transmission).

Ultra-stable parameter set $\mathscr{P}$

Parameter	Notation	Stable and $E_N \neq 0$
Temperature	T	4K
Input carrier power	P_1	0.01W
Input subcarrier power	P_2	0.01W
Loss	L_s	10^{-10}
Carrier detuning	d_1	-0.22
Subcarrier detuning	d_2	-0.25
Quality factor	Q	1.9×10^9
Cavity Length	L_n	0.001m

Figure 6.10 shows the detunings for the $\mathscr{P}_1$ parameter space yield maximum output entanglement. While figure 3.2 shows the marginal return and limits to higher entanglement yields versus input squeezing. The marginal return is likely due to the optical cavities parameters causing the entangling effects to compete with the detangling effects. (seen in the $E_N = 0$ portions of the plots in figures 6.2, 6.3, and 6.4).

The flexibility of the two-photon formalism allows for the full simulation of homodyne measurements of the sideband quadratures. Such flexibility creates a robust platform for understanding how the output entanglement and quantum noise are affected by laboratory complications and loss parameters.

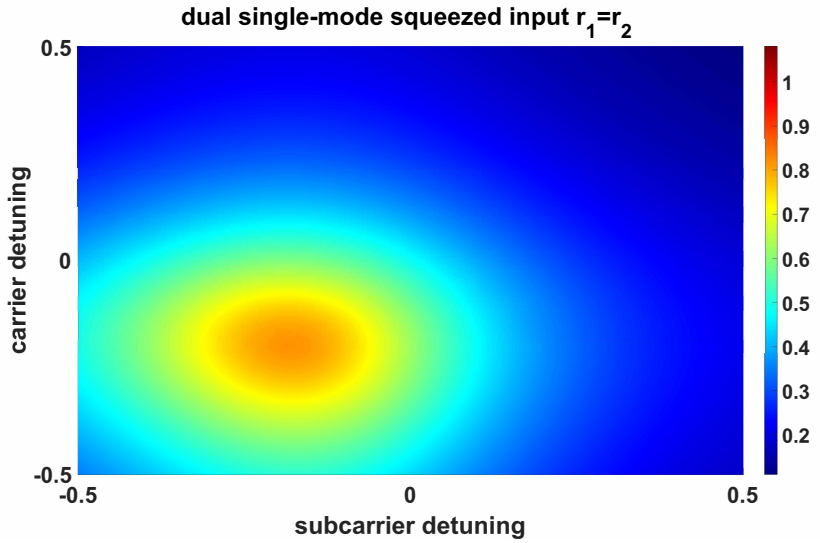

Figure 6.10: In these simulation results, the optimal detunings appear well within the regions of optical spring stability (see reference [64]). For the other calculations in this parameter space, the detunings are set to yield optimal entanglement. Furthermore, our calculations also show that the referenced work was operating at the optimal detuning to yield OM entanglement [9].

6.5 Project conclusions

Entanglement and squeezing are valuable quantum resources in quantum technologies such as quantum sensing, computing, and networking. The optomechanical cavity's properties make it an attractive prospect for studying new means of producing squeezed light and entangled light. However, generating entanglement via squeezed light injection into OMCs will likely not be a competitive method for producing entanglement from single-mode squeezed Gaussian states. At an input squeezing strength of $r = 1$ the output entanglement from the simulated OMC, entanglement circuit yielded $E_N \approx 0.8$ at squeeze angles of about π in each input arm. This is the case for both the ultra-stable parameter space and the laboratory parameter space. If one applied these squeezed coherent fields to a beam splitter, the output entanglement would yield $E_N > 3$. Although these devices yield competitive entangling rates for low input squeezing, the yields are barely higher than the unsqueezed results.

Chapter 7
Further Extensions of Squeezed Light Injection into OMC's

In the case of two single-mode squeezed coherent input states input into on optomechanical cavity, the output entanglement varied with the input squeezing angle (see figure 6.2). Naively, one could assume that the boost in input quantum noise could be modulated in some way to resonate with the harmonic nature of the OMC. To investigate this hypothesis, we replace the input squeezing angle with a function of squeezing frequency and time.

7.1 Rotating Squeeze angle

The position of the cavity endmirror $\hat{\mathbf{X}}_\mu$ has a fundamental uncertainty (Heisenberg's uncertainty), amplified by the uncertainty in the amplitude of the injected coherent field. This OM interaction drives the quantum processes in the cavity. Injecting light with more quantum noise amplifies the quantum effects of the OMC (see chapter 6). However, figure 6.2 shows that it is not strictly amplitude or strictly phase squeezed light that generates peak output entanglement. Since we already have a well-established computational model of this system, we can explore these phenomena by merely creating a virtual experiment. What would occur if the injected light's squeezing angle rotated at a frequency comparable to the mechanical oscillator frequency? Perhaps there exists some frequency in squeeze angle where the uncertainty fluctuations could induce a position uncertainty frequency that could then resonate with at least one of the intracavity field fluctuation frequencies.

When, $\theta - > \beta t + \delta_0$, and we Fourier transform to the sideband frequency Ω; the squeezing quadrature matrix becomes the following:

$$s(r,\beta,\delta_0) = \begin{pmatrix} \sqrt{\frac{\pi}{2}}\delta(\Omega-2\beta)e^{-2i\delta_0}\sinh(r)+\cosh(r) & i\sqrt{\frac{\pi}{2}}\delta(\Omega-2\beta)e^{-2i\delta_0}\sinh(r) \\ i\sqrt{\frac{\pi}{2}}\delta(\Omega-2\beta)e^{-2i\delta_0}\sinh(r) & \cosh(r)-\sqrt{\frac{\pi}{2}}\delta(\Omega-2\beta)e^{-2i\delta_0}\sinh(r) \end{pmatrix}. \quad (7.1)$$

The hypothesis fails due to the squeezing matrix's independence relative to the squeezing angle frequency from this form alone. From, Heisenberg's equation ($\dot{\hat{\mathbf{A}}} = \frac{i}{\hbar}[\mathbf{H},\hat{\mathbf{A}}] + (\frac{\partial\hat{\mathbf{A}}}{\partial t})_H$)

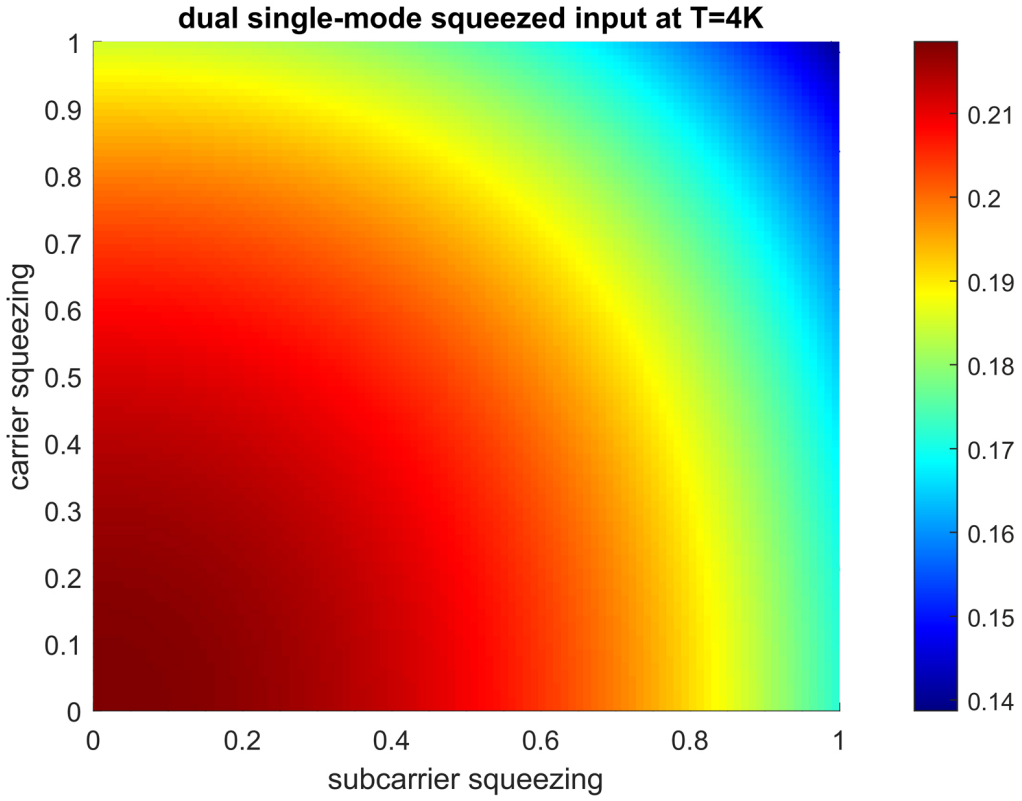

Figure 7.1: The plot is the results from the rotating squeezing angle simulation. When varying r from 0 to 1 for the two single-mode squeezed states and oscillator temperature $T = 4K$, simulation results show output entanglement only falls from such complications in the squeezing. Additionally, the transformation to a time-varying squeezing angle has eliminated the OM entanglement's angle dependence. This angle-dependency is not replaced with squeeze angle frequency dependence except near $\Omega = \pm 2\beta$. Moreover, at the harmonic frequency ($\Omega = \pm 2\beta$) the entanglement is zero. Similar to the higher order mode frequency behaivor.

we can predict the effect of the new time dependent squeezing operation:

$$[\mathbf{H}_{int}, \hat{\mathbf{S}}_j(\xi)] = (g\hat{\mathbf{f}}(\xi, 2)\hat{\mathbf{S}}_j(2\xi) - i\beta(\xi^*\hat{\mathbf{a}}^2 + \xi\hat{\mathbf{a}}^{\dagger 2}))\sum_k (-1)^k \frac{(\hat{\mathbf{X}}_\mu - 1)^k}{k!}, \tag{7.2}$$

7.2 Dual two-mode squeezed input

Previously, we addressed the applicability of optomechanical cavities as entanglement generators. However, we have yet to mention the entanglement swapping capabilities. The three-wave mixing in the OM interaction Hamiltonian makes OMCs a legitimate candidate

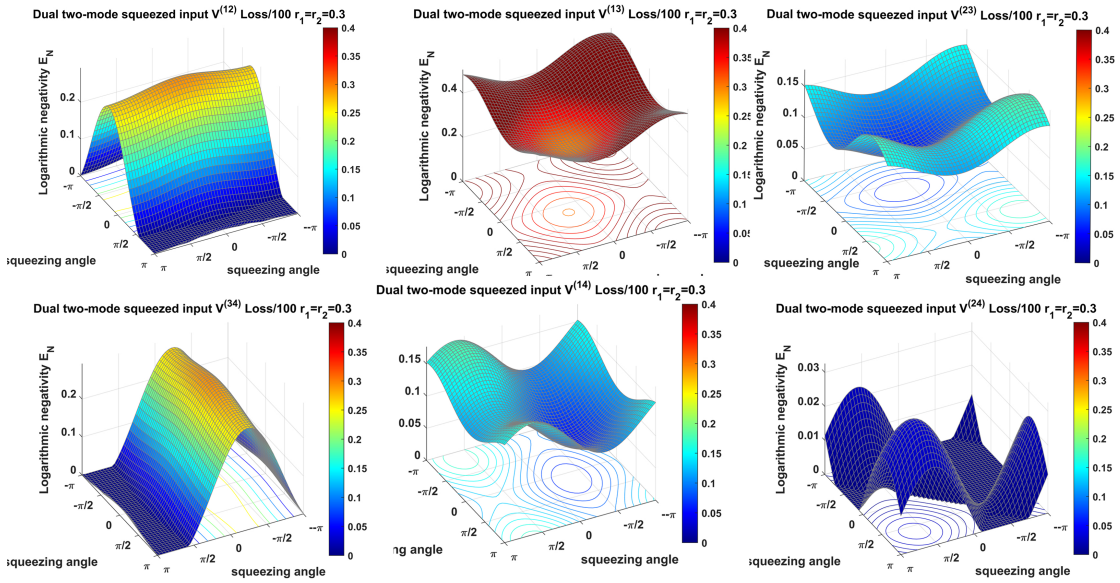

Figure 7.2: This simulation was done at $T = 4K$. The two input fields were both *two−mode squeezed*. The modes 1 and 2 were entangled intially, as is were modes 3 and 4. These results are somewhat preliminary and may require further investigation.

for further attention as a prospect for developing viable entanglement swap devices, particularly for continuous-variable applications. Figure 7.2 contains the simulation results for the pair of two-mode squeezed coherent states introduced into an OMC. The result is squeezing angle dependent entanglement swapping. In this simulation, there are four independent intracavity optical modes. Consequentially, our program for this scenario requires the diagonalization of a 126 by 126 matrix. The increase in dimension dramatically increases the programs' overall complexity since the original entanglement applications only required the diagonalization of 66 by 66 matrices per parameter configuration. Initially, modes 1 and 2 are entangled, and modes 3 and 4 are entangled. The output results show that this initial entanglement somewhat persists. However, the OMC still appears to swap some of the entangled modes, yielding more robust entanglement between modes 2 and 3

output than any other bipartite combination.

These results seem to suggest that OMC's could be utilized as continuous variable entanglement swapping devices.

7.3 Future work: networks of optomechanical cavities

Deployment of OMCs in some quantum networks will require firm comprehension of the behavior of networks of OCMs with an arbitrary number of optical input fields. Furthermore, optomechanical cavities may have further applications when integrated into devices as a series or in parallel. In this section, we take the first small steps to studying such systems in theory. Here we assume all OMC's are cantilever movable endmirror type OMCs.

somewhere cite [65, 66, 67].

7.3.1 Parallel

To investigate these applications we start from a more general Hamiltonian:

$$\mathbb{H} = \mathbf{H}_0 \ + \ \mathbf{H}_d \ + \ \mathbf{H}_{int} \ . \tag{7.3}$$

In the above equation $\mathbf{H}_0$ is the sum of the Hamiltonians of the free photons and the mechanical oscillators in the network of OMC's, and $\mathbf{H}_d$ is the sum of the driving Hamiltonians; likewise for $\mathbf{H}_{int}$ which is the sum of the interaction Hamiltonians. Perhaps the most important of the three is the interaction term:

$$\mathbf{H}_{int} = \sum_{j}^{M} \sum_{k}^{N} g_{jk} \hat{\mathbf{n}}_j \ u(\hat{\mathbf{x}}_k) \ , \tag{7.4}$$

for M photon fields and N phonon fields (mechanical oscillators). For circuits with multiple OM oscillators it may be necessary to consider higher order effects so instead of just the linear term in $\hat{\mathbf{x}}$ we include the entire series expansion which we write as $u(\hat{\mathbf{x}})$.

Since the entanglement effect on unsqueezed input states is relatively weak we shall only examine squeezed input cases. Next, we calculate the commutator of $\hat{\mathbf{S}}$ with the

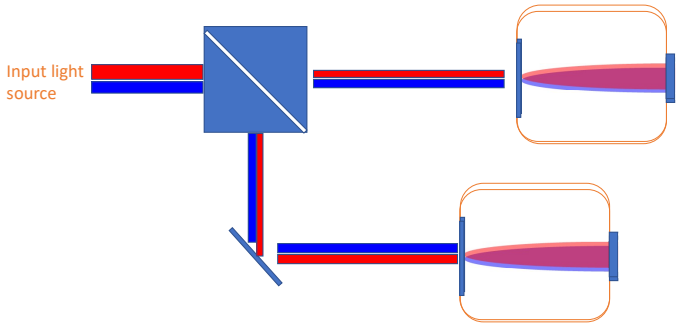

Figure 7.3: Cartoon of two OMCs configured in parallel.

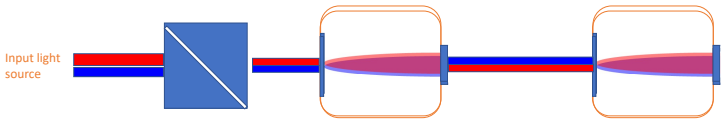

Figure 7.4: Cartoon of two OMCs configured in series.

interaction Hamiltonian:

$$[\hat{\mathbf{S}}_j, \mathbf{H}_{int}] = \sum_{j\ k\ l} [\hat{\mathbf{S}}_j, g_{kl}\hat{\mathbf{n}}_k\ u(\hat{\mathbf{x}}_l)]. \tag{7.5}$$

Ignoring the sum for now:

$$[\hat{\mathbf{S}}_j, g_{kl}\hat{\mathbf{n}}_k\ u(\hat{\mathbf{x}}_l)] = g_{kl}[\hat{\mathbf{S}}_j, \hat{\mathbf{n}}_k]\ u(\hat{\mathbf{x}}_l) = g_{kl}[\hat{\mathbf{S}}_j, \hat{\mathbf{n}}_k]\ u(\hat{\mathbf{x}}_l)\delta_{jk} \tag{7.6}$$

$$= \hat{\mathbf{S}}_j(\hat{\mathbf{n}}_k - \hat{\sigma}_k^\dagger\hat{\mathbf{a}}_k + \hat{\sigma}_k\hat{\mathbf{a}}_k - \hat{\sigma}_k^\dagger\hat{\sigma}_k)g_{kl}u(\hat{\mathbf{x}}_l)\delta_{jk}. \tag{7.7}$$

Thus when considering the full sum we can write

7.3.2 Series

$$[\hat{\mathbf{S}}_j(\xi_j), \mathbf{H}_{int}] = \sum_{j\ k} g_{jk}u(\hat{\mathbf{x}}_k)\ 2\hat{\mathbf{f}}_2(\xi_j)\hat{\mathbf{S}}_j(2\xi_j). \tag{7.8}$$

From the OM squeezing results in previous work, as well as the results displayed in figure 6.1 one could infer great applications for OMC squeezing and entanglement devices when arranged in series.

Appendix A
Miscellaneous Calculations

A.1 Calculation 1

In this section we note the steps to calculate the expected value of $\hat{\mathbf{S}}^{\dagger}(\xi)\hat{\mathbf{S}}(\zeta)$. Before we begin we note that $\hat{\mathbf{S}}^{\dagger}(\xi)\hat{\mathbf{S}}(\zeta) = \hat{\mathbf{1}}$ when $\xi = \zeta$ and $\hat{\mathbf{S}}^{\dagger}(\zeta)\hat{\mathbf{S}}(\xi) = \hat{\mathbf{S}}(\zeta)$ when $\xi = 2\zeta$ (will be shown in the following notes). Let's begin with the following:

$$\hat{\mathbf{S}}^{\dagger}(\xi)\hat{\mathbf{S}}(\zeta) = e^{-\xi^{*}\hat{\mathbf{a}}^{2}+\xi\hat{\mathbf{a}}^{\dagger 2}}\ e^{\zeta^{*}\hat{\mathbf{a}}^{2}-\zeta\hat{\mathbf{a}}^{\dagger 2}} \tag{A.1}$$

Using the Baker-Campbell-Hausdroff (BCH) formula we can write this product as follows (note: $\mathbf{A} = -\xi^{*}\hat{\mathbf{a}}^{2} + \xi\hat{\mathbf{a}}^{\dagger 2}$ and $\mathbf{B} = \zeta^{*}\hat{\mathbf{a}}^{2} - \zeta\hat{\mathbf{a}}^{\dagger 2}$):

$$\hat{\mathbf{S}}^{\dagger}(\xi)\hat{\mathbf{S}}(\zeta) = e^{-\xi^{*}\hat{\mathbf{a}}^{2}+\xi\hat{\mathbf{a}}^{\dagger 2}}\ e^{\zeta^{*}\hat{\mathbf{a}}^{2}-\zeta\hat{\mathbf{a}}^{\dagger 2}} = \exp\Big[(-\xi^{*}+\zeta^{*})\hat{\mathbf{a}}^{2} + (\xi-\zeta)\hat{\mathbf{a}}^{\dagger 2} + \hat{\mathbf{Z}}\Big], \tag{A.2}$$

where $\hat{\mathbf{Z}} = \frac{1}{2}\hat{\mathbf{k}}_0 + \frac{1}{12}([\hat{\mathbf{f}}_2(-\xi), \hat{\mathbf{k}}_0] - \frac{1}{12}[\hat{\mathbf{f}}_2(\zeta), \hat{\mathbf{k}}_0]) + ...$; and where $\hat{\mathbf{k}}_0 = \frac{1}{2}[-\xi^{*}\hat{\mathbf{a}}^{2} + \xi\hat{\mathbf{a}}^{\dagger 2}, \zeta^{*}\hat{\mathbf{a}}^{2} - \zeta\hat{\mathbf{a}}^{\dagger 2}]$.

$$\hat{\mathbf{k}}_0 = [\xi\hat{\mathbf{a}}^{\dagger 2} - \xi^{*}\hat{\mathbf{a}}^{2}, \zeta^{*}\hat{\mathbf{a}}^{2} - \zeta\hat{\mathbf{a}}^{\dagger 2}] \tag{A.3}$$

$$= [\xi\hat{\mathbf{a}}^{\dagger 2}, \zeta^{*}\hat{\mathbf{a}}^{2}] \ - \ [\xi\hat{\mathbf{a}}^{\dagger 2}, \zeta\hat{\mathbf{a}}^{\dagger 2}] \ - \ [\xi^{*}\hat{\mathbf{a}}^{2}, \zeta^{*}\hat{\mathbf{a}}^{2}] \ + \ [\xi^{*}\hat{\mathbf{a}}^{2}, \zeta\hat{\mathbf{a}}^{\dagger 2}] \tag{A.4}$$

$$= [\xi\hat{\mathbf{a}}^{\dagger 2}, \zeta^{*}\hat{\mathbf{a}}^{2}] \ + \ [\xi^{*}\hat{\mathbf{a}}^{2}, \zeta\hat{\mathbf{a}}^{\dagger 2}] \ ; \tag{A.5}$$

since, $[\hat{\mathbf{a}}^{\dagger 2}, \hat{\mathbf{a}}^{2}] = -2(2\hat{\mathbf{n}} + 1)$ and $[\hat{\mathbf{a}}^{2}, \hat{\mathbf{a}}^{\dagger 2}] = 2(2\hat{\mathbf{n}} + 1)$ we can write eqn A.5 as

$$2(\xi\zeta^{*} - \xi^{*}\zeta)(2\hat{\mathbf{n}} + 1) \ . \tag{A.6}$$

Thus, the resulting operator is highly dependent on the input squeezing angle difference and is not very sensitive to differences in squeezing strength between the two inputs. To make this more clear we can write $\hat{\mathbf{k}}_0$ in a different form than above if we assume $\xi = r_1 e^{i\theta}$ and $\zeta = r_2 e^{i\phi}$:

$$\hat{\mathbf{k}}_0 \ = \ 4ir_1 r_2 \sin(\theta - \phi)(2\hat{\mathbf{n}} + 1) \ . \tag{A.7}$$

If the squeezing angles are the same, the term $\hat{\mathbf{k}}_0$ vanishes; the real parts of the squeezing parameters do not change the form of the operator unless they are zero. Furthermore, at higher orders there are terms with dependence on $\sin(\theta + \phi)$ and $\cos(\theta + \phi)$; there is still some non-trivial complications to the squeezing operator *around* the line $\theta = \phi$. These complications may account for the peaks in the dual single-mode squeezed input entanglement results which appear to show that the entanglement is maximum when $\theta \approx \phi$; it is likely that when θ exactly equals ϕ that the E_N falls (or rises) sharply.

A.1.1 Super ξ (when $\zeta = 2\xi$)

In this case $\hat{\mathbf{k}}_0 = 0$ and so are the rest of the terms in the BCH series above. Thus, in equation A.2 $\hat{\mathbf{Z}} = 0$ and,

$$\hat{\mathbf{S}}^\dagger(\xi)\hat{\mathbf{S}}(2\xi) \;=\; \hat{\mathbf{S}}(2\xi)\ . \tag{A.8}$$

A.1.2 more on the BCH application

Additionally, this is a special application of the BCH formula that lends to a pertinent lemma. For an arbitrary matrix Lie group, L, it has a corresponding Lie algebra, ℓ. For a matrix operator element $\hat{\mathbf{X}}$ of the algebra ℓ the adjoint endomorphisim is the map for all matrix operations $\hat{\mathbf{Y}} \in \ell$ then $\mathrm{ad}_{\hat{\mathbf{X}}} : \ell \longrightarrow \ell$ with $\mathrm{ad}_{\hat{\mathbf{X}}}(\hat{\mathbf{Y}}) = [\hat{\mathbf{X}}, \hat{\mathbf{Y}}]$. Furthermore, when

$$e^{\mathrm{ad}_{\hat{\mathbf{x}}}}\hat{\mathbf{Y}} = \hat{\mathbf{Y}} + [\hat{\mathbf{X}}, \hat{\mathbf{Y}}] + \frac{1}{2!}[\hat{\mathbf{X}}, [\hat{\mathbf{X}}, \hat{\mathbf{Y}}]] + \frac{1}{3!}[\hat{\mathbf{X}}, [\hat{\mathbf{X}}, [\hat{\mathbf{X}}, \hat{\mathbf{Y}}]]]\ . \tag{A.9}$$

Then,

$$e^{\hat{\mathbf{X}}}e^{\hat{\mathbf{Y}}} = (\mathrm{ad}_{\hat{\mathbf{X}}}\hat{\mathbf{Y}})\ e^{\hat{\mathbf{X}}}\ , \tag{A.10}$$

which is known as the braiding identity [68].

A.2 Some Commutator Algebra

$$[\hat{\mathbf{S}}, \hat{\mathbf{a}}^2] = \hat{\mathbf{a}}[\hat{\mathbf{S}}, \hat{\mathbf{a}}] + [\hat{\mathbf{S}}, \hat{\mathbf{a}}]\hat{\mathbf{a}} \tag{A.11}$$

Moreover,

$$\hat{\mathbf{a}}[\hat{\mathbf{S}}, \hat{\mathbf{a}}] = \hat{\mathbf{a}}\hat{\mathbf{S}}\hat{\mathbf{a}} - \hat{\mathbf{a}}^2\hat{\mathbf{S}} \tag{A.12}$$

$$\hat{\mathbf{S}}^\dagger\hat{\mathbf{a}}[\hat{\mathbf{S}}, \hat{\mathbf{a}}] = \hat{\mathbf{S}}^\dagger\hat{\mathbf{a}}\hat{\mathbf{S}}\hat{\mathbf{a}} - \hat{\mathbf{S}}^\dagger\hat{\mathbf{a}}^2\hat{\mathbf{S}} \tag{A.13}$$

Let, $\hat{\sigma} = \hat{\mathbf{S}}^\dagger\hat{\mathbf{a}}\hat{\mathbf{S}}$, then:

$$\hat{\mathbf{S}}^\dagger\hat{\mathbf{a}}[\hat{\mathbf{S}}, \hat{\mathbf{a}}] = \hat{\mathbf{S}}^\dagger\hat{\mathbf{a}}\hat{\mathbf{S}}\hat{\mathbf{a}} - \hat{\mathbf{S}}^\dagger\hat{\mathbf{a}}^2\hat{\mathbf{S}} = \hat{\sigma}\hat{\mathbf{a}} - \hat{\sigma}^2 \Rightarrow \hat{\mathbf{a}}[\hat{\mathbf{S}}, \hat{\mathbf{a}}] = \hat{\mathbf{S}}(\hat{\sigma}\hat{\mathbf{a}} - \hat{\sigma}^2) \tag{A.14}$$

where $\hat{\sigma} = \hat{\mathbf{a}}\cosh r - \hat{\mathbf{a}}^\dagger e^{i\theta}\sinh r$.

Next,

$$[\hat{\mathbf{S}}, \hat{\mathbf{a}}]\hat{\mathbf{a}} = \hat{\mathbf{S}}\hat{\mathbf{a}}^2 - \hat{\mathbf{a}}\hat{\mathbf{S}}\hat{\mathbf{a}} \tag{A.15}$$

$$\hat{\mathbf{S}}^\dagger[\hat{\mathbf{S}}, \hat{\mathbf{a}}]\hat{\mathbf{a}} = \hat{\mathbf{a}}^2 - \hat{\mathbf{S}}^\dagger\hat{\mathbf{a}}\hat{\mathbf{S}}\hat{\mathbf{a}} = \hat{\mathbf{a}}^2 - \hat{\sigma}\hat{\mathbf{a}} \Rightarrow [\hat{\mathbf{S}}, \hat{\mathbf{a}}]\hat{\mathbf{a}} = \hat{\mathbf{S}}(\hat{\mathbf{a}}^2 - \hat{\sigma}\hat{\mathbf{a}}) \tag{A.16}$$

A.2.1 [S,n]

$$[\hat{\mathbf{S}}, \hat{\mathbf{n}}] = \hat{\mathbf{a}}^\dagger[\hat{\mathbf{S}}, \hat{\mathbf{a}}] + [\hat{\mathbf{S}}, \hat{\mathbf{a}}^\dagger]\hat{\mathbf{a}} \tag{A.17}$$

Splitting up the two terms: $[\hat{\mathbf{S}}, \hat{\mathbf{a}}^\dagger]\hat{\mathbf{a}} = \hat{\mathbf{S}}\hat{\mathbf{a}}^\dagger\hat{\mathbf{a}} - \hat{\mathbf{a}}^\dagger\hat{\mathbf{S}}\hat{\mathbf{a}} = \hat{\mathbf{S}}\hat{\mathbf{S}}^\dagger[\hat{\mathbf{S}}, \hat{\mathbf{a}}^\dagger]\hat{\mathbf{a}} = \hat{\mathbf{S}}\hat{\mathbf{n}} - \hat{\mathbf{S}}\hat{\sigma}^\dagger\hat{\mathbf{a}}$. Also,

$$\hat{\mathbf{a}}^\dagger[\hat{\mathbf{S}}, \hat{\mathbf{a}}] = \hat{\mathbf{a}}^\dagger\hat{\mathbf{S}}\hat{\mathbf{a}} - \hat{\mathbf{a}}^\dagger\hat{\mathbf{a}}\hat{\mathbf{S}} = \hat{\mathbf{S}}\hat{\mathbf{S}}^\dagger\hat{\mathbf{a}}^\dagger\hat{\mathbf{S}}\hat{\mathbf{a}} - \hat{\mathbf{S}}\hat{\mathbf{S}}^\dagger\hat{\mathbf{a}}^\dagger\hat{\mathbf{S}}\hat{\mathbf{S}}^\dagger\hat{\mathbf{a}}\hat{\mathbf{S}} = \hat{\mathbf{S}}\hat{\sigma}^\dagger\hat{\mathbf{a}} - \hat{\mathbf{S}}\hat{\sigma}^\dagger\hat{\sigma}. \tag{A.18}$$

Ultimately,

$$[\hat{\mathbf{S}}, \hat{\mathbf{n}}] = \hat{\mathbf{S}}(\hat{\mathbf{n}} - \hat{\sigma}^\dagger\hat{\mathbf{a}} + \hat{\sigma}\hat{\mathbf{a}} - \hat{\sigma}^\dagger\hat{\sigma}). \tag{A.19}$$

However, using BCH we can show that this commutator is also equivalent to $\hat{\mathbf{S}}(2\xi) - \hat{\mathbf{1}}$ (see section A.3).

more algebra

The input state is the following (neglecting the phonon/μmirror state for now):

$$|\psi_{input}\rangle = |\alpha_1, \alpha_2\rangle = \hat{\mathbf{D}}_1(\alpha_1)\hat{\mathbf{D}}_2(\alpha_2)\,|0, 0\rangle \tag{A.20}$$

The time evolution of the displacement operator (with $g- > -g$ for now).

$$[H_{int}, \hat{\mathbf{D}}_j] = \tag{A.21}$$

$$g\hat{\mathbf{X}}_\mu(\hat{\mathbf{f}}_j(\alpha) - |\alpha|^2)\ \hat{\mathbf{D}}_j \tag{A.22}$$

where $\hat{\mathbf{f}}_1(\alpha_1) = (\alpha_1^*\hat{\mathbf{a}}_1 - \alpha_1\hat{\mathbf{a}^\dagger}_1)$, $\hat{\mathbf{f}}_j^\dagger = -\hat{\mathbf{f}}_j$; Also recall that $[H, D_1D_2] = D_1[H, D_2] + [H, D_1]D_2$ Thus, $\dot{\hat{\mathbf{D}}}\,|\psi_{input}\rangle$ can be written as follows:

$$\begin{aligned}&[g\hat{\mathbf{X}}_\mu]((\hat{\mathbf{f}}_1(\alpha_1) + |\alpha_1|^2)\,|\alpha_1\rangle\,|\alpha_2\rangle \\ &\quad +(\hat{\mathbf{f}}_2(\alpha_2) + |\alpha_2|^2)\,|\alpha_1\rangle\,|\alpha_2\rangle)\ ;\end{aligned}$$

ultimately,

$$= [g\hat{\mathbf{X}}_\mu](|\alpha_1|^2 + |\alpha_2|^2)\,|\alpha_1\rangle\,|\alpha_2\rangle\ \ ; \tag{A.23}$$

noting that $\hat{\mathbf{f}}_1(\alpha_1)\,|\alpha_1\rangle = 0$. Furthermore we note the following (ignoring explicit time dependence):

$$\dot{\hat{\mathbf{D}}}_1\hat{\mathbf{D}}_2 + \hat{\mathbf{D}}_1\dot{\hat{\mathbf{D}}}_2 = [g\hat{\mathbf{X}}_\mu](\hat{\mathbf{f}}_1(\alpha_1) - |\alpha_1|^2 + \hat{\mathbf{f}}_2(\alpha_2) - |\alpha_2|^2)\hat{\mathbf{D}}_1\hat{\mathbf{D}}_2 \tag{A.24}$$

A.3 Boosting squeezing

The boost in predicted out squeezing is due to the commutator of S and Hint. Here we show this:

$$[\hat{\mathbf{S}}, \hat{\mathbf{n}}] = \hat{\mathbf{S}}\hat{\mathbf{n}}\ -\ \hat{\mathbf{n}}\hat{\mathbf{S}}; \tag{A.25}$$

since, $\hat{\mathbf{S}} = \exp\big[1/2(\xi^*\hat{\mathbf{a}}^2 - \xi\hat{\mathbf{a}}^{\dagger 2})\big] = e^{\hat{\mathbf{f}}(\xi,2)}$ and since $e^x = \sum_n \frac{x^n}{n!}$ we can write...

$$[\hat{\mathbf{S}}, \hat{\mathbf{n}}] = [\exp\big[1/2(\xi^*\hat{\mathbf{a}}^2 - \xi\hat{\mathbf{a}}^{\dagger 2})\big], \hat{\mathbf{n}}] = \sum_m [\frac{(\hat{\mathbf{f}}(\xi,2))^m}{m!}, \hat{\mathbf{n}}] = \sum_m \frac{[(\hat{\mathbf{f}}(\xi,2))^m, \hat{\mathbf{n}}]}{m!}. \quad \text{(A.26)}$$

For $m = 0$ the commutator is zero. The $m = 1$ term is

$$[(\hat{\mathbf{f}}(\xi,2)), \hat{\mathbf{n}}] = 1/2(\xi^*[\hat{\mathbf{a}}^2, n] - \xi[\hat{\mathbf{a}}^{\dagger 2}, n]) \;=\; 1/2(2\xi^*\hat{\mathbf{a}}^2 - 2\xi\hat{\mathbf{a}}^{\dagger 2}) = \hat{\mathbf{f}}(2\xi,2). \quad \text{(A.27)}$$

Next, for $m = 2$...

$$[(\hat{\mathbf{f}}(\xi,2))^2, \hat{\mathbf{n}}] = (\hat{\mathbf{f}}(\xi,2))[(\hat{\mathbf{f}}(\xi,2)), \hat{\mathbf{n}}] + [(\hat{\mathbf{f}}(\xi,2)), \hat{\mathbf{n}}](\hat{\mathbf{f}}(\xi,2)) \quad \text{(A.28)}$$

$$= \; 2(\hat{\mathbf{f}}(\xi,2))(\hat{\mathbf{f}}(2\xi,2)), \quad \text{(A.29)}$$

since $[\hat{\mathbf{f}}(\xi,2), \hat{\mathbf{f}}(2\xi,2)] = 0$. From this result we can infer that $m = 3$ is

$$2^2(\hat{\mathbf{f}}(\xi,2))^2(\hat{\mathbf{f}}(2\xi,2)) \; ; \quad \text{(A.30)}$$

thus for arbitrary k, where $k = m + 1$ we have the following:

$$[(\hat{\mathbf{f}}(\xi,2))^k, \hat{\mathbf{n}}] = 2^k(\hat{\mathbf{f}}(\xi,2))^k(\hat{\mathbf{f}}(2\xi,2)), \quad \text{(A.31)}$$

for $k = 0$ to infinity. Now we have...

$$[\hat{\mathbf{S}}, \hat{\mathbf{n}}] = [\exp\big[1/2(\xi^*\hat{\mathbf{a}}^2 - \xi\hat{\mathbf{a}}^{\dagger 2})\big], \hat{\mathbf{n}}] = 0 + \sum_k \frac{2^k(\hat{\mathbf{f}}(\xi,2))^k(\hat{\mathbf{f}}(2\xi,2))}{(k+1)!} \quad \text{(A.32)}$$

$$= \; 2^{-1}\hat{\mathbf{f}}(\xi,2)^{-1}\sum_k \frac{2^{k+1}(\hat{\mathbf{f}}(\xi,2))^{k+1}(\hat{\mathbf{f}}(2\xi,2))}{(k+1)!} \quad \text{(A.33)}$$

$$= \; \frac{1}{2}\hat{\mathbf{f}}(\xi,2)^{-1}(\hat{\mathbf{f}}(2\xi,2))(e^{\hat{\mathbf{f}}(2\xi,2)} - \hat{\mathbf{1}}) \quad \text{(A.34)}$$

But remember that $2\hat{\mathbf{f}}(\xi,2) = \hat{\mathbf{f}}(2\xi,2)$; this allows ...

$$\frac{1}{2}\hat{\mathbf{f}}(\xi,2)^{-1}(\hat{\mathbf{f}}(2\xi,2))(e^{\hat{\mathbf{f}}(2\xi,2)} - \hat{\mathbf{1}}) = (e^{\hat{\mathbf{f}}(2\xi,2)} - \hat{\mathbf{1}}) = (\hat{\mathbf{S}}(2\xi) - \hat{\mathbf{1}}) \; ; \quad \text{(A.35)}$$

thus, $[\hat{\mathbf{S}}(\xi), \hat{\mathbf{n}}] \;=\; \hat{\mathbf{S}}(2\xi) - \hat{\mathbf{1}}$.

So for two single-mode squeezed vacuum states the time derivative of the product of squeezing operators (with respect to the interaction Hamiltonian only) $(\hat{\mathbf{S}}_1(\xi)\hat{\mathbf{S}}_2(\zeta))$ is

$$(\hat{\mathbf{S}}_1(2\xi) - \hat{\mathbf{1}})\hat{\mathbf{S}}_2(\zeta) + \hat{\mathbf{S}}_1(\xi)(\hat{\mathbf{S}}_2(2\zeta) - \hat{\mathbf{1}}) \quad \text{(A.36)}$$

$$= \hat{\mathbf{S}}_1(2\xi)\hat{\mathbf{S}}_2(\zeta) + \hat{\mathbf{S}}_1(\xi)\hat{\mathbf{S}}_2(2\zeta) - \hat{\mathbf{S}}_1(\xi) - \hat{\mathbf{S}}_2(\zeta)$$

A.4 Miscellaneous

To begin let's define a useful function that takes a complex number as input and outputs an operator (we will consider the function acting on some complex input as an operator itself):

$$\hat{\mathbf{f}}_m(u) = u\hat{\mathbf{a}}^{\dagger^m} - u^*\hat{\mathbf{a}}^m \ , \tag{A.37}$$

where $m \in \mathbb{N}$. We note here that $\hat{\mathbf{f}}_m(u)^\dagger = -\hat{\mathbf{f}}_m(u)$ and that ...

$$\langle \hat{\mathbf{f}}_1(u)^\dagger \hat{\mathbf{f}}_1(u) \rangle_{00} = |u|^2 \langle (\hat{\mathbf{n}} + \hat{\mathbf{a}}\hat{\mathbf{a}}^\dagger) \rangle_{00} \tag{A.38}$$

$$= |u|^2 \langle (2\hat{\mathbf{n}} + 1) \rangle_{00} \tag{A.39}$$

$$= |u|^2 \ ; \tag{A.40}$$

moreover,

$$\langle \hat{\mathbf{f}}_2(u)^\dagger \hat{\mathbf{f}}_2(u) \rangle_{00} \tag{A.41}$$

$$= |u|^2 \langle (: \hat{\mathbf{n}} :^2 + 1 + \hat{\mathbf{a}} + 2\hat{\mathbf{n}} + \hat{\mathbf{n}}^2) \rangle_{00} \tag{A.42}$$

$$= |u|^2 \langle (: \hat{\mathbf{n}} :^2 + 1 + 2\hat{\mathbf{n}} + \hat{\mathbf{n}}^2) \rangle_{00} = |u|^2 \tag{A.43}$$

Furthermore,

$$\langle \hat{\mathbf{f}}_1(u)^\dagger \hat{\mathbf{f}}_1(u) \rangle_{\alpha_1\alpha_1} = \tag{A.44}$$

$$|u|^2 \langle (\hat{-\mathbf{n}} - \hat{\mathbf{a}}\hat{\mathbf{a}}^\dagger + \frac{u}{u^*} a^{\dagger 2} + \frac{u^*}{u} a^2) \rangle_{\alpha_1\alpha_1} \tag{A.45}$$

$$= -|u|^2 \langle (2\hat{\mathbf{n}} + 1 - \frac{u}{u^*} a^{\dagger 2} - \frac{u^*}{u} a^2) \rangle_{\alpha_1\alpha_1} \tag{A.46}$$

$$= -|u|^2 \ (2|\alpha_1|^2 + 1) \ ; \tag{A.47}$$

moreover,

$$\langle \hat{\mathbf{f}}_2(u)^\dagger \hat{\mathbf{f}}_2(u) \rangle_{\alpha_1\alpha_1} \tag{A.48}$$

$$= |u|^2 \langle (: \hat{\mathbf{n}} :^2 + 1 + \hat{\mathbf{a}} + 2\hat{\mathbf{n}} + \hat{\mathbf{n}}^2) \rangle_{\alpha_1\alpha_1} \tag{A.49}$$

$$= |u|^2 (2|\alpha|^4 + 2|\alpha|^2 + \alpha + 1) \tag{A.50}$$

A.5 Super-ξ Wigner function

Using the wave function from equation 2.22 we let equation 2.22 equal $\phi(x, w)$, and we assume that w_1 and w_2 are both greater than unity, then the Wigner function is

$$W_\Xi(x, y, w_1, w_2) = \int_{-\infty}^{\infty} \eta(x + x', w_1, w_2)^* \eta(x - x', w_1, w_2) \ e^{\frac{2i}{\hbar} y x'} dx' \ , \tag{A.51}$$

where

$$\eta(x, w_1, w_2) = \phi(x, 2w_1)\phi(x, w_2) \ + \ \phi(x, w_1)\phi(x, 2w_2) \ . \tag{A.52}$$

The result is (calculated with Mathematica):

$$W_{\Xi}(x,y,w_1,w_2) = 2\sqrt{\pi}w_1w_2\frac{\exp\left(-\frac{\frac{16w_1^2\left(w_2^4(y-4)^2+(x-1)^2\right)}{w_2^2}+\frac{w_2^2(x-1)^2}{w_1^2}+8(x-1)^2}{4\left(4w_1^2+w_2^2\right)}\right)}{\sqrt{4w_1^2+w_2^2}} + 2\sqrt{\pi}w_1w_2\frac{\exp\left(-\frac{\frac{w_1^2\left(16w_2^4(y-4)^2+(x-1)^2\right)}{w_2^2}+\frac{16w_2^2(x-1)^2}{w_1^2}+8(x-1)^2}{4\left(w_1^2+4w_2^2\right)}\right)}{\sqrt{w_1^2+4w_2^2}} + \frac{4}{5}\sqrt{\pi}w_1w_2\frac{\sqrt{10}\exp\left(-\frac{\left(4w_1^2\left(w_2^2(y-4)-i(x-1)\right)-iw_2^2(x-1)\right)\left(w_1^2\left(4w_2^2(y-4)+i(x-1)\right)+4iw_2^2(x-1)\right)}{10w_1^2w_2^2\left(w_1^2+w_2^2\right)}\right)}{\sqrt{w_1^2+w_2^2}} \quad \text{(A.53)}$$

(when w_j is less than one the factor in the wavefunction is $\frac{1}{2}$ instead of 2). This is a positive function for x and y for the case $\xi_A = \xi_B$ like in eqn 6.6.

A.6 Squeeze entanglement noise in the single homodyne detection scheme

Assume the state:

$$|\mathscr{S}\rangle = c_1 |S_X\rangle_1 |S_X\rangle_2 + c_2 |S_X\rangle_1 |S_Y\rangle_2 + c_3 |S_Y\rangle_1 |S_X\rangle_2 \ , \quad \text{(A.54)}$$

where the states $|S_X\rangle$ and $|S_Y\rangle$ represent squeezed states (squeezed in the X or Y directions) and c_{1-3} are arbitrary constants. The single homodyne detection scheme is used to measure the squeezing of a single mode. This measurement attempt fails for a state such as $|\mathscr{S}\rangle$. This is an attempt to measure the amount of squeezing in the eigenstate$|S_X\rangle$ which is s_x (times 3 for $c_1 = c_2 = c_3$), or some proportional result due to the constants. To measure squeezing in the X direction with a single homodyne scheme is mathematically equivalent to $\langle \hat{S}_X \rangle_{\mathscr{S}}$, or

$$\langle \hat{S}_X \rangle_{\mathscr{S}} = |c_1|^2 s_X + |c_2|^2 s_X \gamma - |c_3|^2 s_X + \dots \ . \quad \text{(A.55)}$$

The negative terms come from the action of the X squeezing operation on a Y squeezed state. Moreover, notice that they are terms that add and subtract, thus unnecessarily obscuring the amount of squeezing. Furthermore, the sum continues with terms that are not related to reaching the goal of the measurement. The correlations and superposition of modes both work here to obscure the desired result. Such components could be removed from the measurement in post-measurement calculations, but only when dual homodyne detection is implemented.

Appendix B
Simulation Code

B.1 Entanglement measures

B.1.1 Logarithmic negativity

This takes a covariance matrix as input.

```
    function EN = LogNeg1(tV) %takes 4x4 (co)Variance matrix as input
dtV= det(tV);
dtV11= det(tV(1:2,1:2));
dtV22= det(tV(3:4,3:4));
dtV12= det(tV(1:2,3:4));
tSigma= dtV11+dtV22-2*dtV12;
EN= max([0, real(-1/2*log(2*(tSigma-sqrt(tSigma^2-4*dtV))))]);
```

B.1.2 Duan's measure

- **code**

```
function [R]= rhsduan(fvar,Pvar,Ppvar,Lossvar,Tevar,Q0var,dLvar,dLpvar,qqq)
% yields the right hand side of the Duan inequality for a set of parameters
% R must be less than one for there to be entanglement
p0= p_gen();
A= p0; % this is just the same as codeopt really

% Setting variables
A.f= fvar;
A.P=Pvar;
A.Pp= Ppvar;
A.Loss= Lossvar;
A.Te = Tevar;
A.Q0 = Q0var;
A.dL = dLvar;
A.dLp = dLpvar;

A.readout_angle = 0;

A.rot1=0;
%c = (zeros(2,length(f)));
B = micro_code_two(A);


clear('B');
f = fvar;
```

```
for j=1:length(f)
    A.f= f(j);
    B(j,:,:)= micro_code_two(A);
    psf12(:,j)= [B(j).psdx1x2;B(j).psdy1y2];
    last4(:,j) = [B(j).psdx1y1; B(j).psdx2y1'; B(j).psdx2y2 ; B(j).psdx2y1];
end


for j=1:length(f)
    out= (cat(1,B(j).psdx1x1,B(j).psdy1y1,B(j).psdx2x2,B(j).psdy2y2));
    three= last4(1:3,j);
    four= last4(4,j);
    tVun= diag(out)+diag(psf12(:,j),-2)+diag(psf12(:,j)',2)+ ...
    diag(three,1) + diag(three',-1);
    tVun(3,2)= four; tVun(1,4)= B(j).psdx1y2'; tVun(4,1)= B(j).psdx1y2;
    tV= real(tVun/2); %real(vpa(tVun+tVun',qqq)/4);%(tVun+tVun')/2;
end

%%
G1= vpa(tV(1:2,1:2));
G2= vpa(tV(3:4,3:4));
C= vpa(tV(1:2,3:4));

dG1= det(G1); dG2 = det(G2); dC = det(C); dM = det(tV);
%%

n= sqrt(dG1); m= sqrt(dG2);
c = (1).*2.^(-1/2).*(m.^(-1).*n.^(-1).*(dC.^2+(-1).*dM+m.^2.*n.^2+( ...
    1).*((-4).*dC.^2.*m.^2.*n.^2+(dC.^2+(-1).*dM+m.^2.*n.^2).^2).^(1/2))).^(1/2);
cp = (1).*2.^(1/2).*dC.*(m.^(-1).*n.^(-1).*(dC.^2+(-1).*dM+m.^2.*n.^2+ ...
    (1).*((-4).*dC.^2.*m.^2.*n.^2+(dC.^2+(-1).*dM+m.^2.*n.^2).^2).^( ...
    1/2))).^(-1/2);% From Sol2 +-+- in Mathematica notebook
syms r1 r2 %n1 n2 m1 m2 c1 c2
%assume(abs(c1)-abs(c2)==sqrt((m1-1)*(n1-1))*sqrt((m2-1)*(n2-1)))
eqns1=[];% [ dC ==c*cp,dM==(n*m-c^2)*(n*m-cp^2)];
eqns2= [(n/r1-1)/(n*r1-1)==...
(m/r2-1)/(m*r2-1),sqrt(r1*r2)*abs(c)-abs(cp)/(sqrt(r1*r2))==...
sqrt((n*r1-1)*(m*r2-1))-sqrt((n/r1-1)*(m/r2-1))];
eqns3= [];%n1== n*r1, n2 == n/r1, m1== m*r2, m2== m/r2,c1 == ...
sqrt(r1*r2),c2== cp/(sqrt(r1*r2))];

EQNZ = cat(2,eqns1,eqns2,eqns3);

S = solve(EQNZ,[r1 r2 ],'Real',true);%n1 n2 m1 m2 c1 c2])
```

```
S.r1;
S.r2;
rr1= S.r1; rr2 = S.r2;


if ~isempty(rr1)
    nn1= vpa(n*rr1,qqq);
    nn2 = vpa(n/rr1,qqq);
    mm1= vpa(m*rr2,qqq);
    mm2= vpa(m/rr2,qqq);
    cc1 = vpa(c*sqrt(rr1*rr2),qqq);
    cc2= vpa( cp/(sqrt(rr1*rr2)),qqq);
    %%


    a= sqrt(sqrt((mm1-1)/(nn1-1)));

    %%
    %"a0 is..."
    %a
    %"Standard form disagreement "
    %double(abs(cc1)-abs(cc2)-(sqrt((mm1-1)*(nn1-1))-sqrt((mm2-1)*(nn2-1))))
    in= a^2*(nn1+nn2)/2+(mm1+mm2)/(2*a^2)-(abs(cc1)+abs(cc2));
    %"should be less than one for entangled systems"
    R=-in/(a^2+a^(-2))+1;

end
%"should be less than one for entangled systems"
```

B.2 squeezed light injection

Injecting squeezed light involves the the inclusion of the correlation matrix and then adding that as a layer in the simulated apparatus that is later diagonalized.

in the dual single-mode implementation

```
function results = micro_code_3(opt,psr,psphi,psrp,psphip)
% 2 Single mode squeezed inputs

warning('off');

%% Adding squeezed light as input
% psr= opt.psr; % squeezing strength
% psphi= opt.psphi;  % squeezing angle
```

```
% psrp= opt.psrp; % squeezing strength 2nd field
% psphip= opt.psphip;  % squeezing angle 2nd field

PreSqueeze= vpa([cosh(psr)+sinh(psr)*cos(2*psphi), sinh(psr)*sin(2*psphi);...
sinh(psr)*sin(2*psphi), cosh(psr)-sinh(psr)*cos(2*psphi)],128);
PreSqueezep= vpa([cosh(psrp)+sinh(psrp)*cos(2*psphip), sinh(psrp)*sin(2*psphip);...
sinh(psrp)*sin(2*psphip), cosh(psrp)-sinh(psrp)*cos(2*psphip)],128);
% See eqns 31  in 2phtn rev
```

...

Eventually you insert the squeezers in the apparatus like so

```
    M(a1:a2,aa1:aa2)= (PreSqueeze);%/sqrt(2);
M(a1p:a2p,aa1p:aa2p)= (PreSqueezep);%/sqrt(2);
```

where the quadrature mode labels have been properly shifted to account for new fields/optics.

single two-mode implementation

```
    function results = micro_code_4_2paper(opt,psr,psphi)

warning('off');
paulix=[0 1; 1 0];
%pauliy=1i.*[0 -1;1 0];
pauliz=[1 0;0 -1];
%% Adding squeezed light as input
une4= ones(1,4);
tempmat1= rot90(cos(psphi).*pauliz+sin(psphi).*paulix,3);
mat1= cosh(psr).*diag(une4)+sinh(psr).*rot90(blkdiag(tempmat1,tempmat1));
PreSqueeze= mat1;
PS= (PreSqueeze);
```

Which is then is included in the simulation apparatus like the previous scenario.

B.3 multi-homodyne

This is the more modular multi-homodyne detection code that appears at the end of the MATLAB code for the microcode.m programs. The general purpose was to reduce the length of the code required to better implement additional fields in the simulation.

in the four optical modes implementation

```
    %% Condensed Measurement (4 fields version)
quadindex= [t1  t2  m1p  m2p  t10  t20  m1p0  m2p0];
modeindex= [aa1, aa2, b1, b2, c1, c2, h1,h2, n1, n2 ;
   aa1p, aa2p, b1p, b2p, c1p, c2p, h1p, h2p, n1p, n2p;
    aa10, aa20, b10, b20, c10, c20, h10,h20, n10, n20 ;
   aa1p0, aa2p0, b1p0, b2p0, c1p0, c2p0, h1p0, h2p0, n1p0, n2p0];
```

```
%results.x1x1=CovMes0(quadindex, modeindex, iM,TS,1,1);
tempMat0= zeros(8);
for j=1:8
    for k=1:8
        tempMat0(j,k)= CovMes0(X,quadindex,modeindex, iM,TS,Loss, j,k);
    end
end
results.vv= tempMat0;
```

Appendix C
Miscellaneous Plots and Results

These graphics begin on the following page.

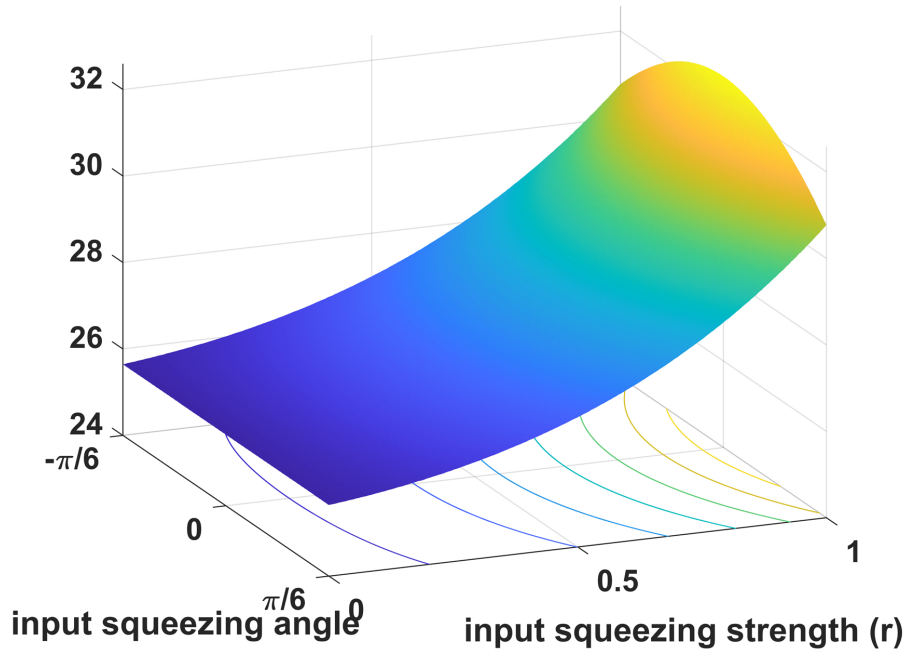

Figure C.1: Quantum to thermal noise ratio plot at $T = 4K$ for the dual single-mode squeezed displaced states input. Here $r_1 = r_2$ and $\phi_1 = \phi_2$ (for squeezing angle ϕ).

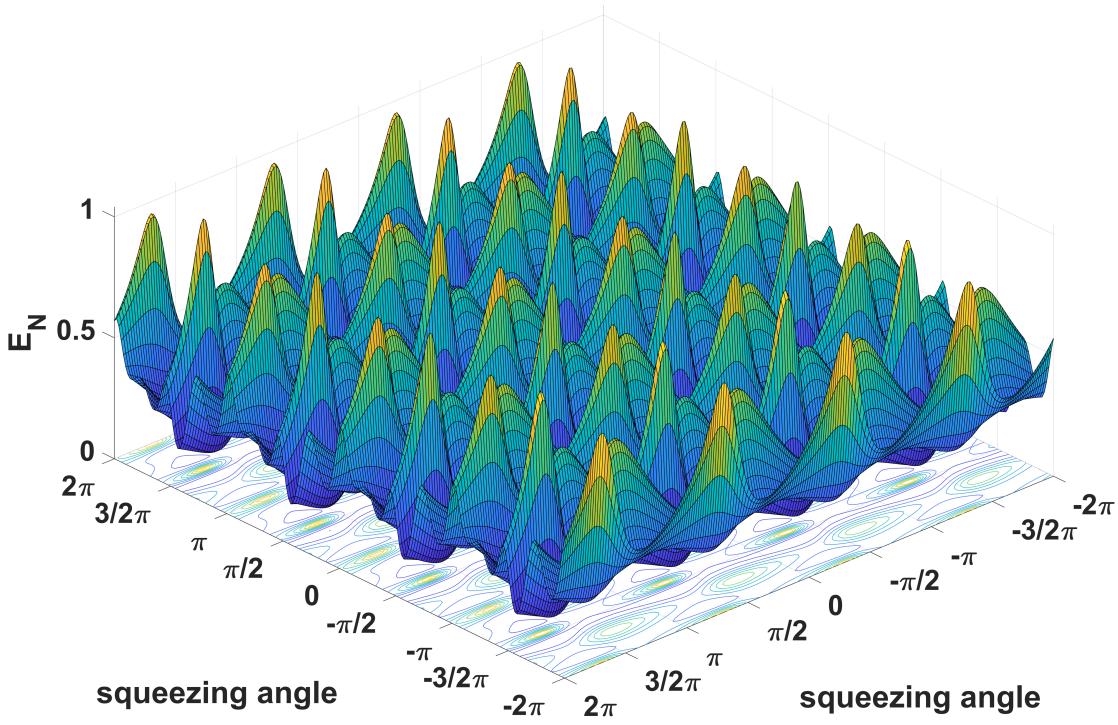

Figure C.2: Plot of the logarithmic negativity output from a μmirror OMC with two single-mode squeezed displaced states input with $r = 0.8$. Here temperature is set to 4K.

Appendix D
Reuse Permission

American Physical Society
Reuse and Permissions License

02-Apr-2021

This license agreement between the American Physical Society ("APS") and Kahlil Dixon ("You") consists of your license details and the terms and conditions provided by the American Physical Society and SciPris.

Licensed Content Information

License Number:	**RNP/21/APR/038376**
License date:	02-Apr-2021
DOI:	10.1103/PhysRevA.102.063518
Title:	Optomechanical entanglement at room temperature: A simulation study with realistic conditions
Author:	Kahlil Y. Dixon et al.
Publication:	Physical Review A
Publisher:	American Physical Society
Cost:	USD $ 0.00

Request Details

Does your reuse require significant modifications: No

Specify intended distribution locations:	Worldwide
Reuse Category:	Reuse in a thesis/dissertation
Requestor Type:	Author of requested content
Items for Reuse:	Whole Article
Format for Reuse:	Electronic

Information about New Publication:

University/Publisher:	Louisiana State University
Title of dissertation/thesis:	Optomechanical Quantum Entanglement
Author(s):	Kahlil Yusef Dixon
Expected completion date:	Apr. 2021

License Requestor Information

Name:	Kahlil Dixon
Affiliation:	Individual
Email Id:	kydixonw@gmail.com
Country:	United States

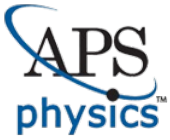

American Physical Society
Reuse and Permissions License

TERMS AND CONDITIONS

The American Physical Society (APS) is pleased to grant the Requestor of this license a non-exclusive, non-transferable permission, limited to Electronic format, provided all criteria outlined below are followed.

1. You must also obtain permission from at least one of the lead authors for each separate work, if you haven't done so already. The author's name and affiliation can be found on the first page of the published Article.
2. For electronic format permissions, Requestor agrees to provide a hyperlink from the reprinted APS material using the source material's DOI on the web page where the work appears. The hyperlink should use the standard DOI resolution URL, http://dx.doi.org/{DOI}. The hyperlink may be embedded in the copyright credit line.
3. For print format permissions, Requestor agrees to print the required copyright credit line on the first page where the material appears: "Reprinted (abstract/excerpt/figure) with permission from [(FULL REFERENCE CITATION) as follows: Author's Names, APS Journal Title, Volume Number, Page Number and Year of Publication.] Copyright (YEAR) by the American Physical Society."
4. Permission granted in this license is for a one-time use and does not include permission for any future editions, updates, databases, formats or other matters. Permission must be sought for any additional use.
5. Use of the material does not and must not imply any endorsement by APS.
6. APS does not imply, purport or intend to grant permission to reuse materials to which it does not hold copyright. It is the requestor's sole responsibility to ensure the licensed material is original to APS and does not contain the copyright of another entity, and that the copyright notice of the figure, photograph, cover or table does not indicate it was reprinted by APS with permission from another source.
7. The permission granted herein is personal to the Requestor for the use specified and is not transferable or assignable without express written permission of APS. This license may not be amended except in writing by APS.
8. You may not alter, edit or modify the material in any manner.
9. You may translate the materials only when translation rights have been granted.
10. APS is not responsible for any errors or omissions due to translation.
11. You may not use the material for promotional, sales, advertising or marketing purposes.
12. The foregoing license shall not take effect unless and until APS or its agent, Aptara, receives payment in full in accordance with Aptara Billing and Payment Terms and Conditions, which are incorporated herein by reference.
13. Should the terms of this license be violated at any time, APS or Aptara may revoke the license with no refund to you and seek relief to the fullest extent of the laws of the USA. Official written notice will be made using the contact information provided with the permission request. Failure to receive such notice will not nullify revocation of the permission.
14. APS reserves all rights not specifically granted herein.
15. This document, including the Aptara Billing and Payment Terms and Conditions, shall be the entire agreement between the parties relating to the subject matter hereof.

Bibliography

[1] P. Kurian, G. Dunston, and J. Lindesay. How quantum entanglement in dna synchronizes double-strand breakage by type ii restriction endonucleases. *Journal of Theoretical Biology*, 391:102–112, 2016.

[2] Aaron D. Jackson, Amber C. Wingfield, and Gary L. Harris. Single photon ge vacancy centers in heteroepitaxial and homoepitaxial diamond grown by hfcvd. In *Conference on Lasers and Electro-Optics*, page JTu5A.13. Optical Society of America, 2017.

[3] Khadijeh Najafi, M. M. Maśka, Kahlil Dixon, P. S. Julienne, and J. K. Freericks. Enhancing quantum order with fermions by increasing species degeneracy. *Phys. Rev. A*, 96:053621, Nov 2017.

[4] Lior Cohen, Anthony J. Brady, Zichang Huang, Hongguang Liu, Dongxue Qu, Jonathan P. Dowling, and Muxin Han. Efficient simulation of loop quantum gravity: A scalable linear-optical approach. *Phys. Rev. Lett.*, 126:020501, Jan 2021.

[5] Sanjaya Lohani, Thomas A. Searles, Brian T. Kirby, and Ryan T. Glasser. On the experimental feasibility of quantum state reconstruction via machine learning, 2020.

[6] Jonathan P Dowling. *Schrodinger's Killer App: Race to Build the World's First Quantum Computer*. CRC Press, Baton Rouge, 2013.

[7] Yan Chen, Michael Zopf, Robert Keil, Fei Ding, and Oliver G. Schmidt. Highly-efficient extraction of entangled photons from quantum dots using a broadband optical antenna. *Nature Communications*, 9(1):2994, Jul 2018.

[8] Zhaohui Ma, Jia-Yang Chen, Zhan Li, Chao Tang, Yong Meng Sua, Heng Fan, and Yu-Ping Huang. Ultrabright quantum photon sources on chip. *Phys. Rev. Lett.*, 125:263602, Dec 2020.

[9] Junxin Chen, Massimiliano Rossi, David Mason, and Albert Schliesser. Entanglement of propagating optical modes via a mechanical interface. *Nature Communications*, 11(1):943, Feb 2020.

[10] Adeline Orieux, Marijn A M Versteegh, Klaus D Jöns, and Sara Ducci. Semiconductor devices for entangled photon pair generation: a review. *Reports on Progress in Physics*, 80(7):076001, may 2017.

[11] Hui Wang, Hai Hu, T.-H. Chung, Jian Qin, Xiaoxia Yang, J.-P. Li, R.-Z. Liu, H.-S. Zhong, Y.-M. He, Xing Ding, Y.-H. Deng, Qing Dai, Y.-H. Huo, Sven Höfling, Chao-Yang Lu, and Jian-Wei Pan. On-demand semiconductor source of entangled photons which simultaneously has high fidelity, efficiency, and indistinguishability. *Phys. Rev. Lett.*, 122:113602, Mar 2019.

[12] Matthias Bock, Andreas Lenhard, Christopher Chunnilall, and Christoph Becher. Highly efficient heralded single-photon source for telecom wavelengths based on a ppln waveguide. *Opt. Express*, 24(21):23992–24001, Oct 2016.

[13] Kahlil Y. Dixon, Lior Cohen, Narayan Bhusal, Christopher Wipf, Jonathan P. Dowling, and Thomas Corbitt. Optomechanical entanglement at room temperature: A simulation study with realistic conditions. *Phys. Rev. A*, 102:063518, Dec 2020.

[14] D. Vitali, S. Gigan, A. Ferreira, H. R. Böhm, P. Tombesi, A. Guerreiro, V. Vedral, A. Zeilinger, and M. Aspelmeyer. Optomechanical entanglement between a movable mirror and a cavity field. *Phys. Rev. Lett.*, 98:030405, Jan 2007.

[15] Christopher Wipf, Thomas Corbitt, Yanbei Chen, and Nergis Mavalvala. Route to ponderomotive entanglement of light via optically trapped mirrors. *New Journal of Physics*, 10(9):095017, sep 2008.

[16] Ying-Dan Wang and Aashish A. Clerk. Reservoir-engineered entanglement in optomechanical systems. *Phys. Rev. Lett.*, 110:253601, Jun 2013.

[17] Yusef Maleki and Aleksei M. Zheltikov. A high-n00n output of harmonically driven cavity qed. *Scientific Reports*, 9(1):16780, 2019.

[18] Pieter Kok, Hwang Lee, and Jonathan P. Dowling. Creation of large-photon-number path entanglement conditioned on photodetection. *Phys. Rev. A*, 65:052104, Apr 2002.

[19] Jonathan D. Cripe. *Broadband measurement and reduction of quantum radiation pressure noise in the audio band*. PhD thesis, LSU Doctoral Dissertations, Jun 2018.

[20] Safura Sharifi, Yaser Banadaki, Torrey Cullen, Georgios Veronis, Jonathan Dowling, and Thomas Corbitt. Design of microresonators to minimize thermal noise below the standard quantum limit, 2019.

[21] Qing Lin, Bing He, and Min Xiao. Entangling two macroscopic mechanical resonators at high temperature. *Phys. Rev. Applied*, 13:034030, Mar 2020.

[22] Thomas Corbitt, Yanbei Chen, and Nergis Mavalvala. Mathematical framework for simulation of quantum fields in complex interferometers using the two-photon formalism. *Phys. Rev. A*, 72:013818, Jul 2005.

[23] Nancy Aggarwal, Torrey J. Cullen, Jonathan Cripe, Garrett D. Cole, Robert Lanza, Adam Libson, David Follman, Paula Heu, Thomas Corbitt, and Nergis Mavalvala. Room-temperature optomechanical squeezing. *Nature Physics*, 16(7):784–788, Jul 2020.

[24] Markus Aspelmeyer, Tobias J. Kippenberg, and Florian Marquardt. Cavity optomechanics. *Rev. Mod. Phys.*, 86:1391–1452, Dec 2014.

[25] E. Megidish, A. Halevy, Y. Pilnyak, A. Slapa, and H. S. Eisenberg. Quantum tomography of inductively-created large multiphoton states, 2017.

[26] Jonathan P. Dowling and Gerard J. Milburn. Quantum technology: The second quantum revolution, 2002.

[27] A. Zavatta, F. Marin, and G. Giacomelli. Quantum-state reconstruction of a squeezed laser field by self-homodyne tomography. *Phys. Rev. A*, 66:043805, Oct 2002.

[28] Clifford W. Mendel and Edl Schamiloglu. Plasma diagnostic techniques. In Robert A. Meyers, editor, *Encyclopedia of Physical Science and Technology (Third Edition)*, pages 391–400. Academic Press, New York, third edition edition, 2003.

[29] Carlton M. Caves and Bonny L. Schumaker. New formalism for two-photon quantum optics. i. quadrature phases and squeezed states. *Phys. Rev. A*, 31:3068–3092, May 1985.

[30] Olivier Pfister. Continuous-variable quantum computing in the quantum optical frequency comb. *Journal of Physics B: Atomic, Molecular and Optical Physics*, 53(1):012001, nov 2019.

[31] M. B. Plenio. Logarithmic negativity: A full entanglement monotone that is not convex. *Phys. Rev. Lett.*, 95:090503, Aug 2005.

[32] E. M. Rains. Bound on distillable entanglement. *Phys. Rev. A*, 60:179–184, Jul 1999.

[33] Stefan Bäuml, Siddhartha Das, Xin Wang, and Mark M. Wilde. Resource theory of entanglement for bipartite quantum channels, 2019.

[34] Lu-Ming Duan, G. Giedke, J. I. Cirac, and P. Zoller. Inseparability criterion for continuous variable systems. *Phys. Rev. Lett.*, 84:2722–2725, Mar 2000.

[35] Christopher Wipf. *Toward quantum opto-mechanics in a gram-scale suspended mirror interferometer*. PhD thesis, Massachusetts Institute of Technology, 2013.

[36] Thomas Randall. Corbitt. *Quantum noise and radiation pressure effects in high power optical interferometers*. PhD thesis, 2008.

[37] Sina Khorasani. Higher-order interactions in quantum optomechanics: Analysis of quadratic terms. *Scientific Reports*, 8(1):16676, Nov 2018.

[38] Jonathan Cripe, Torrey Cullen, Yanbei Chen, Paula Heu, David Follman, Garrett D. Cole, and Thomas Corbitt. Quantum backaction cancellation in the audio band. *Phys. Rev. X*, 10:031065, Sep 2020.

[39] Stefan L. Danilishin, Farid Ya. Khalili, and Haixing Miao. Advanced quantum techniques for future gravitational-wave detectors. *Living Reviews in Relativity*, 22(1):2, Apr 2019.

[40] Vittorio Giovannetti, Seth Lloyd, and Lorenzo Maccone. Advances in quantum metrology. *Nature photonics*, 5(4):222, 2011.

[41] Artur K Ekert. Quantum cryptography based on bell's theorem. *Physical review letters*, 67(6):661, 1991.

[42] Robert Raussendorf and Hans J Briegel. A one-way quantum computer. *Physical Review Letters*, 86(22):5188, 2001.

[43] Emanuel Knill, Raymond Laflamme, and Gerald J Milburn. A scheme for efficient quantum computation with linear optics. *nature*, 409(6816):46, 2001.

[44] Christopher Gerry and Peter Knight. *Introductory Quantum Optics*. Cambridge University Press, 2004.

[45] Paul G Kwiat, Klaus Mattle, Harald Weinfurter, Anton Zeilinger, Alexander V Sergienko, and Yanhua Shih. New high-intensity source of polarization-entangled photon pairs. *Physical Review Letters*, 75(24):4337, 1995.

[46] S Sofer, E Strizhevsky, A Schori, K Tamasaku, and S Shwartz. Quantum enhanced x-ray detection. *Physical Review X*, 9(3):031033, 2019.

[47] Andreas Reiserer, Norbert Kalb, Gerhard Rempe, and Stephan Ritter. A quantum gate between a flying optical photon and a single trapped atom. *Nature*, 508(7495):237, 2014.

[48] O Alibart, J Fulconis, GKL Wong, SG Murdoch, WJ Wadsworth, and JG Rarity. Photon pair generation using four-wave mixing in a microstructured fibre: theory versus experiment. *New Journal of Physics*, 8(5):67, 2006.

[49] Carlton M Caves. Quantum-mechanical radiation-pressure fluctuations in an interferometer. *Physical Review Letters*, 45(2):75, 1980.

[50] Nancy Aggarwal, Torrey Cullen, Jonathan Cripe, Garrett D Cole, Robert Lanza, Adam Libson, David Follman, Paula Heu, Thomas Corbitt, and Nergis Mavalvala. Room temperature optomechanical squeezing. *arXiv preprint arXiv:1812.09942*, 2018.

[51] Thomas Corbitt, Yanbei Chen, Edith Innerhofer, Helge Müller-Ebhardt, David Ottaway, Henning Rehbein, Daniel Sigg, Stanley Whitcomb, Christopher Wipf, and Nergis Mavalvala. An all-optical trap for a gram-scale mirror. *Phys. Rev. Lett.*, 98:150802, Apr 2007.

[52] S. Sharifi, Y. M. Banadaki, T. Cullen, G. Veronis, J. P. Dowling, and T. Corbitt. Design of microresonators to minimize thermal noise below the standard quantum limit. *Review of Scientific Instruments*, 91(5):054504, 2020.

[53] G. Vidal and R. F. Werner. Computable measure of entanglement. *Phys. Rev. A*, 65:032314, Feb 2002.

[54] K. Audenaert, M. B. Plenio, and J. Eisert. Entanglement cost under positive-partial-transpose-preserving operations. *Phys. Rev. Lett.*, 90:027901, Jan 2003.

[55] Xin Wang and Mark M. Wilde. Cost of quantum entanglement simplified. *Phys. Rev. Lett.*, 125:040502, Jul 2020.

[56] Alessio Serafini. *Quantum Continuous Variables: A Primer of Theoretical Methods*, volume 1. CRC Press, 1 edition, 2017.

[57] Wen Zhao, Sheng-Dian Zhang, Adam Miranowicz, and Hui Jing. Weak-force sensing with squeezed optomechanics. *Science China Physics, Mechanics & Astronomy*, 63(2):224211, Aug 2019.

[58] Biao Xiong, Xun Li, Shi-Lei Chao, Zhen Yang, Rui Peng, and Ling Zhou. Strong squeezing of duffing oscillator in a highly dissipative optomechanical cavity system. *Annalen der Physik*, 532(4):1900596, 2020.

[59] Hoi-Kwan Lau and Aashish A. Clerk. Ground-state cooling and high-fidelity quantum transduction via parametrically driven bad-cavity optomechanics. *Phys. Rev. Lett.*, 124:103602, Mar 2020.

[60] Chang-Woo Lee, Jae Hoon Lee, and Hyojun Seok. Squeezed-light-driven force detection with an optomechanical cavity in a mach–zehnder interferometer. *Scientific Reports*, 10(1):17496, Oct 2020.

[61] Muhammad Asjad, Najmeh Etehadi Abari, Stefano Zippilli, and David Vitali. Optomechanical cooling with intracavity squeezed light. *Opt. Express*, 27(22):32427–32444, Oct 2019.

[62] Jun John Sakurai. *Modern quantum mechanics; rev. ed.* Addison-Wesley, Reading, MA, 1994.

[63] Zhi Jiao Deng, Steven J M Habraken, and Florian Marquardt. Entanglement rate for gaussian continuous variable beams. *New Journal of Physics*, 18(6):063022, jun 2016.

[64] Thomas Corbitt, Christopher Wipf, Timothy Bodiya, David Ottaway, Daniel Sigg, Nicolas Smith, Stanley Whitcomb, and Nergis Mavalvala. Optical dilution and feedback cooling of a gram-scale oscillator to 6.9 mK. *Phys. Rev. Lett.*, 99:160801, Oct 2007.

[65] Shuntaro Takeda, Maria Fuwa, Peter van Loock, and Akira Furusawa. Entanglement swapping between discrete and continuous variables. *Phys. Rev. Lett.*, 114:100501, Mar 2015.

[66] Kevin Marshall and Christian Weedbrook. Continuous-variable entanglement swapping. *Entropy*, 17(5):3152–3159, 2015.

[67] Giovanni Guccione, Tom Darras, Hanna Le Jeannic, Varun B. Verma, Sae Woo Nam, Adrien Cavaillès, and Julien Laurat. Connecting heterogeneous quantum networks by hybrid entanglement swapping. *Science Advances*, 6(22), 2020.

[68] Brian C. Hall. *Lie groups, Lie algebras, and representations: an elementary introduction.* Graduate texts in mathematics. Springer, second edition edition, 2015.

Vita

Kahlil was born in Atlanta, Georgia and raised mostly in Nashville, Tennessee. In Nashville, Tennessee he attended and graduated from Martin Luther King Jr. Academic Magnet School from 2008 to 2012. Later that year he enrolled in Howard University in Washington, DC as an undergraduate physics major. Kahlil joined the physics department at LSU after graduating from Howard University in 2016.

Author's Publications

Khadijeh Najafi, M. M. Maska, Kahlil Dixon, P. S. Julienne, and J. K. Freericks. Enhancing quantum order with fermions by increasing species degeneracy.Phys. Rev.A, 96:053621, Nov 2017.

Kahlil Y. Dixon, Lior Cohen, Narayan Bhusal, Christopher Wipf, Jonathan P. Dowling, and Thomas Corbitt. Optomechanical entanglement at room temperature: A simulation study with realistic conditions. Phys. Rev. A, 102:063518, Dec 2020.